Scuola Internazionale Superiore di Studi Avanzati - Trieste

Angular Momentum, Assembly, and Environments of Galaxies and Halos

A thesis submitted in fulfilment of the requirements for the degree of Ph.D

in

Astrophysics

Author:
Jingjing Shi

Supervisors:
Prof. Andrea Lapi
Prof. Huiyuan Wang
Prof. Ravi K. Sheth

October 2017

SISSA - Via Bonomea 265 - 34136 TRIESTE - ITALY

To my family

Contents

Acknowledgments v

Abstract vii

Publication List ix

Acronyms xi

I Introduction 1

1 Cosmology Background 3
1.1 FRW cosmology . . . 3
1.2 Linear perturbation theory . . . 4
1.2.1 Dynamics of linear perturbations . . . 4
1.2.2 Primordial density field . . . 6
1.2.3 Zel'dovich approximation . . . 7
1.3 Non-linear evolution . . . 8
1.3.1 Spherical collapse model . . . 9
1.3.2 Numerical simulation . . . 11
1.4 Halo model . . . 12
1.4.1 Density profile . . . 13
1.4.2 Halo abundance . . . 14
1.4.3 Halo clustering . . . 15

2 Halo Assembly 19
2.1 Merger tree and halo accretion . . . 19
2.1.1 Progenitor mass function . . . 21
2.1.2 MAH & formation time . . . 22
2.1.3 Substructures . . . 25
2.2 Assembly bias . . . 25

2.2.1 Environmental indicators 26
2.2.2 Halo assembly bias 27

3 Angular Momentum of Halo and Galaxy 31
3.1 Halo angular momentum 31
3.1.1 Tidal torque theory 31
3.1.2 Spin parameter 33
3.1.3 Internal distribution 34
3.2 Angular momentum in galaxies 35
3.2.1 General properties of LTGs and ETGs 35
3.2.2 Formation of LTGs and ETGs 39
3.2.3 Angular momentum of galaxies 43

II Halo Assembly and Environment 45

4 Dependence of Halo Bias on Mass and Environment 47
4.1 Bias of constrained regions 48
4.1.1 Large scale environment as a constraint 48
4.1.2 Small scale overdensity as an additional constraint 49
4.1.3 Small scale overdensity and its derivatives as additional constraints 51
4.1.4 General formulation 51
4.1.5 Reconstructing the dependence on mass and environment . 52
4.2 Evolution 53
4.2.1 Excursion set approach: Analytic 53
4.2.2 Excursion set approach: Monte-Carlo 56
4.3 Discussion and conclusions 57

5 Environmental Dependence of Halo Dynamical Properties and Accretion History 61
5.1 Numerical simulations and dark matter halos 62
5.1.1 Simulation and halo identification 62
5.1.2 Merger trees and halos to be accreted 63
5.1.3 Large scale tidal field 66
5.2 Environmental dependence of halo accretion 67
5.2.1 Infall halo mass function 70
5.2.2 Orbits of infall halos 72
5.2.3 Alignment of accretion flow with tidal tensor 79
5.3 Environmental dependence of halo dynamical properties 81
5.4 Discussion and summary 92

6 Bimodal Age Distribution of Accreted Subhalos 95
6.1 Numerical simulations and halo merger tree 96
6.1.1 Simulation and halo merger tree 96
6.1.2 Accreted subhalo identification 97
6.2 Bimodal formation redshift distribution 97
6.2.1 Origin of the two populations 102
6.2.2 Results with EPS merger trees 106
6.3 Summary & discussion 106

III Angular Momentum of Galaxies 111

7 Angular Momentum in LTGs and ETGs 113
7.1 The initial specific angular momentum of inflowing gas 115
7.2 Fraction of inflowing gas from stellar efficiency and metal abundance 117
7.3 Star Formation efficiency and metallicity of ETGs and LTGs . . . 119
7.3.1 Star-formation efficiency of ETGs 120
7.3.2 Metal abundance of ETGs 122
7.3.3 Star formation efficiency of LTGs 123
7.3.4 Metal abundance of LTGs 123
7.4 Estimated fraction of inflowing gas and specific angular momentum 124
7.5 Discussion 130
7.5.1 The case of LTGs 131
7.5.2 The case of ETGs 131
7.6 Summary and conclusions 133

IV Summary and Outlook 135

8 Summary and Outlook 137

A 141
A.1 Relation of the work in Chapter 4 to Abbas & Sheth (2007) 141
A.2 Implications for galaxy bias 145

B 147
B.1 Additional effects on the estimate of the infalling fraction 147
B.2 Halo angular momentum profile 148
B.2.1 Simulation and halo identification 148
B.2.2 Specific angular momentum profile 148

Acknowledgments

I would like to express my sincere gratitude to my supervisors, Professor Andrea Lapi, Professor Huiyuan Wang, and Professor Ravi K. Sheth. I have always been inspired from the discussions with you during my Ph.D. Your wide range of knowledge and creative thinking helped me to nurture my interests on cosmology and galaxies. Without you all, I would not be able to finish this thesis.

I also want to thank my collaborators, Professor Luigi Danese, Professor Houjun Mo, and Dr. Lizhi Xie. It has always been a great pleasure to work and discuss with you.

Lots of thanks to my dearest fellows in SISSA, we have shared so many happy time all together, which is very valuable for me.

I wish to thank all my friends in Trieste. Your accompany means a lot to me. And special thanks to the hiking group in Trieste.

Finally, deepest gratitude goes to my lovely family, you have always been very supportive.

Abstract

This thesis is dedicated to understand more on the acquisition of angular momentum, assembly, and the effects of environments on halos and galaxies.

The simplest analyses of halo bias assume that halo mass alone determines halo clustering. However, if the large scale environment is fixed, then halo clustering is almost entirely determined by environment, and is almost completely independent of halo mass. We give an analytic explanation for this phenomenon. Our analysis is useful for studies which use the environmental dependence of clustering to constrain cosmological and galaxy formation models. It also shows why many correlations between galaxy properties and environment are merely consequences of the underlying correlations between halos and their environments, and provides a framework for quantifying such inherited correlations.

We have studied how halo intrinsic dynamical properties are linked to their formation processes for halos in two mass ranges, 10^{12} – $10^{12.5}\,h^{-1}\mathrm{M}_{\odot}$ and $\geq 10^{13}\,h^{-1}\mathrm{M}_{\odot}$, and how both are correlated with the large scale tidal field within which the halos reside at present. Halo merger trees obtained from cosmological N-body simulations are used to identify infall halos that are about to merge with their hosts. We find that the tangential component of the infall velocity increases significantly with the strength of the local tidal field, but no strong correlation is found for the radial component. These results can be used to explain how the internal velocity anisotropy and spin of halos depend on environment. The position vectors and velocities of infall halos are aligned with the principal axes of the local tidal field, and the alignment depends on the strength of the tidal field. Opposite accretion patterns are found in weak and strong tidal fields, in the sense that in a weak field the accretion flow is dominated by radial motion within the local structure, while a large tangential component is present in a strong field. These findings can be used to understand the strong alignments we find between the principal axes of the internal velocity ellipsoids of halos and the local tidal field, and their dependence on the strength of tidal field. They also explain why halo spin increases with the strength of local tidal field, but only in weak tidal fields does the spin-tidal field alignment follow the prediction of the tidal torque theory. Our results can be used to understand the spins of disk galaxies and velocity structures

of elliptical galaxies and their correlations with large-scale structure.

We have also studied the accretion histories of accreted subhalos. We found, for the very first time, a bimodal formation redshift distribution in simulations. The bimodal feature is originated from the 'universal' two phase mass accretion histories of halos. The halos that are young at accretion are those on the fast accretion phase, while old halos at accretion are already on the slow accretion phase. This bimodal feature is absent in the merger tree built with extended Press-Schechter formalism. We discuss how this bimodal feature is related with the galaxy bimodality and its implication for connecting halos with galaxies.

As comes to the galaxy formation, we have investigated the origin, shape, scatter, and cosmic evolution in the observed relationship between specific angular momentum $j_\star$ and the stellar mass $M_\star$ in early-type galaxies (ETGs) and late-type galaxies (LTGs). Specifically, we exploit the observed star-formation efficiency and chemical abundance to infer the fraction $f_{\rm inf}$ of baryons that infall toward the central regions of galaxies where star formation can occur. We find $f_{\rm inf} \approx 1$ for LTGs and ≈ 0.4 for ETGs with an uncertainty of about 0.25 dex, consistent with a biased collapse. By comparing with the locally observed $j_\star$ versus $M_\star$ relations for LTGs and ETGs, we estimate the fraction f_j of the initial specific angular momentum associated with the infalling gas that is retained in the stellar component: for LTGs we find $f_j \approx 1.11^{+0.75}_{-0.44}$, in line with the classic disc formation picture; for ETGs, we infer $f_j \approx 0.64^{+0.20}_{-0.16}$, which can be traced back to a $z \lesssim 1$ evolution via dry mergers. We also show that the observed scatter in the $j_\star$ versus $M_\star$ relation for both galaxy types is mainly contributed by the intrinsic dispersion in the spin parameters of the host dark matter halo. The biased collapse plus merger scenario implies that the specific angular momentum in the stellar components of ETG progenitors at $z \sim 2$ is already close to the local values, in good agreement with observations. All in all, we argue that such a behavior is imprinted by nature and not nurtured substantially by the environment.

Publication List

This thesis is a summary of part of my research done during my Ph.D. More specifically, it is based on the following papers:

Chapter 4: Jingjing Shi, Ravi K. Sheth "*Dependence of halo bias on mass and environment*", arXiv:1707.04096, accepted by MNRAS

Chapter 5: Jingjing Shi, Huiyuan Wang and Houjun Mo "*Flow Patterns around Dark Matter Halos: The Link between Halo Dynamical Properties and Large-scale Tidal Field*", 2015, ApJ, 807, 37

Chapter 6: Jingjing Shi, Huiyuan Wang, Houjun Mo, Lizhi Xie, Xiaoyu Wang, Andrea Lapi, Ravi K. Sheth "*The Bimodal Formation Redshift Distribution of Accreted Subhalos*", in preparation

Chapter 7: Jingjing Shi, Andrea Lapi, Claudia Mancuso, Huiyuan Wang, Luigi Danese "*Angular Momentum of Early- and Late-type Galaxies: Nature or Nurture?*", 2017, ApJ, 843, 105

Acronyms

Here, I provide a brief list of acronyms.

AGN	Active Galactic Nuclei;
ALMA	Atacama Large Millimeter Array;
BH	Black Hole;
CDM	Cold Dark Matter;
CGM	Circumgalactic Medium;
DM	Dark Matter;
EdS	Einstein-de Sitter;
EPS	Extended Press-Schechter;
ETGs	Early Type Galaxies;
FOF	Friends of Friends;
FRW	Friedmann-Robertson-Walker;
HOD	Halo Occupation Distribution;
IFS	Integral Field Spectroscopy;
IGM	Intergalactic Medium;
IMF	Initial Mass Function;
ISM	Inter-Stellar Medium;
LPT	Linear Perturbation Theory;
LSS	Large Scale Structure;
LTGs	Late Type Galaxies;
MAH	Mass Accretion History;
MW	Milky Way;
NFW	NavarroFrenkWhite ;
SAM	Semi-Analytic Model;
SF	Star Formation;
SFE	Star Formation Efficiency;
SFH	Star Formation History;
SFR	Star Formation Rate;
sSFR	specific Star Formation Rate;
SN	Supernova;
TTT	Tidal Torque Theory;

Part I:

Introduction

Chapter 1

Cosmology Background

1.1 FRW cosmology

The current standard cosmology is based on the assumption that the universe is homogeneous and isotropic on large scales. Thus the space-time structure for such universe can be described by

$$ds^2 = dt^2 - a^2(t)\left[\frac{dr^2}{1-Kr^2} + r^2(d\theta^2 + sin^2\theta d\phi^2)\right], \tag{1.1}$$

which is known as the Robertson-Walker Metric. Here light speed is set as $c = 1$, t is the proper time, $a(t)$ is the expansion factor, (r, θ, ϕ) are the spherical polar coordinate system in the comoving space, and K is the curvature parameter which takes the value of 1, 0, or -1.

In general relativity, the geometry of the space-time is determined by its matter distribution. Using the above metric, the Einstein field equations are:

$$\frac{\ddot{a}}{a} = -\frac{4\pi G}{3}(\rho + 3P) + \frac{\Lambda}{3} \tag{1.2}$$

for the time-time component and

$$\frac{\ddot{a}}{a} + 2\left(\frac{\dot{a}}{a}\right)^2 + 2\frac{K}{a^2} = 4\pi G(\rho - P) + \Lambda \tag{1.3}$$

for the space-space component. Substituting equation (1.2) into equation (1.3), we can get

$$\left(\frac{\dot{a}}{a}\right)^2 = \frac{8\pi G}{3}\rho - \frac{K}{a^2} + \frac{\Lambda}{3}\ . \tag{1.4}$$

This is the so called Friedmann equation. The cosmology that obeys it is called FRW cosmology. The left hand side of the above equation can also be written in

Hubble parameter, $H(a) \equiv \dot{a}/a$, which describes the expansion rate of the universe. And its value at present time is called the Hubble constant, denoted by H_0. By convention, H_0 is usually expressed as $H_0 = 100h\,\mathrm{kms}^{-1}\mathrm{Mpc}^{-1}$, with $h = 0.67$ (Planck Collaboration et al., 2016). Note that from now on, all variables with subscript 0 denote the values at present time unless they are clarified.

The density ρ usually includes a non-relativistic matter component, ρ_m, and a relativistic radiation component, ρ_γ. The cosmological constant can be thought as an energy component with density $\rho_\Lambda \equiv \Lambda/8\pi G$. And the thermodynamics study shows that $\rho_m \propto a^{-3}$ and $\rho_\gamma \propto a^{-4}$. Thus the above equation (1.4) can be written as

$$\left(\frac{\dot{a}}{a}\right)^2 = \frac{8\pi G}{3}\left[\rho_{m,0}\left(\frac{a_0}{a}\right)^3 + \rho_{\gamma,0}\left(\frac{a_0}{a}\right)^3 + \rho_{\Lambda,0}\right] - \frac{K}{a^2}\ . \tag{1.5}$$

If we further define the critical density as

$$\rho_\mathrm{crit}(t) \equiv \frac{3H^2(t)}{8\pi G}\ , \tag{1.6}$$

then we can get the dimensionless cosmological constant

$$\Omega_\mathrm{m}(t) \equiv \frac{\rho_\mathrm{m}(t)}{\rho_\mathrm{crit}(t)}\ , \Omega_\gamma(t) \equiv \frac{\rho_\gamma(t)}{\rho_\mathrm{crit}(t)}\ , \Omega_\Lambda(t) \equiv \frac{\rho_\Lambda(t)}{\rho_\mathrm{crit}(t)}\ . \tag{1.7}$$

Note that if we take $t = t_0$, we have $-K/(H_0^2 a_0^2) = 1 - \Omega_{\mathrm{m},0} - \Omega_{\Lambda,0} - \Omega_{\gamma,0} = 1 - \Omega_0$. There is another more commonly used time variable called redshift, $z \equiv a_0/a(t) - 1$, where $a_0 = 1$. Substituting these elements into equation (1.5), we can get

$$H^2(z) = H_0^2\left[\Omega_{\Lambda,0} + (1-\Omega_0)(1+z)^2 + \Omega_{\mathrm{m},0}(1+z)^3 + \Omega_{\gamma,0}(1+z)^4\right]\ . \tag{1.8}$$

The latest Planck collaboration suggests a flat universe (i.e. $K = 0$) and $\Omega_{\mathrm{m},0} = 0.31$, $\Omega_{\Lambda,0} = 0.69$ and $\Omega_{\gamma,0} \leq 0.0025/h^2$.

1.2 Linear perturbation theory

Standard cosmology model assumes that structures in the universe originated from small initial density perturbations imprinted by the quantum fluctuations during inflation, with their further growth dominated by the gravitational force. When the perturbation is very small ($\delta \ll 1$), linear evolution theory applies.

1.2.1 Dynamics of linear perturbations

To study the evolution of small perturbations in an expanding FRW cosmology, it is convenient to use comoving coordinate $\mathbf{x}$, defined as

$$\mathbf{r} = a(t)\mathbf{x}\ . \tag{1.9}$$

The proper motion $\mathbf{u} = \dot{\mathbf{r}}$, at point $\mathbf{x}$, can be written as

$$\mathbf{u} = \dot{a}(t)\mathbf{x} + \mathbf{v} \ , \mathbf{v} \equiv a\dot{\mathbf{x}} \ , \tag{1.10}$$

where $\mathbf{v}$ is the peculiar velocity describing the motion of the fluid relative to the fundamental observer, comoving with the background, and $\dot{a}\mathbf{x}$ is the Hubble flow. We can express the density ρ in terms of the density contrast, δ, against the backgroud, represented by $\bar{\rho}$ (note that $\bar{\rho} \propto a^{-3}$),

$$\rho(\mathbf{x}, t) = \bar{\rho}(t)\left[1 + \delta(\mathbf{x}, t)\right] . \tag{1.11}$$

Then the time evolution of a perfect fluid (which applies to the baryonic gas, pressureless dust, and collisionless dark matter) can be described by the equation of continuity (which describes the mass conservation), the Eulerian equation (the equation of motion), and the Poisson equation (describing the gravitational field):

$$\begin{gathered} \frac{\partial \delta}{\partial t} + \frac{1}{a}\nabla\left[(1+\delta)\mathbf{v}\right] = 0 \ , \\ \frac{\partial \mathbf{v}}{\partial t} + \frac{\dot{a}}{a}\mathbf{v} + \frac{1}{a}(\mathbf{v}\cdot\nabla)\mathbf{v} = -\frac{\nabla\Phi}{a} - \frac{\nabla P}{a\bar{\rho}(1+\delta)} \ , \\ \nabla^2\Phi = 4\pi G\bar{\rho}a^2\delta \ , \end{gathered} \tag{1.12}$$

where $\nabla \equiv \nabla_{\mathbf{x}}$ and $\partial/\partial t$ is in the comoving space. Given the equation of state, the above equations can be in principle solved. For a pressureless perturbation, the solutions for the above equations are:

$$\delta_- \propto H(z) \ , \tag{1.13}$$

denoting the decaying mode of $\delta(t)$ and

$$\delta_+ \propto H(z)\int_z^\infty \frac{(1+z')}{E^3(z')}dz' \ , \tag{1.14}$$

denoting the growing mode, where $E(z) = H(z)/H_0$. In the case of an Eds universe with $a(t) \propto t^{2/3}$, we have

$$\delta_- \propto t^{-1} \ , \delta_+ \propto t^{2/3} \ . \tag{1.15}$$

In the more general case, the growing mode can be gotten numerically. Carroll, Press & Turner (1992) gives a good approximation:

$$\delta_+ \propto D(z) \propto g(z)/(1+z) \ , \tag{1.16}$$

where $g(z) \approx 2.5\Omega_{\rm m}(z)\left\{\Omega_{\rm m}^{4/7}(z) - \Omega_\Lambda(z) + [1 + \Omega_{\rm m}(z)/2]\,[1 + \Omega_\Lambda(z)/70]\right\}^{-1}$ and $D(z)$ is the so called linear growth rate.

Since all fluctuations are quite small at early time, it is reasonable to assume that the growing mode dominates at more recent epochs. Under this assumption, the linear evolution of the density perturbation can be written as

$$\delta(\mathbf{x}, t) = \frac{D(t)}{D(t_i)}\delta_i(\mathbf{x}, t_i) \ , \tag{1.17}$$

where $\delta_i(\mathbf{x}, t_i)$ is the perturbation at a given time t_i.

1.2.2 Primordial density field

The primordial density field is found to be very well approximated by a homogeneous and isotropic Gaussian random field, which can be completely described by its power spectrum or its two-point correlation function.

The two point correlation function is defined as

$$\xi(x) \equiv \langle \delta_1(\mathbf{x}_1)\delta_2(\mathbf{x}_2)\rangle \ , \text{with } x \equiv |\mathbf{x}_1 - \mathbf{x}_2|. \tag{1.18}$$

Note that $\xi(0) = \sigma^2$ is the variance of the field and $\xi(x)$ depends only on the distance x. The density perturbation field $\delta(\mathbf{x})$ can also be written by its Fourier transform:

$$\delta_{\mathbf{k}} = \frac{1}{V}\int \delta(\mathbf{x})\exp(-i\mathbf{k}\cdot\mathbf{x})d^3\mathbf{x} \ , \tag{1.19}$$

where $V = L^3$ is the volume of the box on which the perturbation field is assumed to be periodic and $\mathbf{k} = (2\pi/L)(i_x, i_y, i_z)$, with (i_x, i_y, i_z) to be integers. The power spectrum is defined as $P(k) \equiv V\langle|\delta^2_{\mathbf{k}}|\rangle$. Inputting equation (1.19) into the above formula, we have

$$P(k) = \int \xi(\mathbf{x})e^{-i\mathbf{k}\cdot\mathbf{x}}d^3\mathbf{x} = 4\pi\int_0^\infty \xi(r)\frac{\sin kr}{kr}r^2dr \ . \tag{1.20}$$

Inversely, we also have

$$\xi(r) = \frac{1}{(2\pi)^3}\int P(k)e^{i\mathbf{k}\cdot\mathbf{r}}d^3\mathbf{k} = \frac{1}{2\pi^2}\int_0^\infty P(k)\frac{\sin kr}{kr}k^2dk \ . \tag{1.21}$$

It is commonly assumed that the initial power spectrum is a power law,

$$P(k) \propto k^n \ , \tag{1.22}$$

where n is the spectral index. This is consistent with the prediction of inflation models. A special case is $n = 1$, which is called the scale invariant spectrum. During the linear evolution phase (or say in the linear regime), each Fourier mode

evolves independently. The linear power spectrum can be related to the initial power spectrum via the transfer function, $T(k)$:

$$P(k,z) = P(k,z_i)T^2(k)\frac{D^2(z)}{D^2(z_i)} \tag{1.23}$$

where $D(z)$ is the growth rate as defined in the above Section 1.2.1. The accurate solution for $T(k)$ requires solving Boltzmann equation, which is a quite complicated task. There are several well developed codes for this task, for example, CMBFAST (Seljak & Zaldarriaga, 1996), CAMB (Lewis & Bridle, 2002), and CLASS (Lesgourgues, 2011).

For a linear power spectrum with a certain shape, the amplitude is known if we know $P(k)$ for a given k or any value that is dependent on $P(k)$ statistically. The normalization of the linear $P(k)$ is known if we can measure the variance of the density field smoothed with a radius of R:

$$\sigma^2(R) = \frac{1}{2\pi^2}\int P(k)W_{\rm R}^2(k)k^2dk \ , \tag{1.24}$$

where $W_{\rm R}(k) = 3/(kR)^3[\sin(kR) - kR\cos(kR)]$ is the top-hat window function. For a historical reason, we usually denote the normalization using

$$\sigma_8 \equiv \sigma_{\rm m}(8\,h^{-1}{\rm Mpc}) \ . \tag{1.25}$$

It is important to notice that σ_8 is evaluated from the initial power spectrum evolved to the present day with the linear theory. Or to say, if the perturbation evolves linearly across the whole cosmic history for all the scales, then σ_8 is simply the variance of the present-day mass distribution smoothed with $8\,h^{-1}$Mpc. However, it is clearly true that non-linear effects can not be neglected at this scale, thus σ_8 does not necessarily correspond to the true mass variance now.

Measuring σ_8 is still one of the most important tasks for cosmological observation. Planck Collaboration et al. (2016) gives $\sigma_8 = 0.82$.

1.2.3 Zel'dovich approximation

As δ approaches 1, the above linear theory won't apply any more. Zel'dovich (1970) came up with the formalism that as long as the matter can be taken as cold dust moving under the action of gravity alone, the motion of a single particle can be described by a simple law:

$$\mathbf{x}(t) = \mathbf{q}_{\rm i} - b(t)\mathbf{s}(\mathbf{q}_i) \ , \tag{1.26}$$

where $\mathbf{q}_i$ is the initial Lagrangian comoving coordinate, and the second term represents displacement due to the density perturbation. This formula is known as

Zel'dovich Approximation. $b(t)$ and $\mathbf{s}(\mathbf{q}_i)$ can be determined as follows (Shandarin & Zeldovich, 1989), see Mo, van den Bosch & White (2010) for a derivation from linearized Euler equation.

According to the principle of mass conservation, there is

$$\rho(\mathbf{x},t)a^3(t)d^3\mathbf{x} = \rho_i(\mathbf{q}_i)d^3\mathbf{q}_i \ , \tag{1.27}$$

where $a(t)$ is the normalized scale factor, with $a(t_i)$ set to be 1. Thus

$$\rho(\mathbf{x},t) = \rho_i(\mathbf{q}_i)a^{-3}\|\frac{d\mathbf{x}}{d\mathbf{q}_i}\|^{-1} \ , \tag{1.28}$$

stands, where the tensor can be expressed as

$$\left(\frac{d\mathbf{x}}{d\mathbf{q}_i}\right)_{jk} = \delta_{jk} - b(t)\frac{\partial \mathbf{s}_j}{\partial \mathbf{q}_k} \ . \tag{1.29}$$

Substituting this into equation (1.28), we have

$$1+\delta(\mathbf{x},t) = \frac{1}{[1-b(t)\lambda_1]\,[1-b(t)\lambda_2]\,[1-b(t)\lambda_3]} \ , \tag{1.30}$$

note that $\delta(\mathbf{q}_i) \ll 1$, $\bar{\rho}(t)a^3 = \bar{\rho}_i a_i^3$, and $\lambda_1 > \lambda_2 > \lambda_3$ are the eigenvalues of the deformation tensor $\partial \mathbf{s}_j/\partial \mathbf{q}_k$. Linearization of the above equation further gives $1+\delta(\mathbf{x},t) \simeq 1 + b(t)(\lambda_1+\lambda_2+\lambda_3)$. Hence, in the linear regime, $\delta(\mathbf{x},t) = b(t)\nabla\mathbf{s}$. Combing with the Possion equation, $\delta_i = \nabla^2\Phi_i/4\pi G\bar{\rho}_i a_i^3$, and equation (1.17), $\delta(\mathbf{x},t) = D(t)\delta_i(\mathbf{q}_i)$ (with $D(t_i)$ set to be 1), we have

$$b(t) = D(t) \text{ and } \mathbf{s}(\mathbf{q}_i) = \frac{1}{4\pi G\bar{\rho}_m a^3}\nabla\Phi_i(\mathbf{q}_i) \ . \tag{1.31}$$

From equation (1.30), we can see that when $D(t)\lambda_1 \ll 1$, the perturbation is still in the linear regime. If $D(t) = 1/\lambda_i$, shell crossing happens along the direction of the i^{th} eigenvector. Further more, the equation clearly suggests that collapse happens first along the eigenvector with the largest eigenvalue, λ_1, forming flattened sheet-like structure (Zel'dovich pancakes). Zel'dovich proposed that the formulation (i.e. equations (1.26) and (1.31)) could be used to extrapolate the evolution of structure into the quasi-linear regime where the displacements are not that small (up to $\delta \sim 1$). With its good accuracy, Zel'dovich approximation is usually used to set up initial conditions for cosmological simulations.

1.3 Non-linear evolution

When $\delta > 1$, linear perturbation theory discussed in the above section is no longer valid. The density field loses its Gaussianality due to the mode coupling. And

the evolution of the density field can not be described by a simple growth rate. In order to specify the density field in the non-linear regime, several methods have been developed, including spherical collapse model and ellipsoid collapse model (Bond et al., 1991; Sheth, Mo & Tormen, 2001), high-order perturbation theory (Bernardeau et al., 2002), numerical simulations (Springel, 2005; Springel et al., 2005), and halo model (Cooray & Sheth, 2002). In this section, I am going to introduce only spherical collapse and numerical simulation briefly. And the introduction on halo model will be discussed in next Section 1.4.

1.3.1 Spherical collapse model

The spherical top-hat collapse model is a simple but useful model for describing the non-linear evolution. For an ideal case, a spherical symmetry for the top-hat density perturbation in a homogeneous and isotropic background is assumed. Only gravitational collapse of collisionless matter like DM is considered, non-gravitational effects are negligible. Here I am going to show explicitly the case with $\Omega_\Lambda = 0$, i.e. with EdS cosmology. Since at high z, all cosmologies behave similar to EdS universe, the treatment is a reasonable good approximation for the early time structure growth.

Consider a shell with mass M in the perturbation field, with its initial radius, density contrast and background density, denoted by r_i, δ_i, and $\bar{\rho}_i$. Mass conservation stands before shell crossing, thus $M(r) = 4/3\pi r_i^3 \bar{\rho}_i(1+\delta_i) = 4/3\pi r(t)^3 \bar{\rho}(t)(1+\delta(t))$. The dynamics of the shell obeys

$$\frac{1}{2}\left(\frac{dr}{dt}\right)^2 - \frac{GM}{r} = E \ , \tag{1.32}$$

where E is the energy per unit mass. When $E < 0$, the mass shell is going to collapse, and the solution for the above equation is

$$r = A(1-\cos\theta) \tag{1.33}$$

$$t = B(\theta - \sin\theta) \tag{1.34}$$

where $\theta \in [0, 2\pi]$, and $A = (GM)/(2|E|)$, $B = (GM)/(2|E|)^{3/2}$. From this solution, we can see that the shell starts expansion at $r = 0$ with $t = 0$ and $\theta = 0$. Using $dr/dt = 0$, we can find the shell reaches the maximum radius, $r_{\rm max}$, when $\theta = \pi$ and $t_{\rm ta} = \pi B$, where $t_{\rm ta}$ is called turn-around time. And the shell reaches back $r = 0$ when $\theta = 2\pi$ with $t_{\rm col} = 2t_{\rm ta}$, where the collapse time $t_{\rm col}$ is also called the virialization time.

During the collapse, energy is conserved, $E_i = E_{\rm ta} = E_{\rm col}$. And we can obtain $E_i = K_i\delta_i$. This implies that our previous requirement that $E_i < 0$ for collapse can

be translated into $\delta_i > 0$. Or to say, in EdS cosmology, all overdensities collapse. Further more, at turn-around point, the velocity of the shell is 0, we thus have

$$\frac{r_{\rm max}}{r_i} = \frac{1+\delta_i}{\delta_i} \simeq \delta_i^{-1} \ . \tag{1.35}$$

This equation implies that the turn-around radius depends only on the initial overdensity, and larger perturbations have larger $r_{\rm max}$, thus collapse later.

The actual overdensity within the spherical collapse region is $1+\delta = \rho/\bar{\rho}$, where the mean density within the region is $\rho = 3M/(4\pi r^3)$ and the background mean density is $\bar{\rho} = 1/(6\pi G t^2)$ (Dodelson, 2003). Inputting equations (1.33) and (1.34), we have

$$1+\delta = \frac{9}{2}\frac{(\theta-\sin\theta)^2}{(1-\cos\theta)^3} \ . \tag{1.36}$$

So far, the discussion for spherical collapse is done in the Eulerian frame. If we switch to Lagrangian frame, linear theory suggests that $\delta_{\rm L}(t) \propto D(t) \propto t^{2/3}$ in EdS cosmology. The initial condition of this evolution can be given using equation (1.36) in the limit $\theta \ll 1$ at the very early time. Using a Taylor series expansion of $\sin\theta$ and $\cos\theta$, we have

$$\delta_i = \frac{3}{20}(6\pi)^{2/3}\left(\frac{t_i}{t_{\rm ta}}\right)^{2/3} \ . \tag{1.37}$$

Thus linear theory prediction gives

$$\delta_{\rm L}(t) = \delta_i\left(\frac{t}{t_i}\right)^{2/3} = \frac{3}{20}(6\pi)^{2/3}\left(\frac{t}{t_{\rm ta}}\right)^{2/3} \ . \tag{1.38}$$

It is interesting to compare the overdensity value of the spherical collapse model (Eulerian space), with the one of the linear theory (Lagrangian space) at some specific time. For example, at turn-around point, equation (1.36) gives $1+\delta(t_{\rm ta}) \simeq 5.55$, while equation (1.38) gives $\delta_{\rm L}(t_{\rm ta}) \simeq 1.062$. At collapse time, $t_{\rm col}$, the Eulerian density is infinite and the Lagrangian one reads

$$\delta_c \equiv \delta_{\rm L}(t_{\rm col}) \simeq 1.686 \ . \tag{1.39}$$

This is saying that regions with their linearly extrapolated densities $\delta_{\rm L}(t) \geq 1.686$ should have collapsed. δ_c is often called critical overdensity for collapse. Note that this value is gotten under EdS cosmology. However, calculations under non-EdS (i.e. ΛCDM) cosmology found weak dependence on cosmology. $\delta_c = 1.686$ stays a rather good approximation.

According to the above spherical collapse model, δ approaches infinity at $t_{\rm col}$. In reality, this would not happen since shell crossing happens before. Shells interact

with each other, exchanging mass and energy, resulting in a virialized halo. A halo in virial equilibrium satisfies virial theorem:

$$2K + U = 0 \ , \tag{1.40}$$

where K is the final total kinematic energy and U is the gravitational binding energy. Applying energy conservation, we can have $r_{\rm vir} = r_{\rm ta}/2$, where $r_{\rm vir}$ is the radius of the virialized halo. Thus the density after virialization is 8 times larger than that at turn-around point. It is reasonable to take the virialization time same as $t_{\rm col}$, i.e. $t_{\rm vir} = t_{\rm col}$. Since $\bar{\rho} \propto t^{-2}$ in EdS cosmology and $t_{\rm col} = 2t_{\rm ta}$, the actual overdensity of a virialized dark matter halo is

$$1 + \Delta_{\rm vir} \equiv \frac{\rho(t_{\rm col})}{\rho(\bar{t_{\rm col}})} = \frac{8\rho(t_{\rm ta})}{\bar{\rho}(t_{\rm ta})/4} = 18\pi^2 \approx 178 \ . \tag{1.41}$$

The extension to ΛCDM cosmology gives (Bryan & Norman, 1998)

$$\Delta_{\rm vir} \approx \frac{18\pi^2 + 82x - 39x^2}{1+x} \ , \tag{1.42}$$

where $x \equiv \Omega(z_{\rm vir}) - 1$ with $\Omega(z_{\rm vir}) = \left[\Omega_{\rm m,0}(1+z_{\rm vir})^3\right] / \left[H^2(z_{\rm vir})/H_0^2\right]$. This quantity is used to define dark matter halos in numerical simulations or in analytic models.

1.3.2 Numerical simulation

Numerical simulations have the merit of taking full treatment for the non-linear evolution. Current numerical simulations can be divided into two main categories: N-body and hydro-dynamics. In the N-body simulation, only gravitational interaction is considered, which is dominated by the collisionless dark matter. Dark matter in the simulation is represented by particles. And their initial conditions are usually set by imposing a desired power spectrum (generated by Boltzmann code) on a glass-like uniform particle load (White, Efstathiou & Frenk, 1993). The structure formation can be traced by solving the following equations given by Newton's law:

$$\begin{aligned} \frac{d\mathbf{x}}{dt} &= \frac{1}{a}\mathbf{v} \\ \frac{d\mathbf{v}}{dt} + H\mathbf{v} &= \nabla\phi \\ \nabla^2\phi &= -4\pi G a \left[\rho(\mathbf{x},\mathbf{t}) - \bar{\rho}\right] \ , \end{aligned} \tag{1.43}$$

Note that here it is in comoving coordinates. Cosmological N-body simulations are still under development, pursuing larger box and higher resolution.

In contrast, hydro-dynamical simulation involves baryons besides dark matter. Both of them evolve self-consistently, with the baryon-DM interaction included

automatically. The baryonic process, such as star formation, radiative cooling, reionization, stellar mass loss and metal enrichment, SN and AGN feedback, and supermassive BHs are implemented by sub-grid physics (Springel et al., 2005). Current cosmological hydro-dynamical simulations like EAGLE (Schaye et al., 2015) and Illustris (Vogelsberger et al., 2014b), have been able to recover successfully various galaxy properties. However, the implement of the specific sub-grid physics still needs improvement and verification.

1.4 Halo model

Halo Model is an explicit analytic description for the non-linear gravitational clustering (i.e. the mass distribution on non-linear scale). In this approach, all masses are associated with certain virialized dark matter halos (for a comprehensive review, see Cooray & Sheth 2002). Throughout this section, we assume that a halo has spherical symmetry, with its density profile totally determined by its mass, $\rho(r|m) = mu(r|m)$. Here $u(r|m)$ is the normalized density profile, $\int d^3\mathbf{x}u(\mathbf{x}|m) = 1$. Thus the density field can be written as

$$\rho(\mathbf{x}) = \sum_i m_i u(\mathbf{x} - \mathbf{x}_i|m_i) \ , \tag{1.44}$$

which is a summation of the contribution from each halo, and i stands for the i*th* halo. The mean density is

$$\bar{\rho} =< \rho(\mathbf{x}) >= \int dmn(m)m \int d^3\mathbf{x}' u(\mathbf{x} - \mathbf{x}'|m) = \int dmn(m)m \ , \tag{1.45}$$

where the mass function $n(m)$ is the number density of halos with mass m (see Section 1.4.2).

The two point correlation function is $\xi_{\rm mm}(r) \equiv< \delta(\mathbf{x})\delta(\mathbf{x}+\mathbf{r}) >=< \rho(\mathbf{x})\rho(\mathbf{x}+\mathbf{r}) > /\bar{\rho}^2 - 1$, where

$$< \rho(\mathbf{x})\rho(\mathbf{x}+\mathbf{r}) >= \sum_i \sum_j < n_i n_j m_i m_j u(\mathbf{x}_1 - \mathbf{x}_i|m_i)u(\mathbf{x}_2 - \mathbf{x}_j|m_j) > \ , \tag{1.46}$$

with $\mathbf{x}_2 = \mathbf{x}_1 + \mathbf{r}$. This equation can be further split into 1-halo term ($i = j$) and the 2-halo term ($i \neq j$):

$$< \rho(\mathbf{x})\rho(\mathbf{x}+\mathbf{r}) >_{\rm 1h}= \int dmm^2 n(m) \int d^3\mathbf{x} u(\mathbf{x}_1 - \mathbf{x}|m)u(\mathbf{x}_2 - \mathbf{x}|m) \tag{1.47}$$

$$\begin{aligned} < \rho(\mathbf{x})\rho(\mathbf{x}+\mathbf{r}) >_{\rm 2h}=&\bar{\rho}^2 + \int dm_1 m_1 n(m_1) \int dm_2 m_2 n(m_2) \\ &\times \int d^3\mathbf{x}'_1 u(\mathbf{x}_1 - \mathbf{x}'_1|m_1) \int d^3\mathbf{x}'_2 u(\mathbf{x}_2 - \mathbf{x}'_2|m_2) \\ &\times \xi_{\rm hh}(\mathbf{x}'_1 - \mathbf{x}'_2|m_1, m_2) \end{aligned} \tag{1.48}$$

On large scales, $\xi_{\rm hh}(r|m_1, m_2) = b(m_1)b(m_2)\xi_{\rm mm}(r)$, the above 2-halo term can be simplified, where $b(m)$ is the bias factor which takes account of the fact that halo does not represent the mass field perfectly (see Section 1.4.3 for more information). Further more, we should note that on small scale the bias factor is complicated and halo exclusion effect needs to be taken good care of. We can see that the 1-halo term describes the contribution from correlation inside the halo, while the 2-halo term describes the contribution by two distinct halos. It is much more convenient to write the correlation function in Fourier space, for which we have

$$\begin{aligned} P(k) &= P_{\rm 1h}(k) + P_{\rm 2h}(k) \ , \\ P_{\rm 1h}(k) &= \int dmn(m)\left(\frac{m}{\bar{\rho}}\right)^2 |u(k|m)|^2 \ , \\ P_{\rm 2h}(k) &= \int dm_1 n(m_1)\frac{m_1}{\bar{\rho}}u(k|m_1)\int dm_2 n(m_2)\frac{m_2}{\bar{\rho}}u(k|m_2)P_{\rm hh}(k|m_1, m_2) \end{aligned} \tag{1.49}$$

where $u(k|m)$ is the Fourier transform of the density profile $u(r|m)$, and $P_{\rm hh}(k|m_1, m_2)$ represents the power spectrum of halos with mass m_1 and m_2.

By far, we can see that once the halo abundance, $n(m)$, halo bias, $b(m)$, and halo internal mass distribution, $u(k|m)$, are known, we can give a rather good description of the matter filed. Halo model has been widely used in observational cosmology to explain the galaxy clustering and weak lensing measurements (Zehavi et al., 2011; Zu & Mandelbaum, 2015). In the following, I am going to introduce briefly the three key prescriptions separately.

1.4.1 Density profile

Using N-body simulations with good resolution, Navarro, Frenk & White (1996) and Navarro, Frenk & White (1997) found that all virialized halos can be described by an universal density profile

$$\rho(r) = \rho_{\rm crit}\frac{\delta_0}{(r/r_s)(1 + r/r_s)^2} \ , \tag{1.50}$$

where δ_0 is the characteristic overdensity, r_s is the scale radius. This formula is known as the famous NFW profile. This profile is characterized by a logarithmic slope of -1 near the center and a gradual change to -3 at large radii. As $r \to 0$, $\rho(r) \to \infty$, suggesting the existence of a cusp in the center.

The enclosed mass can be given by

$$M(r) = 4\pi\bar{\rho}\delta_0 r_s^3\left[\ln(1 + cx) - \frac{cx}{1 + cx}\right] , \tag{1.51}$$

where $x \equiv r/r_{\rm h}$ and $c \equiv r_{\rm h}/r_s$ is the halo concentration parameter. Note that if we define $\rho(r_{\rm h}) = \Delta_{\rm h}\rho_{\rm crit}$, where $\Delta_{\rm h}$ is given by equation 1.42, then

$$\delta_0 = \frac{\Delta_{\rm h}}{3}\frac{c^3}{\ln(1+c) - c/(1+c)} \ . \tag{1.52}$$

Thus, for a given cosmology, a halo density profile is totally determined by its mass, M, and concentration parameter, c, or equivalently, by r_s and δ_0.

1.4.2 Halo abundance

In this section, I am going to discuss the method for obtaining halo abundance characterized by mass function $n(m)$. As we have discussed in Section 1.3.1, a halo can be related to an initial patch with overdensity $\delta_i > 0$ (in EdS universe). According to the linear theory, the density field evolves as $\delta(\mathbf{x}, t) = D(t)\delta_0(\mathbf{x})$, where $\delta_0(\mathbf{x})$ is the density field extrapolated to $t = t_0$, and $D(t)$ is the linear growth rate normalized to unity at $t = t_0$. Spherical collapse model predicts regions with $\delta(\mathbf{x}, t) > \delta_c \simeq 1.686$ to collapse into dark matter halos at time t. Or equivalently, regions with $\delta_0(\mathbf{x}) > \delta_c(t) = \delta_c/D(t)$ will have collapsed to form dark matter halos at time t.

Consider a density field smoothed with some window function, $W(\mathbf{x}; R)$, then we have

$$\delta(\mathbf{x}; R) = \int \delta(\mathbf{x}')W(\mathbf{x} - \mathbf{x}'; R)d^3\mathbf{x}' \ , \tag{1.53}$$

and the variance of the smoothed density field is (same as equation (1.24)),

$$\sigma^2(R) = \langle\delta(\mathbf{x}; R)\rangle = \frac{1}{2\pi^2}\int P(k)\hat{W}^2(kR)k^2dk \ . \tag{1.54}$$

The three commonly used window functions are top-hat, Gaussian, and sharp-k filter. For a given window function with size R, the mass within it satisfies $M \propto R^3$. Thus either M or R is the only variable that characterizes the filter. Note that in CDM based cosmology, the mass variance $\sigma^2(R)$ decreases monotonically with increasing filter size R (or M). Therefore, $\sigma^2(R)$, R, and M are equivalent. Let us define $S \equiv \sigma^2(R)$. Recall that initial density field is Gaussian:

$$P(\delta; R) = \frac{1}{(2\pi S)^{1/2}}\exp\left[-\frac{\delta^2}{2S}\right] \ . \tag{1.55}$$

In 1974, Press & Schechter proposed the idea that (at time t) the fraction of mass in halos with mass M is twice the probability that $\delta(\mathbf{x}; R) > \delta_c/D(t)$:

$$F(M, t) = 2\int_{\delta_c/D(t)}^{\infty} p\left(\delta; R\right)d\delta = \mathrm{erfc}\left(\frac{\nu}{\sqrt{2}}\right) \ , \tag{1.56}$$

where $\nu \equiv \delta_c(t)/\sqrt{S}$ is the peak height, and the time enters only through D(t). By differentiating the above equation, we have the halo mass function

$$n(M,t) = \frac{\bar{\rho}}{M^2} f_{\rm PS}(\nu) |\frac{{\rm dln}\nu}{{\rm dln}M} dM| \text{ with } f_{\rm PS}(\nu) = \sqrt{\frac{2}{\pi}} \nu e^{-\nu^2/2} \ . \tag{1.57}$$

The PS formalism suffers from the fudge factor problem, i.e., the factor 2 in equation (1.56) is put without a good physical origination. To solve this problem, Bond et al. (1991) proposed the 'excursion set theory', also called the EPS formalism. The theory started from the fact that each point $\mathbf{x}$ in the smoothed density field corresponds to a trajectory in δ_S versus S plane, starting from $(0,0)$. Especially, when sharp-k filter is adopted, each step of the trajectory is a Markovian process, that is, the step of $\Delta\delta_S$ associated with ΔS depends only on its current position and has no memory of its previous path. In order to derive the mass function, Bond et al. (1991) requires further that the fraction of trajectories with their first up-crossing of the barrier $\delta_c(t)$ at $S > S_1$ is equal to the mass fraction within halos of $M < M_1$, where S_1 and M_1 are the mass variance and mass of the larger region where the halos lie in. Consequently, we have the mass function (i.e. the comoving number density of halos divided by dM)

$$\begin{aligned} n(M,t) =& \frac{\bar{\rho}}{M} \frac{\partial F(>M)}{\partial M} = -\frac{\bar{\rho}}{M} \frac{\partial F(<M)}{\partial M} \\ =& -\frac{\bar{\rho}}{M} \frac{\partial F(>S)}{\partial S} \frac{dS}{dM} = \frac{\bar{\rho}}{M} f_{\rm FU}(S, \delta_c(t)) |\frac{dS}{dM}| \ , \end{aligned} \tag{1.58}$$

with the fraction of the trajectories that have their first up-crossing of the barrier, $\delta_c(t) = \delta_c/D(t)$, between S and $S + dS$ expressed as

$$f_{\rm FU}(S, \delta_c(t)) = \frac{1}{\sqrt{2\pi}} \frac{\delta_c(t)}{S^{3/2}} \exp\left[-\frac{\delta_c(t)^2}{2S}\right] \ , \tag{1.59}$$

where we have applied the fact that $F(>M) = 1 - F(<M)$, since each mass element is expected to collapse with mass $M > 0$. Note that equation (1.58) is exactly the same as equation (1.57).

1.4.3 Halo clustering

Dark matter halos are biased tracers of the matter field. The above EPS formalism can be used to derive halo bias. In the following, I am going to show briefly the calculation in Lagrangian space following Mo & White (1996). The calculation for the bias factor in Eulerian space can be found in Sheth (1998).

Based on the EPS argument, Bond et al. (1991) further derived the fraction of mass in a region of radius R_0 and linear overdensity δ_0 initially that ends up in a

DM halo with mass M_1 (note that $M_1 < M_0$) at z_1 is

$$f(S_1, \delta_1|S_0, \delta_0)\frac{dS_1}{dM_1}dM_1 = \frac{1}{(2\pi)^{1/2}}\frac{\delta_1 - \delta_0}{(S_1 - S_0)^{3/2}}\exp\left[-\frac{(\delta_1 - \delta_0)^2}{2(S_1 - S_0)}\right]\frac{dS_1}{dM_1}dM_1 \ . \tag{1.60}$$

Thus the constrained halo number within this region is

$$N(1|0)dM_1 \equiv \frac{M_0}{M_1}f(S_1, \delta_1|S_0, \delta_0)\frac{dS_1}{dM_1}dM_1 \ , \tag{1.61}$$

note that here M_0 is referred to the mass of the region which is uncollapsed at $z = 0$.

Lagrangian space

The overdensity of the number of halos that form from a region of radius R_0 and overdensity δ_0 initially is

$$\delta_{\rm h}^{\rm L}(1|0) = \frac{N(1|0)}{n(M_1, z_1)V_0} - 1 \ , \tag{1.62}$$

where $V_0 = 4\pi R_0^3/3$, $N(1|0)$ and $n(M_1, z_1)$ are given by equation (1.58) and (1.61). When $R_0 \gg R_1$ and $|\delta_0| \ll \delta_1$, the above equation can be simplified to

$$\delta_{\rm h}^{\rm L}(1|0) = \frac{\nu_1^2 - 1}{\delta_1}\delta_0 \ . \tag{1.63}$$

Thus, halo overdensity is proportional to the mass density field, with the proportionality given by the bias factor

$$b_{\rm h}^{\rm L} = \frac{\nu_1^2 - 1}{\delta_1} \ . \tag{1.64}$$

The above formula is the same as the one given by Cole & Kaiser (1989) based on peak-background split model. Thus, on large scales, the cross correlation between halos of mass M_1 that formed at $z = z_1$ and the mass in Lagrangian sphere of radius R_0 can be written as $\xi_{\rm hm}^L(R_0, M_1, z_1) = \langle\delta_{\rm h}^L(1|0)\delta_0\rangle_{R_0} = b_{\rm h}^{\rm L}\Delta_0$, where $\Delta_0 \equiv \langle\delta_0^2\rangle$.

Eulerian space

To model the clustering signal in the Eulerian space, the key point is that the mass within the Eulerian region of $R_{\rm E}$ is the same as the mass within the initial Lagrangian region $R_{\rm L}$. Initially, $\delta_{\rm L} \ll 1$, then $M = \bar{\rho}(1 + \delta_{\rm E})V_{\rm E} \simeq \bar{\rho}V_{\rm L}$. Thus we have

$$1 + \delta_{\rm E} = (R_{\rm L}/R_{\rm E})^3 \ . \tag{1.65}$$

The Lagrangian size $R_{\rm L}$ and density $\delta_{\rm L}$ can be related to the Eulerian size $R_{\rm E}$ and density $\delta_{\rm E}$ using spherical collapse model. Equations (1.33) and (1.34) can be re-written as

$$\frac{R_{\rm E}(R_{\rm L},\delta_{\rm L},z)}{R_{\rm L}} = \frac{3(1+z)}{5\delta_{\rm L}}\frac{1-\cos\theta}{2} \ , \tag{1.66}$$

where $\delta_{\rm L}$ is the density extrapolated linearly to current time and $1-\cos\theta$ can be replaced by $\cosh\theta - 1$ if the patch is underdense. Combing with equation (1.65), equation (1.66) describes the fact that once $R_{\rm E}$ and z are given, we can have a corresponding curve in the $(R_{\rm L}, \delta_{\rm L})$ plane. To a good approximation, it gives (Mo & White, 1996)

$$\frac{\delta_{\rm L}(R_{\rm L}|R_{\rm E},z)}{1+z} = 1.68647 - \frac{1.35}{\delta_{\rm E}^{2/3}} - \frac{1.12431}{\delta_{\rm E}^{1/2}} + \frac{0.78785}{\delta_{\rm E}^{0.58661}} \ . \tag{1.67}$$

A simpler approximation gives (Bernardeau, 1994)

$$\frac{\delta_{\rm L}(R_{\rm L}|R_{\rm E},z)}{1+z} = \delta_c - \delta_c(1+\delta_{\rm E})^{-1/\delta_c}, \tag{1.68}$$

which is also called the moving barrier, represented by $B(R_{\rm L}|R_{\rm E},z) = \delta_{\rm L}(R_{\rm L}|R_{\rm E},z)/(1+z)$. Different from the constant barrier δ_c, this barrier is changing with the mass scale defined by $R_{\rm L}$.

Under the above assumption, the overdensity of halo number within a sphere characterized by Eulerian radius R and overdensity δ can be obtained:

$$\delta_h(1|0) = \frac{N(1|0)}{n(M_1,z_1)V} - 1 \ , \tag{1.69}$$

where $V = 4\pi R^3/3$, $R_{\rm L}$ is given by equation (1.65), and $\delta_{\rm L}$ is determined from δ using equation (1.68). When $R_{\rm L}^0 \gg R_{\rm L}^1$ and $|\delta_{\rm L}^0| \ll \delta_{\rm L}^1$, we have

$$\delta_{\rm h}(1|0) = b_h(M_1,z_1)\delta = \left(1 + \frac{\nu_1^2-1}{\delta_{\rm L}^1}\right)\delta \tag{1.70}$$

Thus, the linear halo bias is

$$b_{\rm h}(M_1,z_1) = 1 + (\frac{\nu_1^2-1}{\delta_1}) = 1 + b_h^{\rm L}(M_1,z_1) \ . \tag{1.71}$$

We can see that the bias factor increases with halo mass, with the massive halos being more clustered.

Halo bias is determined by the mass, as shown by equation (1.71) and (1.64). Besides, in the EPS theorem, steps of the walks are assumed to be uncorrelated when sharp-k filter is adopted. However, for more physical filters, like the Gaussian

filter, this is not true anymore. In Musso & Sheth (2012, 2014), they developed a "Markovian Velocity Model" to describe the case with more physical filters. In this model, the walk steps are correlated and it is an extension of the EPS theory, so they are also called "correlated excursion set formalism" . In Chapter 4, we are going to use this model to explore analytically how the bias varies with halo mass and environment.

Chapter 2

Halo Assembly

In the standard CDM paradigm of structure formation, a key concept is the formation and evolution of dark matter halos. Since halos are the hosts of observed galaxies, the studies of halo properties are essential for understanding the formation and evolution of galaxies in the cosmic density field. Generally speaking, the key halo properties are: halo abundance (see Section 1.4.2), internal structure (see Section 1.4.1), dynamical properties (see Section 3.1), assembly histories(see below) and clustering properties (see Section 1.4.3). These properties are intertwined. For example, halo concentration is found to depend strongly on the mass accretion history(MAH) of a halo (Wechsler et al., 2002; Zhao et al., 2003a,b); and halo clustering correlates with the formation redshifts of halos at fixed halo mass (Gao, Springel & White, 2005). In the standard CDM scenario, structures form hierarchically. Small scale fluctuations collapse into virialized halos first and merge into larger halos. Thus halo properties are expected to be determined by their formation histories. The difference of clustering strength for halos of different ages at fixed mass indicates the importance of environments. In this chapter, I am going to introduce briefly the studies on halo assembly history and the effects of environments.

2.1 Merger tree and halo accretion

The history of the merger events can be represented by a halo merger tree, as shown in Figure 2.1. For a halo identified with certain algorithm at $t = t_0$, there exists the main trunk, which is consisted of the consecutive most massive progenitor in each snapshot. Clearly, there are more small halos at high redshift and those small halos merger into larger ones at low redshift.

Currently, there are mainly three ways to generate merger trees. The first one is numerical simulation. There are very well developed codes, such as Gadget-

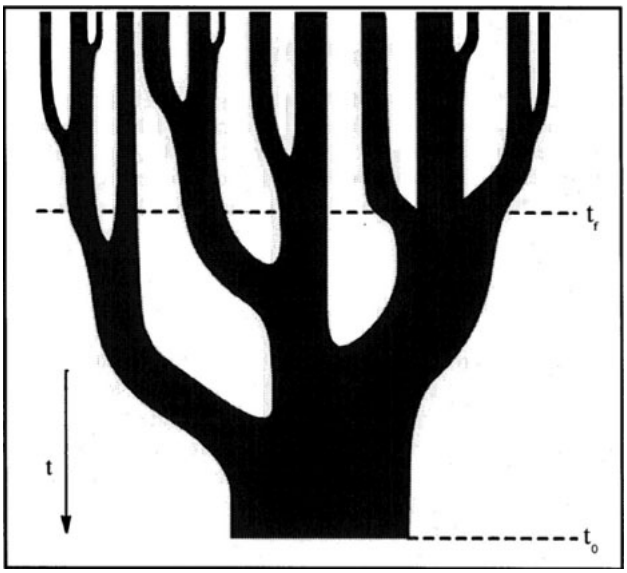

Figure 2.1: Illustration of a halo merger tree showing the progenitors of a halo selected at time t_0. The figure is taken from Lacey & Cole (1993).

2 (Springel, 2005), to trace the gravitational evolution of the inputting initial density field. Snapshots of the evolved field are recorded at certain chosen redshifts and halos are recognized within the field (Davis et al., 1985). With certain criteria, the halos in each snapshot are connected and recognized as progenitors and descendants. Although it is the most accurate and probably the most commonly used way to construct merger trees, N-body simulation suffers the limits of resolution effects, the mis-identification of halo finder and tree building algorithm, and it's computationally expensive. The second one is EPS formalism, which is discussed in more detail in Section 2.1.1. The third one is the semi-numerical methods, which uses LPT to follow the evolution of the density field. The codes based on this method, such as PINOCCHIO (Monaco et al., 2002; Monaco, Theuns & Taffoni, 2002; Monaco, 2016) and COLA (Tassev, Zaldarriaga & Eisenstein, 2013), are computationally fast and accurate at large scale structures.

The halo merger tree is a complicated structure, efforts are still needed to fully understand it. In the following, I am going to discuss several main features of the merger tree, i.e. progenitor mass function and the MAH. The remnants of the merging events are substructures, which are believed to be the hosts of satellite galaxies. Thus the study of the substructures might be important for understanding the properties of satellites. Note that not all substructures are associated with merging events and the satellite galaxy is not necessarily living in a substructure when observed.

2.1.1 Progenitor mass function

EPS formalism (see Section 1.4.2) offers a good chance to study the halo mass assembly with mergers. Equation (1.60) describes the mass fraction of a larger region (uncollapsed) that collapses into smaller halos. This equation stands even when the larger region corresponds to a collapsed larger halo which forms later than the smaller one. This is because both situations can be translated as calculating the probability that a trajectory passes δ_0 at S_0 given its first upcrossing of barrier $\delta_1 = \delta_c/D(t_1)$ at $S_1 > S_0$.

In this case, the progenitor mass function, i.e. the number of progenitors at time t_1 in the mass interval $(M_1, M_1 + dM_1)$ that merge with another halo to form a halo of mass M_0 by time t_0, is given by equation (1.61). Explicitly, it is

$$n(M_1, t_1|M_0, t_0) = \frac{M_0}{M_1} f(\nu_{01}) \left|\frac{\mathrm{dln}\nu_{01}}{\mathrm{dln}M_1}\right| , \tag{2.1}$$

where $\nu_{01} \equiv (\delta_1 - \delta_0)/\sqrt{S_1 - S_0}$, and $f(\nu) = \sqrt{2/\pi}\nu\exp(-\nu^2/2)$ (Lacey & Cole, 1993). Basically, this function tells us, for a given halo mass M at time t, how the mass distribution of its progenitors at earlier time $t - \Delta t$ is like. Thus, starting with this function, a merger tree can be built for any given halo in principle. Several algorithms have been developed, including binary tree (Lacey & Cole, 1993), N-branch method with accretion (Somerville & Kolatt, 1999) and many others (Kauffmann & White, 1993; Parkinson, Cole & Helly, 2008; Sheth & Lemson, 1999; Jiang & van den Bosch, 2014). Even each of them has their own pros and cons, and they all share the same advantages of being fast and free of the resolution limits.

Another way to characterize the mass distribution of progenitors is the un-evolved subhalo mass function. It describes the mass distribution of progenitors that build up a host halo along its lifetime. van den Bosch, Tormen & Giocoli (2005) and Giocoli, Tormen & van den Bosch (2008) found an universal un-evolved subhalo mass function using EPS merger trees and N-body simulations separately, which is independent of the present host halo mass. Especially, Giocoli, Tormen & van den Bosch (2008) provides a fitting formula,

$$\frac{dN}{d\ln(m_v/M_0)} = N_0 x^{-\alpha} e^{-6.283x^3}, \quad x = \frac{m_v}{\alpha M_0} \tag{2.2}$$

where $\alpha = 0.8$ and $N_0 = 0.21$. In contrast, Xie & Gao (2015) found that the universality of this mass function doesn't stand any more when adopting a different definition for the un-evolved subhalo population. They found the progenitors of the present day massive hosts are relatively more abundant than the low mass hosts. The difference of these studies implies that we need to choose the subhalo population with more care. And future higher resolution simulations with improved halo finder and tree building algorithm are going to clarify this issue more clearly.

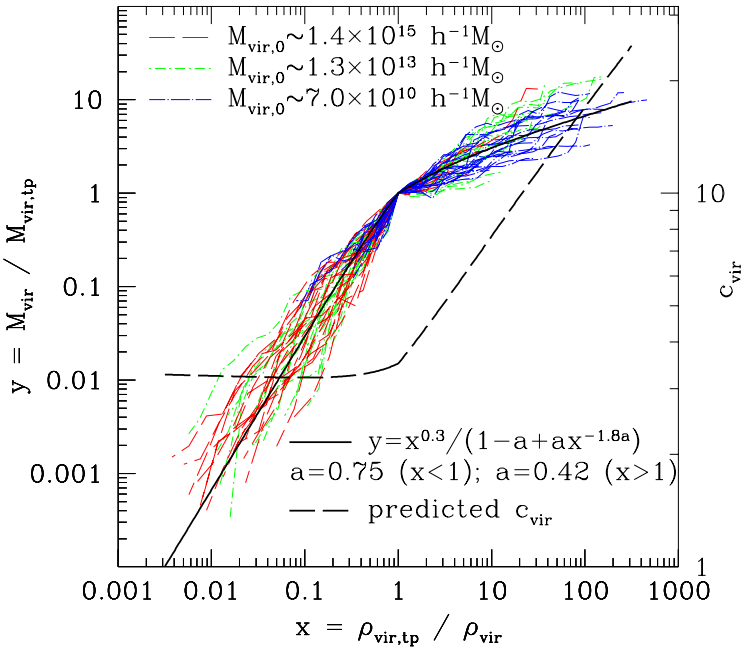

Figure 2.2: MAH of dark matter halos. The solid black line represents equation (2.3). The thick dashed line denotes the corresponding concentration c_{vir} evolution. The figure is taken from Zhao et al. (2003a).

2.1.2 MAH & formation time

Halo assembly history is fully represented by its merger tree. However, as mentioned before, it is a complex structure, which includes a lot of information. An explicit and useful way to describe the assembly history is the MAH, $M(z)$, which traces the mass growth history of the most massive progenitors. It has been studied by merger trees constructed with EPS formalism (van den Bosch, 2002; Jiang et al., 2014) and merger trees in numerical simulation (Wechsler et al., 2002; Zhao et al., 2003a,b).

Zhao et al. (2003a,b) found that the MAH of a halo is usually characterized by a fast accretion phase (with the growth rate larger than the expansion rate of the universe) and a slow accretion phase (with the growth rate approximately same as the expansion rate $\propto H(z)^{-1}$). The two phases are connected through a turning-around point. They further found an universal MAH form for halos with mass in the range of 7×10^{10} to $1.3 \times 10^{15}\, h^{-1}\mathrm{M}_{\odot}$, see Figure 2.2. The average MAH can be described by

$$\frac{M(z)}{M(z_{tp})} = \frac{x^{0.3}}{1 - a + ax^{-1.8a}} \,, \tag{2.3}$$

where z_{tp} is the turning point redshift, $x \equiv \rho(z_{tp})/\rho(z)$, and $a = 0.75(0.42)$ for the fast (slow) accretion phase. The MAH is tightly correlated with the structure of halos, as shown in Figure 2.2. At fast accretion phase, c is found to be nearly a constant ~ 3.5, and it increases quickly as the halo enters the slow accretion phase. This directly shows that the halo density profile is correlated with its mass assembly.

To be even simpler, the MAH can be characterized by some parameters. So far, only a small number of simple quantities have been adopted to characterize the formation histories of individual halos, and most of them are based on characteristic times at which a halo has assembled a fixed fraction of its final mass (e.g. Navarro, Frenk & White, 1995; Wechsler et al., 2002; Zhao et al., 2009) or the gravitational potential well associated with the halo has reached some depth (Zhao et al., 2003b). The most popular one is the formation redshift, z_f. There exist a bunch of definitions of the formation time. Li, Mo & Gao (2008) gives a comprehensive comparison among all those definitions. However, the most simple and commonly used definition is the time when the most massive progenitor of the halo, $M(z)$, reaches the mass of $M(z)/2$.

The probability distribution of z_f can be obtained easily with EPS formalism (Lacey & Cole, 1993). Starting with equation (1.60), the probability that the formation redshift, z_f, of a halo is smaller than z_1 is equal to the probability of the existence of a parent halo with $M_0/2 < M_1 < M_0$ at z_1:

$$P(t_f < t_1|M_0, t_0) = \int_{M_0/2}^{M_0} n(M_1, t_1|M_0, t_0) dM_1 = \int_{S_0}^{S_{1/2}} \frac{M_0}{M_1} f(S_1, \delta_1|S_0, \delta_0) dS_1 \ , \tag{2.4}$$

where $S_{1/2} = S(M_0/2)$. Introducing $\widetilde{\omega}(t_1) \equiv (\delta_1 - \delta_0)/\sqrt{S_{1/2} - S_0}$ and $\widetilde{S}(M_1) \equiv (S_1 - S_0)/(S_{1/2} - S_0)$, the above formula can be written as

$$P(t_f < t_1|M_0, t_0) = P(> \widetilde{\omega}(t_1)|M_0, t_0) = \frac{1}{2\pi} \int_0^1 \frac{M(S_0)}{M(S_1)} \frac{\widetilde{\omega}}{\widetilde{S}^{3/2}} \exp\left[-\frac{\widetilde{\omega}^2}{2\widetilde{S}}\right] \mathrm{d}\widetilde{S} \ . \tag{2.5}$$

Differentiating the above formula gives the PDF of the formation redshifts for halos. On average, massive halos tend to form later. At fixed mass, the distribution of the formation redshifts is actually wide. In Figure 2.3, the predictions from EPS (solid lines) are compared with the measurements from N-body simulations (points) for halos of different mass (indicated by the number of particles N_p in each panel). The prediction from EPS is not exactly the same as the measurements in the simulations (Lin, Jing & Lin, 2003). This is mainly due to the over-simplified assumptions in the EPS formalism.

Halo assembly is expected to determine the halo properties. Using formation times, it has been shown that younger halos on average are less concentrated and more elongated, spin faster, and contain a larger amount of substructures, than their

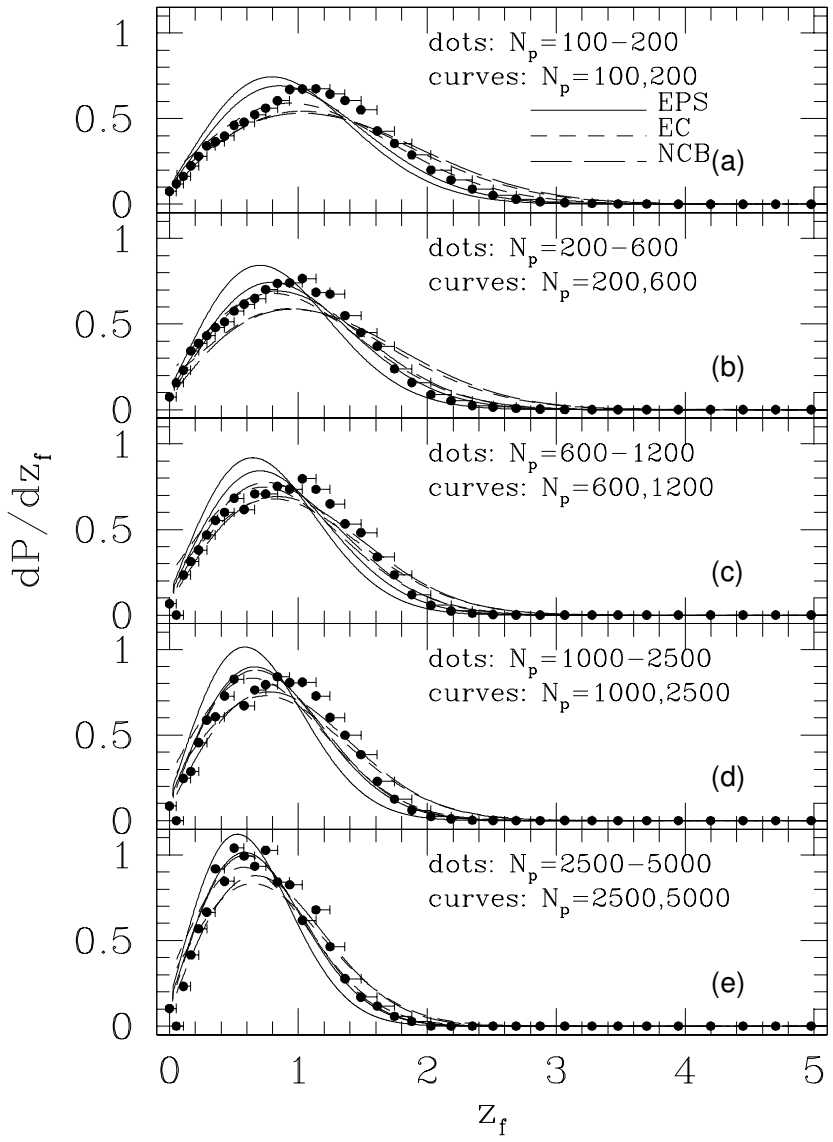

Figure 2.3: Probability distribution function of dark halo formation time in a standard ΛCDM model. Each panel represents dark halos with different mass, indicated by the number $N_{\rm p}$ of particles whose mass is $1.67\times10^{10}\,h^{-1}{\rm M}_{\odot}$ each. Points with error bars are results from an N-body simulation. Solid lines are the prediction of the extended Press-Schechter formalism (EPS); short-dashed lines are the predictions of the ellipsoidal collapse (EC) model (Sheth, Mo & Tormen, 2001); long-dashed lines are the prediction from non-spherical collapse boundary (NCB) model (Chiueh & Lee, 2001). The figure is taken from Lin, Jing & Lin (2003).

older counterparts of the same mass (e.g. Gao et al., 2004; Allgood et al., 2006; Hahn et al., 2007; Wang et al., 2011).

2.1.3 Substructures

In reality, the internal structures of halos are not smooth. Besides the most massive bound structure, which is usually called main halo or distinct halo, there are many small self-bound structures called substructures. Substructures are mainly the remnants of mergers. The evolution of substructures include key information for understanding the evolution of the associated galaxies. Due to the gravitational effects originated by the hosts, subhalos usually experience significant mass loss during/post mergers (van den Bosch, Tormen & Giocoli, 2005). The dominating mechanisms are dynamical friction and tidal stripping. The encounters between subhalos may happen as well. All of these are going to alter the un-evolved subhalo mass function, resulting in an evolved subhalo mass function that deviates from the un-evolved one. According to Angulo et al. (2009), the evolved subhalo mass function can be described by an universal form:

$$\frac{dN}{d\ln(m/M_0)} = A\left(\frac{m}{M_0}\right)^{\alpha} \exp\left[-\frac{1}{\sigma^2}\left(\frac{m}{M_0}\right)^2\right] , \tag{2.6}$$

where the best fitting parameters are $A \approx 2$, $\alpha \approx -0.9$, and $\sigma \approx 0.16$. And it is independent of the mass and redshift of the host halo. The substructure mass fraction increases with the halo mass since massive halos usually undergo more mergers (Zentner & Bullock, 2003).

Previously, people assumed that the accreted subhalos are just like other normal hosts before accretion (van den Bosch et al., 2008; Wetzel, Tinker & Conroy, 2012; Wetzel et al., 2013). In Chapter 6, I am going to extend the mass assembly history study to subhalos and explore the specific feature of the z_f distribution for subhalos before accretion.

2.2 Assembly bias

A generic prediction of the EPS formalism is that halo bias depends strongly on mass (see Section 1.4.3). However, this does not neccessarily mean that for a halo of a given mass, the bias is totally determinded by its mass. In fact, Sheth & Tormen (2004) found that halos in denser region tend to form a little bit earlier than halos of the same mass in less dense region using the statistics of the marked correlation. Subsequent studies in simulations found various dependence of halo properties on environment for fixed mass. The fact that halo clustering properties

depend on the assembly history besides mass alone is usually referred as "assembly bias".

2.2.1 Environmental indicators

In the literature, there exist various indicators of the LSS environments. Here I am going to summarize the most commonly used ones.

- Halo bias(halo clustering): $b = \xi_{hm}/\xi_{mm}$. Halo bias depends on the mass and redshift(see Section 1.4.3). For the study on assembly bias using halo clustering, see Gao, Springel & White (2005) and Jing, Suto & Mo (2007).

- Overdensity: $\delta = \rho/\bar{\rho} - 1$. In application, there are several ways to determine the overdensity. Typically, the density field can be divided into cubic grids, with the density on each grid assigned by the cloud-in-cell interpolation scheme in the N-body simulations. The overdensity centered on a halo within a sphere of radius R, δ_R, can be gotten by summing up the contributing grids. Based on this, δ_{R-FOF} can be further defined by substracting the FOF halo mass of the central halo within the sphere (Fakhouri & Ma, 2009). Another method is to count all halos, both distinct and subhalos with $V_{max} > 120\,\mathrm{km\,s^{-1}}$ (which is the lowest V_{max} value of a complete halo catalog in their study and makes the sampling of the environments to the maximum accuracy), within a sphere of $2\,h^{-1}$Mpc (which is larger than the virial radius of the most halos and represents more local environment) (Hester & Tasitsiomi, 2010).

- Mass tidal field: indicated by tidal tensor $T_{ij} = \partial_i\partial_j\phi$, where ϕ is the gravitational potential and can be gotten by solving the Poisson equation, $\nabla^2\phi = 4\pi G\rho_m\delta$. The eigenvalues satisfy $\lambda_1 > \lambda_2 > \lambda_3$. And the number of the positive eigenvalues can be used to classify the environment where a halo resides. If all three eigenvalues are positive, then we say the halo lives in a cluster. If two or one of them are positive, the region is defined as filament or sheet, and the region with three negative eigenvalues is defined as void. Clearly, positive eigenvalues indicate compressing and negative values indicate stretching from surroundings (Hahn et al., 2007).

- Halo tidal field: indicated by eigenvalues $t_i (i = 1, 2, 3)$ and eigenvectors $\boldsymbol{t}_1$, $\boldsymbol{t}_2$, and $\boldsymbol{t}_3$. $\boldsymbol{t}_1$ corresponds to the stretching direction(the direction where the tidal force reaches maximum) and $\boldsymbol{t}_3$ corresponds to the compressing direction (Wang et al., 2011). The detailed calculation of halo tidal field and its advantages can be found in Section 5.1.3.

- Velocity shear tensor: $\Sigma_{ij} = -\frac{1}{2H(z)}(\frac{\partial v_i}{\partial r_j} + \frac{\partial v_j}{\partial r_i})$, where $i = x, y$, and z, and v_i denotes the velocity field. Eigenvectors are $\boldsymbol{e}_i (i = 1, 2, 3)$. $\boldsymbol{e}_1$ indicates the fastest collapse direction and $\boldsymbol{e}_3$ indicates the slowest collapse direction (Libeskind, Hoffman & Gottlöber, 2014).

Comparing with halo bias and overdensity, tidal field clearly includes richer information of the LSS environment by using both the eigenvalues and the eigenvectors. Wang et al. (2011) studied the correlations between a number of halo properties and the halo tidal field, and found significant correlations between the local halo tidal fields and all the halo properties they studied, including half-mass assembly time, spin, axis ratio, and substructure abundance. In particular, they found that the halo tidal field is the primary environmental effect shaping most of the halo intrinsic properties, while other commonly used environmental indicators, such as the local mass density and the morphology of the LSS, are secondary in that their effects operate mainly through their correlations with the tidal field. Among the two tidal field indicators, halo tidal field has the advantage of being easily applied in the observations by definition.

Forero-Romero, Contreras & Padilla (2014a) studied the alignments of the shape, angular momentum and peculiar velocities of dark matter haloes with velocity field and tidal field separately. For example, they found that the major axis of a halo lies parallel with the minor eigenvector axis of the mass tidal field, while it aligns with the largest eigenvector of the velocity shear for massive halos. They concluded that the two cosmic web indicator describe complementary physical aspects of the environments.

2.2.2 Halo assembly bias

The effects of environments on halos can be revealed through various aspects. Gao, Springel & White (2005) found in N-body simulations, at fixed halo mass, the clustering signal for the old population is stronger than the young population, see Figure 2.4. Further studies revealed more dependence of halo properties on the environment at fixed mass. For example, studies show that at low mass end, halos with high concentration tend to cluster more, while this trend is inverted at high mass end, i.e. halos with low c cluster more strongly (Gao & White, 2007; Jing, Suto & Mo, 2007; Wechsler et al., 2006). And halos in dense region tend to have higher merger rates (Fakhouri & Ma, 2009). Coming to the dynamical properties, halos with high angular momentum are more clustered than those with low angular momentum. And halos which are more spherical or oblate shapes tend to live in a more clustered way (Bett et al., 2007; Gao & White, 2007; Faltenbacher & White, 2010). Especially, Faltenbacher & White (2010) found the strongest environmental effects when considering the dynamical properties, such as the

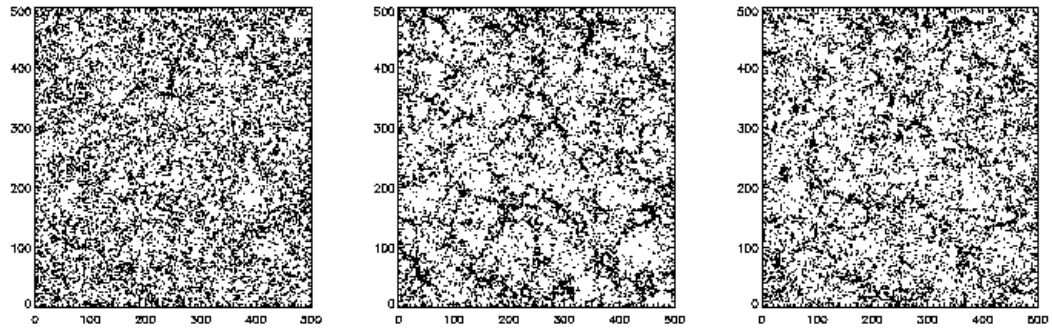

Figure 2.4: From left to the right: the spatial distribution of the 10% youngest, 10% oldest halos and dark matter. The region plotted is a $30\,h^{-1}$Mpc thick slice within Millennum Simulation. Only halos that contain 100-200 particles are plotted. The figure is taken from Gao, Springel & White (2005). The young (left panel) halo population is less clustered (more diffuse) than the dark matter (right panel), while the old (middle panel) halo population is more clustered than the dark matter.

anisotropy parameter, β, that is, the halos with more isotropic internal velocity structure cluster more.

Attempts have been made to understand the environmental effects on halo properties from various perspectives (Wang, Mo & Jing, 2007; Sandvik et al., 2007; Keselman & Nusser, 2007; Desjacques, 2008; Dalal et al., 2008; Fakhouri, Ma & Boylan-Kolchin, 2010; Lacerna & Padilla, 2011, 2012; Li et al., 2013; Paranjape, Hahn & Sheth, 2017; Musso & Sheth, 2014; Hahn et al., 2009). The concentration (age) dependence of clustering at massive end can be explained by peak statistics (Dalal et al., 2008), or the correlated excursion set formalism (Musso & Sheth, 2014). However, at low mass end, the environmental dependence is believed to mainly arise from the fact that small halos lie in the vicinity of large halos, suggesting that their accretion may be suppressed or even truncated by the large scale tidal field (Wang, Mo & Jing, 2007; Dalal et al., 2008; Hahn et al., 2009). Recently, by introducing a anisotropy parameter for the environment, i.e. whether a halo lies in filamentary or more isotropic region, Paranjape, Hahn & Sheth (2017) managed to explain the "assembly bias" phenomenon consistently across the whole mass range. This kind of study might be helpful in incorporating "assembly bias" in the analytic models.

However, a detailed understanding of how environmental effects shape the structure and dynamics of dark matter halos is still lacking. In Chapter 5, I am going to show one of my projects that provides a new perspective for understanding the "assembly bias" by linking the halo accretion history with its current dynamical

properties.

Chapter 3

Angular Momentum of Halo and Galaxy

Angular Momentum is an important property of a dark matter halo. It plays a crucial role in the process of galaxy formation. It's one of the key ingredients that determine the formation history and final type of galaxies. In this chapter, first I am going to give a brief review of the theoretical study on the origin, characteristics, and the internal distribution of halo angular momentum. Then I will give an introduction of the studies on angular momentum in galaxies.

3.1 Halo angular momentum

3.1.1 Tidal torque theory

As first pointed out by Hoyle (1949), the angular momentum of a proto-galaxy may be originated from the tidal field of its surrounding mass distribution. Later Peebles (1969) gave a qualitative analysis within the framework of gravitational instability. This led to the TTT for the origin of the angular momentum within hierarchical structure formation cosmology (Doroshkevich, 1970; White, 1984). Here I am going to give a consistent description following Porciani, Dekel & Hoffman (2002a).

Consider a proto-halo, a patch of matter occupying an Eulerian volume V_E that is destined to end up in a virialized halo, the angular momentum at time t is

$$\mathbf{J}(t) = \int_{V_E} \rho_m(\mathbf{r}, t)\,[\mathbf{r}(t) - \mathbf{r}_{\rm cm}(t)] \times [\mathbf{v}(t) - \mathbf{v}_{\rm cm}(t)]\,d^3r\,, \tag{3.1}$$

where $\mathbf{r}$ and $\mathbf{v}$ are the proper position and peculiar velocity, and the subscript cm denotes center-of-mass. The term proportional to $\mathbf{r}_{\rm cm}$ doesn't contribute to $\mathbf{J}(t)$

and will not be considered further more. Rewrite the above equation in comoving units by using $\mathbf{x} = \mathbf{r}/a(t)$, and $\mathbf{v} = a(t)d\mathbf{x}/dt$ and replacing $\rho_m(\mathbf{r}, t)$ with the density contrast $\delta(\mathbf{x}, t) = \rho_m(\mathbf{x}, t)/\bar{\rho}_m(t) - 1$, to obtain

$$\mathbf{J}(t) = \bar{\rho}_m(t)a^5(t) \int_{V_E} [1 + \delta(\mathbf{x}, t)] \, [\mathbf{x}(t) - \mathbf{x}_{\rm cm}(t)] \times \dot{\mathbf{x}}(t) \, d^3x \,, \tag{3.2}$$

where $a(t)$ is the cosmic expansion factor and the dot denotes a derivative with respect to cosmic time t. Note that in the matter dominated era, $\bar{\rho}_m a^3(t) = \rho_0 a_0^3 = constant$, where the variables with subscript 0 means the values at the present time.

It is more convenient to think the fluid dynamics with Lagrangian description. The comoving Eulerian position of a fluid element can be written as the sum of its initial Lagrangian position $\mathbf{q}$ and a displacement $\mathbf{S}$ caused by the gravitational perturbations: $\mathbf{x} = \mathbf{q} + \mathbf{S}(\mathbf{q}, t)$. When fluctuations are sufficiently small, or when the flow is properly smoothed, the mapping $\mathbf{q} \to \mathbf{x}$ is reversible. Then the Jacobian determinant $\|\partial\mathbf{x}/\partial\mathbf{q}\|$ does not vanish, and the continuity equation implies $1 + \delta[\mathbf{x}(\mathbf{q}, t)] = \|\partial\mathbf{x}/\partial\mathbf{q}\|^{-1}$. Substituting in equation (3.2) one obtains

$$\mathbf{J}(t) = a^2(t) \, \bar{\rho}_0 a_0^3 \int_{V_L} \left[\mathbf{q} - \bar{\mathbf{q}} + \mathbf{S}(\mathbf{q}, t) - \bar{\mathbf{S}}\right] \times \dot{\mathbf{S}}(\mathbf{q}, t) \, d^3q \,, \tag{3.3}$$

where V_L is the Lagrangian region corresponding to V_E.

The displacement $\mathbf{S}$ is spelled out using the *Zel'dovich* approximation (see Section 1.2.3), $\mathbf{S}(\mathbf{q}, t) = -D(t) \, \nabla\Phi(\mathbf{q})$, where $\Phi(\mathbf{q}) = \phi(\mathbf{q}, t)/\left[4\pi G\bar{\rho}(t)a^2(t)D(t)\right]$ (with $D(t)$ the linear growth factor), and $\phi(\mathbf{q}, t)$ is the gravitational potential. Substituting in equation (3.3) one obtains

$$\mathbf{J}(t) = -a^2(t)\dot{D}(t) \, \bar{\rho}_0 a_0^3 \int_{V_L} (\mathbf{q} - \bar{\mathbf{q}}) \times \nabla\Phi(\mathbf{q}) \, d^3q \,. \tag{3.4}$$

We see explicitly the growth rate is $J \propto a^2(t)\dot{D}(t)$, which is $\propto t$ in an EdS universe. Using Gauss's theorem, this equation can be converted to an integral over the surface Σ_L, of V_L

$$\mathbf{J}(t) = -a^2(t)\dot{D}(t) \, \bar{\rho}_0 a_0^3 \int_{\Sigma_L} (\mathbf{q} - \bar{\mathbf{q}})\Phi(\mathbf{q}) d\mathbf{S} \tag{3.5}$$

Note that here $\mathbf{S}$ means the surface, different from the displacement $\mathbf{S}(\mathbf{q}, t)$ defined above. $\mathbf{J}$ vanishes to the first order if V_L is spherical or if Σ_L is an equi-potential surface of Φ.

Next, let's assume that the potential is smooth enough within the volume V_L that it can be expanded in a Taylor expansion around the center of mass $\bar{\mathbf{q}}$ to the second-order:

$$\Phi(\mathbf{q}) \simeq \Phi(\bar{\mathbf{q}}) + \left.\frac{\partial\Phi}{\partial q_i}\right|_{q_i=\bar{q}_i} (q_i - \bar{q}_i) + \frac{1}{2} \left.\frac{\partial^2\Phi}{\partial q_i \partial q_j}\right|_{q_i=\bar{q}_i} (q_i - \bar{q}_i)\,(q_j - \bar{q}_j) \tag{3.6}$$

Substituting in equation (3.4), one obtains the basic TTT expression for the ith Cartesian component:

$$J_i(t) = -a^2(t)\dot{D}(t)\,\epsilon_{ijk}\,T_{jl}\,I_{lk}\,, \tag{3.7}$$

where ϵ_{ijk} is the anti-symmetric tensor with $\epsilon_{123} = 1$,

$$T_{ij} = \left.\frac{\partial^2\Phi}{\partial q_i \partial q_j}\right|_{\mathbf{q}=\bar{\mathbf{q}}} \tag{3.8}$$

is the tidal tensor at $\bar{\mathbf{q}}$, and

$$I_{ij} = \bar{\rho}_0 a_0^3 \int_{V_L} (q_i - \bar{q}_i)\,(q_j - \bar{q}_j)\,d^3q \tag{3.9}$$

is the inertia tensor of the matter in V_L. Both T_{ij} and I_{ij} are evaluated at fiducial time t_i.

Thus, as long as the principle axis of T_{ij} and I_{ij} are different from each other, $\mathbf{J}$ is non-zero due to the coupling of the quadruple moment of mass distribution of the protohalo with the tidal field generated by its neighboring density fluctuation. This torque depends on the protohalo shape, the external tidal field and the misalignment between them.

One of the key assumptions of TTT is that non-linear evolution doesn't contribute too much to the growth of the halo angular momentum. This turns out to be a main issue. Porciani, Dekel & Hoffman (2002a) and Porciani, Dekel & Hoffman (2002b) have tested the performance and validity of several assumptions made in TTT using N-body simulations. They found that the predictions of TTT for the angular momentum amplitude match with the spin amplitude of the virialized halos today on average, if linear growth is assumed to last until $\sim 1/3$ age of the universe, or $\sim 55\%$-70% of the halo turning around time. However, the scatter is comparable to the amplitude itself. When it comes to the direction of the angular momentum, TTT gives a rather poor prediction with a mean error of $\sim 50^\circ$ for the present day halos, which is mainly caused by the non-negligible non-linear effect.

3.1.2 Spin parameter

A traditional way to characterize the angular momentum of a halo is the dimensionless spin parameter (Peebles, 1969),

$$\lambda = \frac{J|E|^{1/2}}{GM^{5/2}}\,, \tag{3.10}$$

where J, E, and M are the total angular momentum, energy and mass of the halo. λ characterizes the overall importance of rotation relative to the random motion in the system.

Assuming a spherical halo, its total energy can be obtained from the virial theorem, $E = -K$, with all its particles on circular orbits:

$$E = -4\pi \int_0^{r_h} \frac{\rho(r)V_c^2(r)}{2} r^2 dr \equiv -\frac{M_h V_h^2}{2} f_c \,, \tag{3.11}$$

where $V_h = V_c(r_h)$ is the circular velocity at r_h and f_c is a parameter that depends on the halo internal density distribution. For a halo with NFW profile,

$$f_c = \frac{c[1 - 1/(1+c)^2 - 2ln(1+c)/(1+c)]}{2[c/(1+c) - ln(1+c)]^2}, \tag{3.12}$$

with c the concentration parameter.

In Bullock et al. (2001), they have defined another spin parameter

$$\lambda' = \frac{J}{\sqrt{2} M_h V_h r_h}, \tag{3.13}$$

which has the advantage of no needing to calculate the halo energy. And it's related to the one defined by equation (3.10) through $\lambda' = \lambda f_c^{-1/2}$. A detailed comparison between those two definitions for halos of different mass, redshift within varying cosmology in N-body simulations can be found in Rodríguez-Puebla et al. (2016).

Numerical simulations show that the distribution of this spin parameter is very well fitted by a log-normal distribution,

$$p(\lambda) = \frac{1}{2\pi\sigma_{ln\lambda}} \exp\Big[- \frac{ln^2(\lambda/\bar{\lambda})}{2\sigma_{ln\lambda}^2} \Big] \frac{d\lambda}{\lambda} \,, \tag{3.14}$$

with $\bar{\lambda} \sim 0.035$ and $\sigma_{ln\lambda} = 0.5$. Besides, the mean and variance of this distribution is independent of mass, redshift, and cosmology (Barnes & Efstathiou, 1987; Bullock et al., 2001; Macciò et al., 2007). Further studies show that halos in denser environment tend to have higher spin, see Gao & White (2007) and Bett et al. (2007).

3.1.3 Internal distribution

The angular momentum profile inside a halo is an important ingredient for modelling the mass distribution of disk galaxies. In fact, Bullock et al. (2001) found an universal angular momentum profile using N-body simulations for galactic halos:

$$M(< j) = M_h \frac{\mu j}{j_0 + j}, \quad \mu > 1 \,, \tag{3.15}$$

where j stands for the specific angular momentum (defined as the angular momentum per unit mass) projected to the direction of the total angular momentum(since

the direction of different shells are not perfectly aligned with each other), j_0 and μ are fitting parameters which describe the shape of the profile, and $M(< j)$ is the halo mass with specific angular momentum less than j. By setting $M(< j) = M_h$, we can explicitly get $j_{max} = j_0/(\mu - 1)$. The total (mean) angular momentum is $j_h = j_0 b(\mu) = \sqrt{2}\lambda' r_h V_h$, with $b(\mu) = -\mu ln(1 - \mu^{-1}) - 1$. Thus the universal distribution is fully characterized by one shape parameter (μ or j_0) and λ'.

A more direct way to see the inner distribution is to measure j in spherical shells. Barnes & Efstathiou (1987) found roughly $j(r) \propto r$, while a more detailed study by Bullock et al. (2001) shows that within the virial region of a halo, we have

$$j(r) \propto r^{\alpha} \tag{3.16}$$

with $\alpha = 1.1 \pm 0.3$, which implying a nearly constant rotational velocity and

$$j(M) \propto M^{\beta} \tag{3.17}$$

with $\beta = 1.3 \pm 0.3$, where M is the mass enclosed within the shell.

3.2 Angular momentum in galaxies

3.2.1 General properties of LTGs and ETGs

Galaxies show a variety of properties in luminosity, color, morphology, metallicity, SFH etc. The first classification scheme was proposed by E. Hubble in 1926 based on the morphology (Hubble, 1926; Sandage, 1961), with some further development by de Vaucouleurs (1974). It is usually referred to as the Hubble sequence or Hubble fork (see Figure 3.1). Along this sequence from left to right, the morphology of galaxies change gradually from smooth ellipticals to disks with spiral arms. There exists this intermediate class, called S0 or lenticulars, with smooth light distribution yet disky. Spiral galaxies are further divided into barred and normal (without bars) spirals. And they show less tight arm structures and less dominating bulges toward the end of the sequence until they reach irregulars. In general, Irregulars are taken as an extension of the spiral class, with no clearly recognized bulges or disks. Historically, ellipticals and lenticulars together are also refereed as ETGs, while LTGs are used to refer spirals and irregulars. Note that even though the Hubble sequence has encompassed a majority of the galaxy morphology, peculiar galaxies like the Antennae galaxies (also referred as NGC4038/4039), which has a “heart shaped” appearance with two long tidal tails indicating strong dynamical interaction, are not included.

A very important observational fact about Hubble squence is that, galaxies show systematical changes in color, luminosity, surface brightness, gas content,

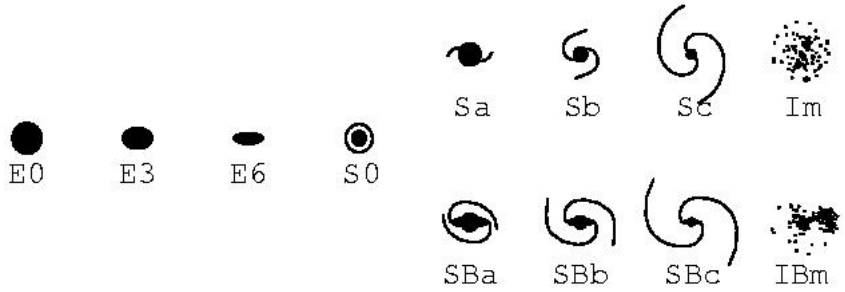

Figure 3.1: Hubble sequence of galaxy morphologies. The figure is taken from Abraham (1998).

star formation activity, bulge fraction B/T and mass surface density along the sequence. In the following, I am going to give a brief summary of some of the properties of LTGs and ETGs.

Surface brightness profile

The one dimensional surface brightness profile of a galaxy along its semi-major axis can be described by a Sérsic profile (Sérsic, 1963):

$$I(R) = I_0 \exp(-kR^{1/n}) \tag{3.18}$$

where I_0 is the central surface brightness, n is the so called Sérsic index which indicates the concentration of the profile (larger n represents more concentrated light profile distribution). When $n = 4$, this profile recovers the De Vaucouleurs' law (de Vaucouleurs, 1948) for ellipticals:

$$I(R) = I_0 \exp\Big[-k_n (R/R_e)^{1/4} \Big] = I_e \exp\Big[-k_n [(R/R_e)^{1/4} - 1] \Big] \tag{3.19}$$

where R_e is the effective radius within which lying half of the total light, and $I_e = I(R_e)$.

And $n = 1$ gives the exponential profile,

$$I(R) = I_0 \exp(-R/R_d), \;\; I_0 = \frac{L}{2\pi R_d^2} \tag{3.20}$$

which is a good description of the disks of spirals. L represents the total luminosity and R_d is the exponential scale length satisfying $R_d \simeq R_e/1.67$.

Kinematics

Stars and gas in the disks of spirals usually rotate in a circular orbit, thus the kinematics in disks can be characterized by the rotation curve $V(R)$, expressing

the rotation velocity as a function of the distance from the galactic center. Observationally, $V(R)$ can be obtained with long-slit spectroscopy (Pizzella et al., 2004) and IFS of ionized gas (Glazebrook, 2013), e.g. H_α emission line. Further more, it can be measured out to large distance due to the more extended HI gas using 21-*cm* observations (van Albada et al., 1985; Bosma, 1981; Shostak, 1973; Begeman, 1989; de Blok et al., 2008). Although $V(R)$ varies from galaxy to galaxy, it's characterized by two general features, a rise at small radii and flat velocity profile at large radii, with the amplitude and the central rise sharpness decreasing with lower luminosity and later types (Rubin et al., 1985). The flat feature at large distance provides an indirect evidence for DM (Rubin, Ford & Thonnard, 1980). The kinematics of bulge is complex and hard to get due to the uncertainty of disk-bulge decomposition.

In contrast, rotation (characterized by V_{rot}) is less important relative to the random motion (characterized by velocity dispersion σ) in ellipticals. Both V_{rot} and σ can be obtained with long-slit spectroscopy and IFS of stellar absorption lines (Thomas et al., 2009; Cappellari et al., 2011). Cappellari (2016) gives a comprehensive review on the kinematic and structure study on ETGs. The kinematics of ETGs is characterized by a velocity dispersion profile that features a peak at the center and becomes flat at larger radii (van den Bosch, Jaffe & van der Marel, 1998). More detailed kinematics studies reveal that there are two typical types of ellipticals. One is the slow rotator, which is usually bright, with boxy isophote (indicating triaxial structure), and supported by anisotropic velocity dispersion (Kormendy & Bender, 1996); the other one is the fast rotator, which is fainter, with disky isophote (indicating axisymmetric), and higher rotation velocity (Davies et al., 1983). The two classes can be approximated separated by $V_{rot}/\sigma \approx 0.4$ (Cappellari et al., 2007) or the spin parameter λ_{R_e} (note this parameter is different from the spin parameter λ defined in Section 3.1.2) measured within the half-light isophote (Emsellem et al., 2007, 2011).

Stellar population

In general, ellipticals are massive and redder comparing to spirals, showing little ongoing star formation activity. The color becomes redder with increasing luminosity, which can be attributed to either metallicity or age. By using standard Lick absorption lines (Trager et al., 1998), such as H_β (sensitive to ages) and Mgb, Fe5270 or Fe5335 (sensitive to stellar metallicity), the age-metallicity degeneracy can be broken (Thomas & Maraston, 2003). And it shows that stellar populations of massive (more luminous) ellipticals are both older and more metal rich. In contrast, spirals are bluer, and contain mainly young and relatively metal poor stellar population.

Both ETGs and LTGs display color gradient, with the outer region bluer than

the central region (Peletier, Davies & Illingworth, 1990; de Jong, 1996). Similar gradient also exist for metallicity, with the outer region showing lower metallicity than the central part (Smartt & Rolleston, 1997; Ma et al., 2017). Note that no age gradient is found for the local ellipticals (Rawle et al., 2008). On the contrary, the populations in the outer region of spirals tend to be younger (Cunow, 2004). These color, metallicity, and age gradient of spirals suggest an inside-out formation scenario, which is a natural prediction of the classic disk formation model (see Section 3.2.2). However, further verification are needed from observations.

Moreover, ETGs show a phenomenon called alpha enhancement, characterized by the α elements (e.g., O, Ne, Mg, Si, S, Ar, Ca, and Ti) to Fe ratio, [α/Fe]. α elements are produced by Type II supernova explosions of massive stars, while a substantial fraction of the Fe comes from Type Ia supernovae explosion (Thielemann, Nomoto & Hashimoto, 1996). Hence, [α/Fe] quantifies the relative importance of Type II and Type Ia supernovae (Matteucci & Greggio, 1986; Thomas, Greggio & Bender, 1998) and therefore carries information about the timescale over which star formation occurs. A detailed chemical evolution simulation that links [α/Fe] and star formation timescale can be found in Pipino & Matteucci (2004). Indeed, observations of [α/Fe] in ETGs show that most of the stars should form in a short time scale $\Delta t \lesssim$ 1Gyr. All these are consistent with passive evolution of a roughly single stellar population in ETGs.

Scaling relationships

- **Tully-Fisher Relation:** spirals obey a well-defined scaling relation between luminosity L and rotational velocity $V_{\rm max}$, expressed in the form

$$L = AV_{max}^{\alpha} \ , \tag{3.21}$$

  where A is the zero-point and α is the slope. This tight relation puts an important constraint on galaxy formation and evolution theory.

- **Fundamental Plane:** ellipticals tend to lie a in 3-D plane defined by

$$\log R_e = a\log\sigma_0 + b\log\langle I\rangle_e + c \ , \tag{3.22}$$

  where R_e is the effective radius, σ_0 is the central velocity dispersion, $\langle I\rangle_e$ is the mean surface brightness within R_e, and a, b, c are constants varying with photometric bands. Two projections of this 3-D plane are Faber-Jackson relation and D_n-σ relation (D_n is a parameter indicating the size), that is, ellipticals with larger dispersion are brighter and larger.

3.2.2 Formation of LTGs and ETGs

To understand the above galaxy properties, detailed model on galaxy formation is needed. White & Rees (1978) first proposed the two stage galaxy formation theory within the hierarchical structure formation picture: dark matter halos form through mergers/accretion; baryons/gas condense in the potential well produced by DM halos through radiative cooling, forming the luminous galaxies. Feedbacks are needed in order to explain the overall low galaxy formation efficiency. Although this theory is far from complete and precise, it did provide the basic ideas for modern galaxy formation theory, see Mo, van den Bosch & White (2010) for more information.

Classic disc formation picture

In this section, I am going to present the standard disc formation picture within ΛCDM framework following mainly Mo, Mao & White (1998).

Several key assumptions are made: i) the mass and angular momentum of a disc is a fixed fraction of its halo; ii) the disc is thin and rotation supported in centrifugal equilibrium; iii)only a disc that is dynamically stable corresponds to a real galaxy disc; and iv) baryons and DM are very well mixed initially. Thus the angular momentum of the disc is expected to have the same origin as that of the DM halo, see Section 3.1.1. And the angular momentum per unit mass, i.e. specific angular momentum, of those two components are expected to be the same before they collapse (Fall & Efstathiou, 1980). The angular momentum properties of halos are briefly summarized in Section 3.1.

Light distribution profile in discs is given by equation (3.20), which means that the surface mass density profile follows a similar exponential expression:

$$\Sigma(R) = \Sigma_0 \exp(-R/R_d) \ , \tag{3.23}$$

where Σ_0 is the central surface mass density and R_d is the scale length. Thus the mass profile of a disk is

$$M_d(R) = \int_0^R 2\pi r \Sigma(r) dr = M_d - M_d(1 + R/R_d)\exp(-R/R_d) \ , \tag{3.24}$$

where M_d is the total mass in disk, $M_d = \int_0^\infty 2\pi R\Sigma(R)dR = 2\pi\Sigma_0 R_d^2$.

The rotation velocity V(R) is contributed by the disc and DM:

$$V^2(R) = V_d^2(R) + V_{DM}^2(R) \ , \tag{3.25}$$

where $V_{DM}(R)$ is rotation curve due to the existence of DM, and $V_d(R)$ is the rotation curve of the disc. Suppose $V_{DM}(R)$ is unaffected by the disc formation,

using equation (1.51) and (1.52), we have

$$V_{DM}(R) = \sqrt{\frac{GM_{DM}(R)}{R}} = V_h\Big[\frac{1}{x}\frac{ln(1+cx) - cx/(1+cx)}{ln(1+c) - c/(1+c)}\Big]^{1/2} , \tag{3.26}$$

where $x \equiv R/R_h$. As for the disc, we have

$$V_d^2(R) = R\frac{\partial\Phi}{\partial R} = -4\pi G\Sigma_0 R_d y^2[I_0(y)K_0(y) - I_1(y)K_1(y)] , \tag{3.27}$$

where the potential well Φ for the exponential infinitesimally thin disc given by Toomre (1963). $y = R/2R_d$, I_n and K_n are the modified Bessel functions of the first and second kinds respectively.

With the rotation curve in hand, the total angular momentum of the disc can be written,

$$J_d = \int_0^{r_h} V(r)r\Sigma(r)2\pi r dr \tag{3.28}$$

$$= M_d R_d V_h \int_0^{r_h/R_d} e^{-\mu}\mu^2\frac{V(R_d\mu)}{V_h}d\mu . \tag{3.29}$$

We assume this angular momentum is a fraction of that of the halo, $J_d = j_d J_h$, where J_h is related to the spin parameter λ by equation (3.10). If we further assume that the disc mass is a fraction of halo mass, $M_d = m_d M_h$, we obtain the disc size to be

$$R_d = \frac{1}{\sqrt{2}}(\frac{j_d}{m_d})\lambda r_h f_c^{-1/2} f_R , \tag{3.30}$$

here I apply the fact that $R_h \gg R_d$ and $f_R = \left[\frac{1}{2}\int_0^\infty e^{-\mu}\mu^2\frac{V(R_d\mu)}{V_h}d\mu\right]^{-1}$.

Note that the last "=" of equation (3.26) only stands when the DM mass profile is independent of the gravitational force of the baryons, which is not true. The more realistic DM mass profile can be obtained as following. Assuming that the halo responds adiabatically to the disc formation (Blumenthal et al., 1986), then angular momentum is a conserved quantity. For an idealized spherical halo with the DM particles in circular orbits, the conserved quantity reduces to specific angular momentum, $RV(R)$. Thus it can be further more reduced to $RM(R)$. Consider a dark matter particle with initial radius R_i ends up at a radius R_f, then

$$R_f M_f(R_f) = R_i M_i(R_i) , \tag{3.31}$$

where $M_i(R_i)$ is the initial total mass profile and $M_f(R_f)$ is the final total mass profile. If we define the disc to total mass fraction as $m'_d \equiv \frac{M_d}{(M_d+M_{DM})}$, then the final

total mass within R_f, $M_f(R_f)$, which is the sum of the disc mass and the DM mass initially within R_i, can be written down as

$$M_f(R_f) = M_d(R_f) + M_i(R_i)(1 - m'_d) \ . \tag{3.32}$$

Since we assumed that the baryons and DM are very well mixed initially, baryons should have the same density profile as DM initially. Further more, those baryons that don't end up in the disc are assumed to have the same distribution as the DM. So $M_i(R_i)$ can be gotten by equation (1.51). Combining equations (3.31) and (3.32), we can get a relationship between R_f and R_i, and the modified DM mass profile $M_{DM}(R) = M_f(R) - M_d(R)$ can be obtained. In this case, the rotation velocity contributed by DM is

$$V_{DM}(R) = \sqrt{\frac{G[M_f(R) - M_d(R)]}{R}} \ . \tag{3.33}$$

Given M_h, c, λ, j_d and m_d, then R_d and $V(R)$ can be solved by iteration. Note that M_h, c, λ in the model is given by the N-body simulation, while the values of j_d and m_d have to estimated by comparing with the observation data. In order to match the local disc properties, Mo, Mao & White (1998) found that m_d needs to be a value of few percent, $m_d = j_d$ should stand, and the assembly redshift for the present day disc needs to be $z \lesssim 1$. With the above assumptions and calculation, the Tully-Fisher relation (including the slope, the scatter and the zero-point) can be recovered very well. In fact, later observation of the star formation efficiency (SFE) of the spirals does match the assumed m_d value here (i.e. $m_d < 0.05$ is required) (Dutton et al., 2010). The low average formation redshift of local spirals is also verified by observation. Requiring $j_d = m_d$ actually implies that the specific angular momentum of discs should be the same/comparable as that of DM halos, and indeed, later study found similar results (Burkert et al., 2016). A natural prediction of the above picture is that high redshift discs are small and dense comparing with the local ones, suggesting an inside-out growth for local spirals (Pezzulli et al., 2015).

The formation of ETGs

The large velocity dispersions imply that ellipticals experience more violent formation process than spirals. Historically, there exist two competing formation scenarios: monolithic collapse scenario (Eggen, Lynden-Bell & Sandage, 1962; Gott & Thuan, 1976) and merger scenario (Toomre & Toomre, 1972). The main difference of those two scenarios are the SFH and the mass assembly time. For the monolithic one, star formation happens as a burst, and the mass assembly happens along; while for the second scenario, both the star formation and the mass assembly

span an extended period of time and mass assembly is usually later than the star formation.

The monolithic collapse scenario was inspired by the fact that ETGs are made of uniformly old stellar populations. It was first proposed by Eggen, Lynden-Bell & Sandage (1962). Depending on whether the star formation time scale is longer or shorter than the free fall time scale, the collapse can be divided into dissipational or dissipationless process. In this scenario, galaxies form through a short time scale at high redshift, which is coincident with their collapse or virialization, and start to evolve passively later on.

The merger scenario began to come up with the study on galaxy interaction done by Toomre & Toomre (1972), where they found the interactions of two spirals can produce structures, such as long tails, seen in peculiar galaxies. They further argued that ETGs are merger remnants of spirals. Current observations do show the imprints of mergers for some galaxies. However, to see whether it is the main formalism in forming ETGs, several issues needed to be understood: i) can mergers of observed galaxies produce remnants that resemble present day ETGs? ii) can the merger rate as a function of progenitor properties and environment, when integrated over redshift, produce the $z = 0$ abundance of ellipticals as a function of stellar mass, age, metallicity, size, velocity dispersion and environments? iii) can the high redshift observation match our expectation for the properties of the progenitors for ETGs?

Mergers can be divided into major mergers (of mass ratio >1/3) and minor mergers (of mass ratio <1/3), see Naab & Burkert (2003). Depending on whether or not gas is involved in the merger events, they can be further classified into "dry merger" (without gas, dissipationless) or "wet merger" (with gas, dissipational, see e.g. Cox et al. 2006). Studies with hydro-dynamical simulations show that low mass ETGs are mainly formed through dissipational (wet) mergers, and massive ETGs are the products of dissipationless (dry) mergers (**?**). The merger scenario seems to fit naturally with the hierarchy structure formation of the DM halos, thus prevails the galaxy formation and evolution theoretical studies for the past decades. Especially, semi-analytic models (SAM) based on cosmological N-body simulations (Kauffmann, 1996; Baugh, Cole & Frenk, 1996; Somerville & Primack, 1999; De Lucia et al., 2006; Kang, van den Bosch & Pasquali, 2007) found qualitatively good agreements with many of the observed correlations for ETGs. They are predicted to be more massive, to be more common in massive halos, and to have older stellar populations.

Various efforts have been done to distinguish those two scenarios. However, it turns out neither of them is able to explain all current observations. More specifically, monolithic collapse explains the roughly passive evolution of a short-time scale star formation for ETGs very well, however it meets difficulties in explaining other observation results. For example, it fails in explaining the mass

growth (Belli, Newman & Ellis, 2014; Man, Zirm & Toft, 2016) and the strong size evolution (van Dokkum et al., 2014; van der Wel et al., 2014) since $z \sim 2$. On the other hand, mergers are still disputative on many open questions, such as the star-formation history, mass assembly process, and structural evolution of massive galaxies. More and more evidence started to favor the importance of "in-situ" process in galaxies. For example, disk instability caused by the internal gravitational instability (Dekel, Sari & Ceverino, 2009) is invoked to explain the formation of small and intermediate mass spheroids systems (Parry, Eke & Frenk, 2009; Porter et al., 2014). While for massive ETGs, recent studies support the two-phase formation scenario (Oser et al., 2010, 2012). In this two-phase scenario, galaxy first experiences an "in-situ" fast growth phase at $z \sim 2$ due to the cold gas inflowing. AGN/SN feedback is triggered later to quench the star formation activity. Thus most ETG progenitors are quiescent already at $z \sim 1$ (Kriek et al., 2016). The second phase is featured mainly with multiple dry minor mergers which increase the size of the galaxies effectively (Naab, Johansson & Ostriker, 2009; Oser et al., 2012). Observationally, Huang et al. (2013) found the multi-component nature of massive galaxies can be understood well with the two-phase assembly history. Further more, Huang et al. (2017b) found the surface mass density profiles of massive galaxies at $0.3 < z < 0.5$ are consistent the two-phase growth history expectation.

3.2.3 Angular momentum of galaxies

As already discussed in Section 3.2.1, galaxies show various properties. However, the more fundamental physical parameters are mass M, energy E and angular momentum J. Especially, the acquisition of the galaxy angular momentum (Danovich et al., 2015) is related with the various astrophysical process in galaxies, such as the gas cooling, star formation, stellar wind, outflows, feedback, galaxy interaction and etc. Studies of galaxy angular momentum can provide further constraints on those process.

Hydro-dynamical simulations are good tools to incorporate all these complexities for angular momentum building up. However, early cosmological hydro-dynamical simulations suffered from a 'catastrophic' angular momentum loss (Steinmetz, 1999; Navarro & Steinmetz, 2000), producing galaxies that are too compact. The employment of more efficient SF feedback are found to be the key solution for this issue (Governato et al., 2007). Now days, hydro-dynamical simulation of single galaxy are able to produce even bulge-less disks (Christensen et al., 2012). The statistical properties and evolution track have been studied with the development of cosmological hydro-simulations like Eagle (Schaye et al., 2015) and Illutris (Vogelsberger et al., 2014b).

Fall (1983) introduced the general diagram of $j_\star$ versus stellar mass $M_\star$ (see

Figure 1 of Romanowsky & Fall 2012), where $j_\star = J_\star / M_\star$ is the stellar specific angular momentum. He found $j_\star \propto M_\star^{5/3}$, and $j_\star$ of ellipticals are 5 times lower than spirals. The simple relation is charged with useful information on galaxy formation. In Chapter 7, I am going to give a self-consistent explanation for this $j_\star$-$M_\star$ relation, using observation scaling relations of ETGs and LTGs.

Part II:

Halo Assembly and Environment

Chapter 4

Dependence of Halo Bias on Mass and Environment

The clustering of galaxies is often used to constrain models of the background cosmology and galaxy formation. In many studies, the Halo Model (Cooray & Sheth, 2002) plays an important role. In the simplest (and most widely used) version of the approach, the clustering of galaxies is determined by a combination of how galaxies populate halos, and the clustering of the halos which host galaxies, and for both ingredients, halo mass is assumed to be the only halo property which matters. Abbas & Sheth (2007) describe one of the first tests of this assumption; they classified galaxies by the number of neighbors within $\sim 8\,h^{-1}$Mpc; measured the clustering signal as a function of environment; and showed that the environmental dependence of clustering was similar to that in a mock catalog in which the galaxy content of a halo was determined completely by halo mass and not environment.

However, they also showed that they were able to model the strength of the clustering signal as a function of environment alone. This finding has recently been confirmed by Pujol et al. (2017). Provided that the environment is defined on a scale that is substantially larger than a typical halo, the clustering signal is a function of environment, and not of halo mass. I.e., at fixed environment, the clustering is independent of halo mass, whereas at fixed mass, the clustering is a strong function of environment. The main goal of this chapter is to provide a more careful derivation of the expression in Abbas & Sheth (2007). A final section discusses how this particular clustering signal is related to what has come to be called Assembly Bias (Sheth & Tormen, 2004), and makes the point that it is useful to distinguish between halo–environment correlations, and whether or not the way galaxies populate halos requires additional correlations.

4.1 Bias of constrained regions

In what follows, it is important to distinguish clearly between the scale associated with halo formation, that on which the environment is defined, and the (typically much larger) scale on which the bias factor is measured. We will use R_h to denote the typical scale for halo formation, R_e to denote the scale on which the environment is defined, and R_0 to denote the scale for large scale bias measurement.

4.1.1 Large scale environment as a constraint

Suppose that we identify those positions in the initial (Gaussian) field which, when smoothed on scale R_e have overdensity Δ_e. Let $S_e \equiv \langle \Delta_e^2 \rangle$. The probability of being centered on such a region is

$$p(\Delta_e) = \frac{\exp(-\Delta_e^2/2S_e)}{\sqrt{2\pi S_e}}. \tag{4.1}$$

The conditional probability that the overdensity, when smoothed on some other scale R_0, is Δ_0, given that it is Δ_e on scale R_e, is

$$p(\Delta_0|\Delta_e) = \frac{\exp^{-(\Delta_0-\mu_{0|e})^2/2S_{0|e}}}{\sqrt{2\pi S_{0|e}}}, \tag{4.2}$$

where

$$\mu_{0|e} \equiv \langle \Delta_0|\Delta_e \rangle = \frac{\langle \Delta_0\Delta_e \rangle}{\langle \Delta_e^2 \rangle}\,\Delta_e \tag{4.3}$$

and

$$S_{0|e} \equiv S_0\,(1 - \langle \Delta_0\Delta_e \rangle^2/S_0 S_e). \tag{4.4}$$

Now, $\langle \Delta_0\Delta_e \rangle$ is the correlation between Δ on the two scales, whereas $\langle \Delta_0|\Delta_e \rangle$ is the cross correlation between the two Δs subject to the constraint that $\Delta = \Delta_e$ on scale R_e. Hence, it is natural to define

$$\langle \Delta_0|\Delta_e \rangle \equiv b_e\,\langle \Delta_0\Delta_e \rangle \qquad \text{where} \quad b_e \equiv \Delta_e/S_e. \tag{4.5}$$

The expression above shows that we should think of the constrained cross-correlation as biasing the unconstrained correlation; the bias is linearly proportional to the

constraint. At the risk of belaboring the point,

$$\begin{aligned}\langle\Delta_0\Delta_e\rangle &= \int \mathrm{d}\Delta_e \int \mathrm{d}\Delta_0\, p(\Delta_e)\, p(\Delta_0|\Delta_e)\Delta_0\Delta_e \\ &= \int \mathrm{d}\Delta_e\, p(\Delta_e)\, \Delta_e\langle\Delta_0|\Delta_e\rangle \\ &= \int \mathrm{d}\Delta_e\, p(\Delta_e)\, \Delta_e\, b_e\langle\Delta_0\Delta_e\rangle \\ &= \langle\Delta_0\Delta_e\rangle \int \mathrm{d}\Delta_e\, p(\Delta_e)\, \frac{\Delta_e^2}{S_e}, \end{aligned} \tag{4.6}$$

where the final integral equals unity. The second expression shows that the unconstrained correlation $\langle\Delta_0\Delta_e\rangle$ is a weighted sum over the constrained cross-correlations $\langle\Delta_0|\Delta_e\rangle$.

Equation (4.5) for the bias is familiar in cosmology from Kaiser (1984). However, there it was introduced in the context of the bias associated with regions which exceed a high threshold in a Gaussian field, though it is often referred to as the 'high peak' limit. The expression above shows that this bias expression is actually associated with a much simpler constraint than either thresholds or peaks: simply that the height *equals* a certain value. The correspondence with peaks is a consequence of the fact that if $\Delta_e \gg \sqrt{S_e}$, then the additional constraints which define a peak do not matter for the bias (because the highest positions in the field are almost certainly also local peaks). While this reason was clear in early work, some more recent papers – arguing that equation (4.5) is particular to peaks – have got the logic backwards.

4.1.2 Small scale overdensity as an additional constraint

The analysis of the previous section shows what one should expect if the constraints are more complicated. E.g., if we add a constraint on a third scale R_h, then

$$\langle\Delta_0|\Delta_e, \Delta_h\rangle = \langle\Delta_0|\Delta_e\rangle + \langle\Delta_0|\Delta_{h|e}\rangle \tag{4.7}$$

where

$$\Delta_{h|e} \equiv \Delta_h - \langle\Delta_h|\Delta_e\rangle. \tag{4.8}$$

Notice that, as there are now two constraints, the bias is the sum of two terms; the form of the expression above suggests that we should think of the prefactors of the correlations with Δ_e and $\Delta_{h|e}$ as being two bias factors. However, $\Delta_{h|e}$ involves both Δ_h and Δ_e, whereas we are typically interested in keeping the effects of these two terms separate. I.e., we seek the coefficients of the terms proportional to $\langle\Delta_0\Delta_e\rangle$

and $\langle\Delta_0\Delta_h\rangle$, respectively. If we define $\nu_e \equiv \Delta_e/\sqrt{S_e}$, and similarly for ν_h, then a little algebra shows that

$$\langle\Delta_0|\Delta_e,\Delta_h\rangle = b_e\,\langle\Delta_0\Delta_e\rangle + b_h\,\langle\Delta_0\Delta_h\rangle \tag{4.9}$$

where

$$b_e = \frac{\nu_e - \langle\nu_e\nu_h\rangle\,\nu_h}{\sqrt{S_e}(1-\langle\nu_e\nu_h\rangle^2)} \tag{4.10}$$

$$b_h = \frac{\nu_h - \langle\nu_h\nu_e\rangle\,\nu_e}{\sqrt{S_h}(1-\langle\nu_e\nu_h\rangle^2)}. \tag{4.11}$$

Note that $b_e \to \Delta_e/S_e$ only when $\langle\nu_e\nu_h\rangle \to 0$ and, in this limit, $b_h \to \Delta_h/S_h$ as well. I.e., when $\langle\nu_e\nu_h\rangle \to 0$, both b_e and b_h have the form of equation (4.5) in their respective variables. Typically, this will happen when $R_e \gg R_h$. The approach to zero will be faster if R_e and R_h are centered on different positions. Furthermore, if $R_0 \gg R_e$ and $R_e \gg R_h$, then we expect $\langle\Delta_0\Delta_h\rangle \ll \langle\Delta_0\Delta_e\rangle$. In this limit $\langle\Delta_0|\Delta_e,\Delta_h\rangle \to \langle\Delta_0|\Delta_e\rangle$: the constraint on Δ_h is irrelevant.

In the present context, equation (4.7) is the more transparent expression because it shows that the constraint on Δ_h will be irrelevant if $\langle\Delta_0|\Delta_{h|e}\rangle = 0$. This happens if $\langle\Delta_0\Delta_h\rangle = \langle\Delta_0\Delta_e\rangle\langle\Delta_e\Delta_h\rangle/S_e$; i.e., if the Δ_0-Δ_h correlation is entirely a consequence of the Δ_0-Δ_e and Δ_e-Δ_h correlations. This holds true for the special case when the smoothing filter used to define Δ on the different scales is sharp in k-space. Such a filter was used extensively in the past, as it leads to Markovian walks with uncorrelated steps, which renders many questions of interest analytically tractable (Bond et al., 1991). For this filter, $\langle\Delta_r\Delta_R\rangle = \langle\Delta_R^2\rangle$ where $R \geq r$. Hence, for this filter $\langle\Delta_0\Delta_h\rangle = S_0$ and $\langle\Delta_0\Delta_e\rangle\langle\Delta_e\Delta_h\rangle/S_e = S_0S_e/S_e = S_0$. So, if Δ_e is fixed, then the constraint from Δ_h is *completely* irrelevant.

More generally, the constraint on Δ_h will be irrelevant if $\langle\Delta_0|\Delta_{h|e}\rangle \ll \langle\Delta_0|\Delta_e\rangle$, i.e., if the amount of correlation between Δ_0 and Δ_h which is not due the Δ_0-Δ_e and Δ_e-Δ_h correlations is smaller than the Δ_0-Δ_e correlation. When $R_0 \gg R_e \gg R_h$, this is very likely to be the case. Hence, except when $|\Delta_{h|e}|$ is very large the fact that Δ_h is constrained will not matter; the cross correlation $\langle\Delta_0|\Delta_e,\Delta_h\rangle$ will be dominated by the first term on the rhs of equation (4.7). Recalling that our choice of subscripts is not accidental, this discussion implies that when $R_e \gg R_h$ then the cross correlation signal of equation (4.7) will be dominated by the correlation with the environment; the halo mass is almost always irrelevant. Halo mass only matters if $|\Delta_{h|e}|$ is large: since Δ_h is typically of order unity, halo mass matters more if Δ_e is very negative (i.e. in underdense regions).

4.1.3 Small scale overdensity and its derivatives as additional constraints

Equation (4.7) serves mainly to illustrate how cross-correlations with the large scale environment generalize as one adds more constraints. Following Musso & Sheth (2012), we are most interested in the case in which the derivatives of Δ_h also matter. In this case,

$$\langle \Delta_0 | \Delta_e, \Delta_h, \Delta'_h \rangle = \langle \Delta_0 | \Delta_e \rangle + \langle \Delta_0 | \Delta_{h|e} \rangle + \langle \Delta_0 | \Delta_{h'|he} \rangle \tag{4.12}$$

and we are again faced with the problem of showing when the first term on the right hand side dominates.

In this context, it is interesting to consider a slightly more general problem in which the derivative on scale R_e is also specified. Then we are interested in $\langle \Delta_0 | \Delta_e, \Delta'_e, \Delta_h, \Delta'_h \rangle$. Musso & Sheth (2014) describe a family of – what they call Markov Velocity – models in which correlations between scales are rather similar to those in ΛCDM models. They show that, for Markov Velocity models,

$$\langle \Delta_0 | \Delta_e, \Delta'_e, \Delta_h, \Delta'_h \rangle = \langle \Delta_0 | \Delta_e, \Delta'_e \rangle; \tag{4.13}$$

i.e., if both Δ_e and Δ'_e are specified, then the smaller scale R_h is irrelevant (see their equation 71). For Markov Velocity models this is an exact, not an approximate, statement. As a result, $\langle \Delta_0 | \Delta_e, \Delta_h, \Delta'_h \rangle$ only depends weakly on R_h, or depends on R_h only for a rather restricted range of scales. The similarity of these models to ΛCDM strongly suggests that $\langle \Delta_0 | \Delta_e, \Delta_h, \Delta'_h \rangle$ in ΛCDM models will also only depend weakly on R_h. I.e., if the environment on scale $R_e \geq R_h$ is fixed, then the large scale bias is approximately independent of halo mass.

4.1.4 General formulation

The lesson from the previous explicit models is clear. If the vector $\mathbf{h}$ includes all the variables which are important for halo formation, then one should express halos as constraints on these variables in the underlying Gaussian field:

$$n(m) = \int \mathrm{d}\mathbf{h}\, p(\mathbf{h})\, C_m(\mathbf{h}), \tag{4.14}$$

where $C_m(\mathbf{h})$ specifies the set of constraints on $\mathbf{h}$ which must be satisfied to form a halo of mass m. Then

$$n(m|\Delta_e) = \int \mathrm{d}\mathbf{h}\, p(\mathbf{h}|\Delta_e)\, C_m(\mathbf{h}) \tag{4.15}$$

and

$$\langle \Delta_0 | \Delta_e, m \rangle = \frac{\int \mathrm{d}\mathbf{h}\, p(\mathbf{h}, \Delta_e)\, C_m(\mathbf{h})\, \langle \Delta_0 | \Delta_e, \mathbf{h} \rangle}{\int \mathrm{d}\mathbf{h}\, p(\mathbf{h}, \Delta_e)\, C_m(\mathbf{h})}. \tag{4.16}$$

4.1.5 Reconstructing the dependence on mass and environment

Fixing m and marginalizing over all Δ_e yields

$$\begin{aligned}
&\frac{\int \mathrm{d}\Delta_e \int \mathrm{d}\mathbf{h}\, p(\mathbf{h}, \Delta_e)\, C_m(\mathbf{h})\, \langle \Delta_0 | \Delta_e, \mathbf{h} \rangle}{\int \mathrm{d}\Delta_e \int \mathrm{d}\mathbf{h}\, p(\mathbf{h}, \Delta_e)\, C_m(\mathbf{h})} \\
&= \frac{\int \mathrm{d}\mathbf{h}\, p(\mathbf{h})\, C_m(\mathbf{h})\, \langle \Delta_0 | \mathbf{h} \rangle}{\int \mathrm{d}\mathbf{h}\, p(\mathbf{h})\, C_m(\mathbf{h}) \int \mathrm{d}\Delta_e\, p(\Delta_e|\mathbf{h})} \\
&\quad + \frac{\int \mathrm{d}\mathbf{h}\, p(\mathbf{h})\, C_m(\mathbf{h}) \int \mathrm{d}\Delta_e\, p(\Delta_e|\mathbf{h})\, \langle \Delta_0 | \Delta_{e|\mathbf{h}} \rangle}{n(m)} \\
&= \frac{\int \mathrm{d}\mathbf{h}\, p(\mathbf{h})\, C_m(\mathbf{h})\, \langle \Delta_0 | \mathbf{h} \rangle}{n(m)}.
\end{aligned} \tag{4.17}$$

The ratio of the final expression to $\langle \Delta_0 \Delta_h \rangle$ is what is usually meant by $b_h(m)$.

On the other hand, marginalizing over all halo masses at fixed environment yields

$$\begin{aligned}
&\frac{\int \mathrm{d}m \int \mathrm{d}\mathbf{h}\, p(\mathbf{h}|\Delta_e)\, C_m(\mathbf{h})\, \langle \Delta_0 | \Delta_e, \mathbf{h} \rangle}{\int \mathrm{d}m \int \mathrm{d}\mathbf{h}\, p(\mathbf{h}|\Delta_e)\, C_m(\mathbf{h})} \\
&= \langle \Delta_0 | \Delta_e \rangle + \frac{\int \mathrm{d}m \int \mathrm{d}\mathbf{h}\, p(\mathbf{h}|\Delta_e)\, C_m(\mathbf{h})\, \langle \Delta_0 | \Delta_{\mathbf{h}|e} \rangle}{\int \mathrm{d}m\, n(m|\Delta_e)}.
\end{aligned} \tag{4.18}$$

If $\mathbf{h}$ involves Δ_h (where, typically $R_h^3 \propto m$) and its derivatives, then, as we have already discussed, we expect the expression above to be dominated by the first term on the right hand side, especially when $R_h \ll R_e \ll R_0$.

Pujol et al. (2017) show that if one attempts to reconstruct how bias depends on Δ_e using

$$\frac{\int \mathrm{d}m \int \mathrm{d}\mathbf{h}\, p(\mathbf{h}|\Delta_e)\, C_m(\mathbf{h})\, \langle \Delta_0 | \mathbf{h} \rangle}{\int \mathrm{d}m\, n(m|\Delta_e)}$$

(their equation 5) then one gets the wrong answer: almost no predicted dependence of the bias on Δ_e when the measurements show a strong trend. Comparison with our equation (4.18) shows why; by assuming that halo bias depends only on halo mass, their expression misses the contribution which leads to the first term on the right hand side of our expression – the term which dominates the answer when $R_h \ll R_e \ll R_0$.

On the other hand, Pujol et al. (2017) found that

$$\frac{\int \mathrm{d}\Delta_e \int \mathrm{d}\mathbf{h}\, p(\mathbf{h}, \Delta_e)\, C_m(\mathbf{h})\, \langle \Delta_0 | \Delta_e \rangle}{\int \mathrm{d}\Delta_e\, n(\Delta_e|m)}$$

(their equation 6) was able to reconstruct the mass dependence of bias rather well. Our analysis shows why this works, even though it too is, formally, incorrect. (The correct expression is our equation 4.17) Namely, the expression above can be written as

$$\frac{\int \mathrm{d}\mathbf{h}\, p(\mathbf{h})\, C_m(\mathbf{h}) \int \mathrm{d}\Delta_e\, p(\Delta_e|\mathbf{h})\, \langle\Delta_0|\Delta_e\rangle}{n(m)} = \frac{\int \mathrm{d}\mathbf{h}\, p(\mathbf{h})\, C_m(\mathbf{h})\, \langle\Delta_0\Delta_e\rangle\langle\Delta_e|\mathbf{h}\rangle/S_e}{n(m)}, \tag{4.19}$$

and our discussion of equation (4.7) showed that we expect

$$\langle\Delta_0\Delta_e\rangle\langle\Delta_e|\mathbf{h}\rangle/S_e \approx \langle\Delta_0|\mathbf{h}\rangle. \tag{4.20}$$

If this approximation were an equality, then their expression would reduce to the correct one, our equation (4.17). That it is only an approximation is why Pujol et al. (2017) only found good, but not perfect agreement with the actual mass dependence of bias, $b_h(m)$.

4.2 Evolution

The analysis of the previous section was for statistics in the initial conditions, sometimes called Lagrangian space. Since the analysis in Pujol et al. (2017) was for halos and environments defined in the evolved Eulerian space, our assertions in Section 4.1 are not completely justified until we have shown that they survive nonlinear evolution.

4.2.1 Excursion set approach: Analytic

We use the excursion set approach of Sheth (1998) to model statistics in the evolved Eulerian space. This approach makes use of the spherical evolution mapping between $\delta_{\rm V}$, the Eulerian density on scale V, and $\Delta_{\rm M}$, the Lagrangian density on scale M:

$$1 + \delta_{\rm V} \equiv M/\bar{\rho}V = (1 - \Delta_{\rm M}/\delta_c)^{-\delta_c}, \tag{4.21}$$

where V is the Eulerian volume, M is the mass in it, and $\delta_c \approx 1.686$ (although $\delta_c = 21/13$ reproduces the monopole of second order perturbation theory). In what follows, we will also make use of the fact that

$$\frac{\Delta_{\rm M}}{\delta_c} = 1 - \left(\frac{\bar{\rho}V}{M}\right)^{1/\delta_c} = 1 - (1 + \delta_{\rm V})^{-1/\delta_c}, \tag{4.22}$$

which follows from rearranging equation (4.21).

The gist of the argument is that Eulerian statistics on scale V are related to Lagrangian statistics on scale M. While this idea can be traced back to Bernardeau (1994), the analysis in Sheth (1998) allows one to work down to substantially smaller V. Lam & Sheth (2008) show that it provides a rather good model of what we call the probability distribution of the Eulerian environment here. Our goal is to show that this approach also provides a simple description of the joint distribution of halos and their environment – i.e. of Eulerian bias – a point which was made in Sheth (1998), but has not been followed-up since. This turns out to be straightforward, particularly because of recent advances in our understanding of the excursion set approach (Musso & Sheth, 2012).

In what follows, δ and Δ always denote Eulerian and Lagrangian overdensities, and their subscripts always denote the corresponding Eulerian or Lagrangian smoothing scale. E.g., if δ_0 is the Eulerian density on scale V_0, then Δ_0 is the Lagrangian density on scale $M_0/\bar{\rho} = V_0\,(1+\delta_0)$, and δ_0 and Δ_0 are related by equation (4.22).

Our goal is to estimate the mean Eulerian density on scale V_0 given that the Eulerian cell is centered on a region with Eulerian density δ_e on scale V_e which itself is centered on a halo of mass m. The Lagrangian version of this quantity is equation (4.16). It becomes

$$\langle \delta_0|\delta_e, m\rangle = \frac{\int \mathrm{d}\mathbf{h}\; p(\mathbf{h},\Delta_e)\, C_m(\mathbf{h})\, \langle \delta_0|\Delta_e,\mathbf{h}\rangle}{\int \mathrm{d}\mathbf{h}\; p(\mathbf{h},\Delta_e)\, C_m(\mathbf{h})}, \tag{4.23}$$

where we have used the fact that the m and δ_e constraints correspond to simple constraints in Lagrangian space. The main problem is to estimate $\langle \delta_0|\Delta_e,\mathbf{h}\rangle$.

On large Eulerian scales V_0 we expect $\delta_0 \ll 1$, and hence $\Delta_0 \approx \delta_0$ almost surely. In this limit, we expect to be able to use the Gaussian expression (equation 4.7):

$$\langle \delta_0|\delta_e, m\rangle \approx \langle \Delta_0|\Delta_e\rangle + \langle \Delta_0|\Delta_{h|e}\rangle \tag{4.24}$$

where $\langle \Delta_0|\Delta_e\rangle = \Delta_e\,\langle \Delta_0\Delta_e\rangle/\langle \Delta_e^2\rangle$ dominates. This would make

$$b_{\rm e}^{\rm E} = \frac{\Delta_e}{\langle \Delta_e^2\rangle} = \frac{\delta_c[1-(1+\delta_e)^{-1/\delta_c}]}{S\,[\bar{\rho}V_e(1+\delta_e)]}, \tag{4.25}$$

where S is the the Lagrangian variance on the mass scale $\bar{\rho}V_e(1+\delta_e)$. Equation (4.25) is the expression in Abbas & Sheth (2007). Comparison with equation (4.5) shows explicitly that, in this limit, the Eulerian bias is like the Lagrangian one provided that one correctly rescales the density *and* volume. Figure 3 of Pujol et al. (2017) shows that this simple expression works remarkably well over a wide range of scales.

Before moving on, we note that this expression has been rediscovered by Uhlemann et al. (2017) who appear to be unaware of earlier work. Moreover,

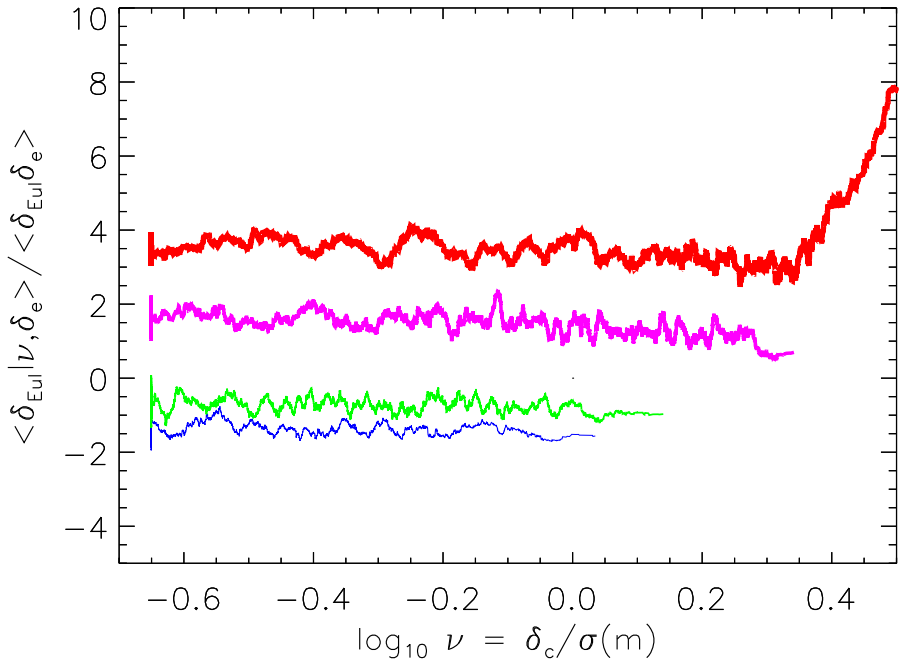

Figure 4.1: The Eulerian bias of halos surrounded by large overdensities is larger; however, at fixed overdensity, bias is the same for all except the most massive halos. The thickness of line is proportional to the overdensity value, with the thickest line corresponding to the densest field. Red and magenta are for halos in the densest 10% and the next densest 20% of the cells in the evolved Eulerian field; blue and green show the bias of halos in the least dense 10% and the next emptiest 20%. The apparent upper limit in ν, which increases with density, is because massive halos are not present in the least dense cells.

as we have spelled out in more detail here, the excursion set approach of Sheth (1998) shows why, even though equation (4.25) is quite accurate, it is just an approximation. That is to say, it shows clearly how to go beyond rescaled Kaiser-bias. For example, the top panel of Figure 6 in Pujol et al. (2017) shows the comoving number density of halos in cells of specified overdensity δ_e. They do not remark on it, but this quantity has long been known to be well-approximated by equation (4.15), with Δ_e given by δ_c times the rhs of equation (4.22) when $\delta_e = \delta_V$ in the rhs of equation (4.22) (Mo & White, 1996; Sheth & Tormen, 2002). This is a limit which our approach is designed to reproduce (Sheth, 1998).

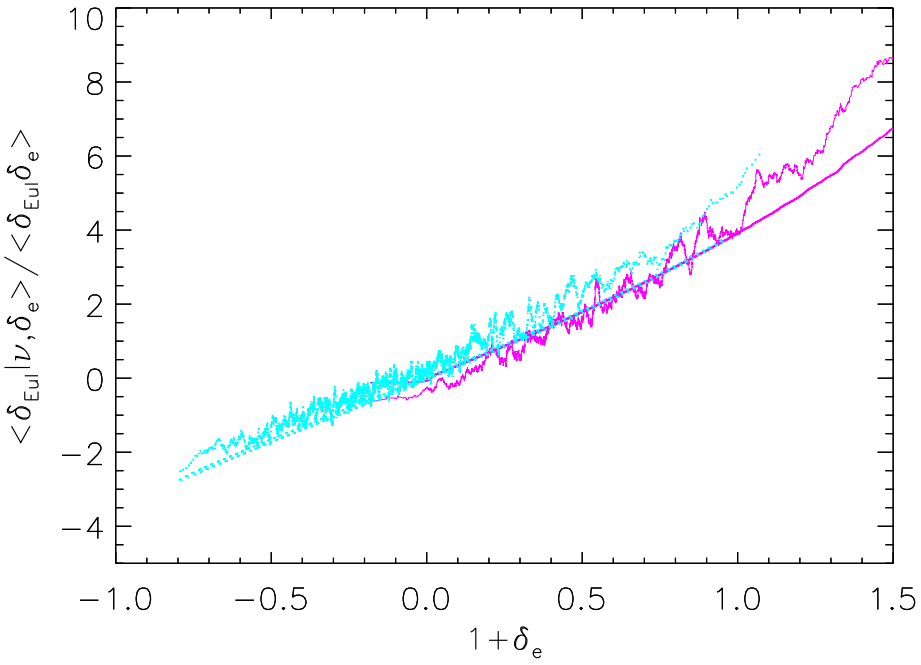

Figure 4.2: Denser Eulerian cells are more biased, but this bias is independent of the mass of the halo at the cell center. Cyan dotted and magenta solid show results for cells centered on the 10% lowest and highest mass halos. Thick smooth magenta and thick dotted cyan curves show $b_e^{\rm E}$ of equation (4.25).

4.2.2 Excursion set approach: Monte-Carlo

We have checked the analysis above explicitly in Monte-Carlo realizations of this process. Namely, we generated 10^5 random walks, each having a correlation structure appropriate for top-hat smoothing of a Gaussian field having $P(k) \propto k^{-2}$. We used the algorithm described in Musso & Sheth (2014) to do this. For each walk, we stored the mass scale on which it first crossed a 'constant barrier' of height δ_c, and the mass scale on which it crossed the 'moving barrier' of equation (4.22), for a range of choices of Eulerian V. First crossing of δ_c is a simple proxy for a halo; by storing first crossings for a range of V, we can map out the Eulerian profile around each 'halo' (see Sheth 1998; indeed, viewed this way, a halo is just the special case in which $V = 0$). In addition, we stored the height of the walk on a number of mass scales, which we use to reconstruct Lagrangian profiles of halos or of Eulerian cells.

Red, magenta, green and blue curves in Figure 4.1 show the Eulerian bias

of halos which are centered on patches having Eulerian densities $\langle 1 + \delta_V \rangle = (7.5, 2.3, 0.5, 0.3)$. The scale V is such that, when smoothed on scale containing mass $M = \bar{\rho}V$, the rms linear theory overdensity had variance $\langle \Delta_V^2 \rangle = 0.5^2$. (Therefore, a halo of mass $\bar{\rho}V$ would have $\nu = \delta_c/\sigma = 42/13$. This is why the curves for underdense regions do not extend to larger ν.) Clearly, the Eulerian bias is larger for the halos centered on denser cells; however, except for the densest cells, the bias is the same for all halo masses. I.e., the bias is determined by the environment, and not by halo mass.

Figure 4.2 shows another way of presenting this trend: cyan and magenta curves show how the bias depends on environment for the least and most massive halos. Clearly, the bias is the same strong function of environment whatever the mass of the halo at the center. (For the moment, we are ignoring the slight tendency for the cells centered on the most massive halos to have slightly smaller bias factors.) The smooth curve shows equation (4.25); it provides a good description of the measurements. This shows explicitly that the first term in equation (4.24) really does capture most of the environmental effect. The second term in equation (4.24) must account for the small trend with mass which remains, but note that this is much smaller than the overall trend with environment.

The trends in Figures 4.1 and 4.2 are remarkably similar to those shown in Figure 4 of Pujol et al. (2017). Even the slight tendency for environments centered on massive halos to be slightly less biased (Figure 4.2) is similar. This suggests that our Monte Carlos realizations have captured the essence of the effect.

To show that we really do understand the origin of this effect, on small scales as well, Figure 4.3 shows the initial Lagrangian density profiles around the patches which evolve into the densest and least dense cells. Symbols with error bars show the mean and the rms around the mean – errors on the mean are smaller than the symbols. Curves show the Lagrangian-space cross correlation – essentially equation 4.7; there are no free parameters in this comparison. The agreement justifies the assertions we made in Section 4.1.5. Namely, accounting for the joint distribution of mass and environment is straightforward. Doing so shows that, just as in Lagrangian space, the Eulerian bias is also determined primarily by the larger scale environment, and much less so by halo mass. Therefore, analyses which ignore the environmental effect will lead to incorrect conclusions about the nature of halo bias.

4.3 Discussion and conclusions

We discussed how the large scale bias of halos depends on both halo mass and environment, in Lagrangian (Section 4.1) and Eulerian (Section 4.2) space. We showed that, at fixed environment, the dependence of large scale bias on halo mass

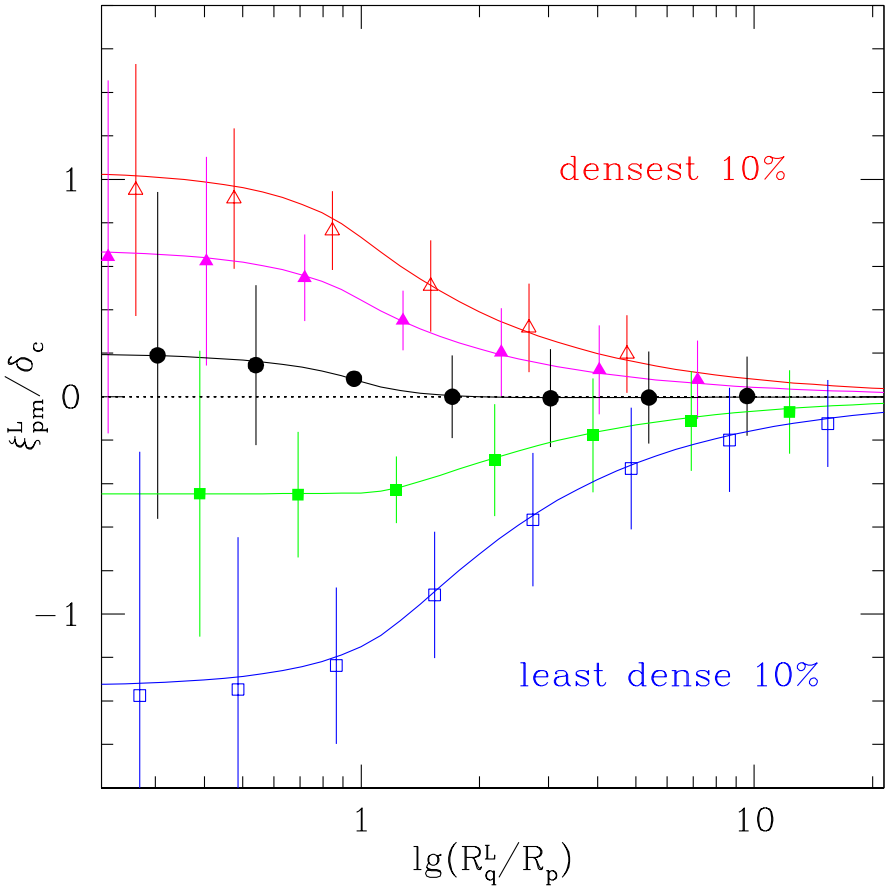

Figure 4.3: Initial Lagrangian density profiles around patches which become Eulerian cells with the specified density: red and magenta are for the densest 10% and the next densest 20% of the cells in the evolved Eulerian field; blue and green show the least dense 10% and the next emptiest 20%. Symbols with error bars show the mean and the rms around the mean – errors on the mean are smaller than the symbols. Curves show the Lagrangian-space cross correlation; there are no free parameters in this comparison.

should be weak (Figure 4.1). Indeed, if one defines halos and environment using a filter which is sharp in k-space (Bond et al., 1991), and one conditions on large scale environment, then large-scale bias is predicted to be *completely* independent of halo mass (see discussion in Section 4.1.2). Our calculation quantifies the small residual effect which comes from the fact that correlations between scales are more complicated than for sharp-k smoothing.

This has an interesting implication. Following Sheth & Tormen (2004), there have been many studies of the dependence of bias on other parameters, if halo mass is held fixed. These are usually called 'Assembly Bias' studies, even though the additional parameters may not be explicitly related to halo assembly. The underlying origin of all these signals is nontrivial correlations between scales. Our analysis shows that if bias at fixed environment does show some dependence (presumably weak!) on halo mass, then one has detected the effect of nontrivial correlations between scales. In this sense, one has detected 'Assembly Bias' coming from the other way round from what is currently fashionable. To see this explicitly, suppose we order scales as

$$R_{\rm bias} \geq R_{\rm env} \geq R_{\rm halo} \geq R_{1/2}$$

where $R_{1/2}$ (for 'half-mass') is a crude proxy for halo assembly. The usual studies fix $R_{\rm halo}$ and look for additional correlation between the more widely separated scales $R_{\rm bias}$ and $R_{1/2}$. But the ranking of scales shows that one could have fixed $R_{\rm env}$ and looked for additional correlation between $R_{\rm bias}$ and $R_{\rm halo}$ (or $R_{1/2}$). This is the sense in which looking for mass dependence at fixed environment is the same as assembly bias.

The analysis of the previous section is particularly relevant to the question of whether or not galaxy properties depend on quantities other than halo mass. The main text shows why, when the environment is constrained, then halo bias is a function of both halo mass and environment. However, this does *not* mean that the HOD of how galaxies populate halos must also depend on both (it may, but it need not). Indeed, Abbas & Sheth (2007) showed that mock galaxy catalogs, in which mass is the only variable which determines how galaxies populate halos, automatically exhibit a number of environmental trends that are seen in the data. That is to say, they showed that the data they examined do *not* require any additional galaxy-environment effect: the halo-environment correlation which comes for free, and which we have spelled out in some detail in this chapter, is sufficient to explain the galaxy-environment correlations.

While this may be true for observable such as luminosity, which are expected to be monotonically related to halo mass, the same may not be true for colors, for which the correlation with halo mass is not as simple. A simple model for galaxy colors, in which galaxy-environment correlations are inherited from the

halo-environment correlations, is able to provide a reasonable description of the bright SDSS galaxies considered by Abbas & Sheth (Skibba & Sheth, 2009). However, it is too simplistic to account for all observed correlations (see Pahwa & Paranjape, 2017, for the current state of the art), and studies at the faint end have yet to be done. Pujol et al. (2017) show that, in the semi-analytic galaxy formation model they considered, galaxy color appears to correlate more with density than halo mass, and that density appears to be more important than halo mass for faint red central galaxies. The importance of environment over halo mass appears at lower luminosities than Abbas & Sheth considered in the SDSS. At these lower luminosities, the scatter between halo mass and luminosity becomes larger, so it will be interesting to see if the color-dependent trends in Pujol et al. (2017)'s Figure 8 are reproduced in data. With such studies in mind, we express their results in our formalism in Appendix A.2.

An interesting extension of our work would be to study what happens if the environment of a halo is defined using a measure which does not correlate with the density. E.g., Paranjape, Hahn & Sheth (2017) use a measure which is built from the tidal shear. They show that, at fixed mass, halo bias correlates strongly with the morphology of the environment (e.g., 'filamentary' versus 'isotropic'), *and* that bias is also a strong function of mass when the environment is fixed. This 'assembly bias' effect appears to be richer than the one with density which we studied here. Again, however, galaxies will inherit the environmental correlations of their host halos, so care must be taken to isolate correlations with environment which are over and above those which come 'for free' from the host halo-environment correlation.

Finally, the careful reader will have noticed that our least dense cells have $1 + \delta_e \sim 0.2$ (e.g. Figure 4.1); such cells would be classified as 'voids' (Sheth & van de Weygaert, 2004). These 'voids' have Eulerian bias factors which are less than zero (Figure 4.1), and the associated Lagrangian profiles of these cells are indeed rather underdense, especially on small scales (Figure 4.3). Clearly, then, the excursion set approach allows us to model the evolution of void profiles; this is done in Massara & Sheth (2017, in preparation). In addition, study of the redshift-space clustering in the $b = 0$ subsample (Figures A.2 and A.3 suggest this is true of the 30% underdense sample) may allow simple constraints on the growth rate $f = \mathrm{d}\ln D/\mathrm{d}\ln a$, from a comparison of the (projected) real and redshift space clustering signals. Furthermore, subsamples selected using our methodology have a rather wide range of bias factors, making them well-suited for multi-tracer constraints on redshift space distortions and primordial non-Gaussianity (McDonald & Seljak, 2009), and for measuring the gravitational redshift effect from large scale structures(Zhu et al., 2017).

Chapter 5

Environmental Dependence of Halo Dynamical Properties and Accretion History

The spatial clustering of halos of a given mass depends significantly on various halo properties. Gao, Springel & White (2005) and Li, Mo & Gao (2008) found that old low-mass halos are more strongly clustered than their younger counterparts. Halo clustering also depends on halo structural properties, such as halo concentration and substructure abundance (Wechsler et al., 2006; Jing, Suto & Mo, 2007), and on dynamical properties, such as halo angular momentum (Bett et al., 2007; Gao & White, 2007), and internal velocity structure (Faltenbacher & White, 2010). All these dependencies, usually referred to as assembly bias, indicate the importance of environmental effects on halo formation and evolution.

In the CDM paradigm of structure formation, dark matter halos form through the accretion (merger) of smaller halos, and halo properties are expected to be determined by their formation histories. The most simple proxy for the formation history is the formation redshift. However, the formation histories of individual halos are complex and cannot be described completely by these simple characteristic formation times. Indeed, information about how small halos to be accreted (i.e. infall halos) are distributed in phase space is totally lost in these characteristic formation times, and yet may be pivotal in the understanding of the structural and dynamical properties of the halos that grow through such accretion process. Previous studies have found that infall halos on average have higher radial than tangential velocities (Tormen, 1997; Vitvitska et al., 2002; Benson, 2005; Wang et al., 2005; Wetzel, 2011; Jiang et al., 2014). Such anisotropic orbits of accretion may affect the internal velocity structure of the descendant halos that form through such accretion. Indeed, dark matter halos in N-body simulations are found to be dominated by radial orbits in their internal velocity distributions, at least in the

outer parts (Colín, Klypin & Kravtsov, 2000; Rasia, Tormen & Moscardini, 2004; Ludlow et al., 2011; Sparre & Hansen, 2012). Clearly, it is important to understand and quantify such links between halo internal properties and their accretion processes. Furthermore, since the phase space distribution of halos to be accreted into a host halo is expected to be closely linked to the large-scale environment within which the host halo resides, such information is also crucial in order to understand the environmental effects on halo structure and dynamics.

In this chapter, we study in detail how small halos are accreted by their hosts, how the properties of the host halos are determined by the accretion process, and how the accretion processes, through which the intrinsic properties of halos are determined, are linked to the local environments of the halos. We pay particular attention to halo dynamical properties, such as velocity dispersion, angular momenta and velocity ellipsoid. The structure of the chapter is organized as follows. In Section 5.1, we describe the simulations we use, and our methods for halo identification, merger tree construction and tidal field estimation. In Section 5.2, we investigate the orbital distributions of infall halos and their dependencies on the large scale tidal field. Section 5.3 examines how halo dynamical properties depend on environments, and how the dependence can be understood in terms of the orbits of infall halos. Finally, in Section 5.4 we discuss and summarize our main results.

5.1 Numerical simulations and dark matter halos

5.1.1 Simulation and halo identification

In this study, we use two N-body cosmological simulations with the same settings carried out with Gadget-2 (Springel, 2005), so we could have better statistics. These simulations adopted a flat ΛCDM cosmological model, with $\Omega_{\Lambda,0} = 0.742$ for the cosmological constant, $\Omega_{\rm dm,0} = 0.214$ and $\Omega_{\rm b,0} = 0.044$ for CDM and baryons, respectively, $h = 0.72$ for the dimensionless value of the Hubble constant, $\sigma_8 = 0.8$ for the *rms* linear mass fluctuation in a sphere of radius $8\,h^{-1}$Mpc extrapolated to $z = 0$, and $n = 1$ for the slope of the primordial fluctuation spectrum. The CDM density field of each simulation is traced by 1024^3 particles, each with mass $m_{\rm p} \approx 5.3352 \times 10^8\,h^{-1}{\rm M}_\odot$, from $z = 72$ to $z = 0$ in a cubic box of a side length $200\,h^{-1}$Mpc. The gravitational force is softened isotropically on a co-moving length scale of $4\,h^{-1}$kpc (Plummer equivalent). Each simulation outputs 80 snapshots from $z = 17$ to $z = 0$, equally spaced in the logarithm of the expansion factor.

Dark matter halos are identified using the standard FOF algorithm (Davis et al., 1985) with a link length that is 0.2 times the mean inter-particle separation. We only consider halos that contain at least 20 particles, and the mass of a halo is the sum of the masses of all particles in the halo. It is known that some FOF halos, in

particular small ones containing small number of particles, may be dominated by 'fuzzy' particles that are not gravitationally bound. We use SUBFIND algorithm developed by Springel et al. (2001) to identify subhalos that are gravitationally bound. If the most massive bound structure contains less than half of the total mass of the FOF halo, this FOF halo is considered to be dominated by 'fuzzy' particles and is excluded from our analysis.

5.1.2 Merger trees and halos to be accreted

Here we give a brief description of the construction of halo merger trees and the identification of halos to be accreted into a host halo. We identify dark matter halos using the method described above in each of the snapshots and cross link halo particles in adjacent snapshots. If more than half of the particles in a halo (denoted as halo 'A') end up in a halo in the next snapshot (denoted as halo 'B'), we call halo 'A' a progenitor of halo 'B', and halo 'B' the descendant of 'A'. This definition ensures that a halo can have one or more progenitors but can only have one descendant. The uniqueness of the descendant allows us to build up a unique merger tree for every halo at present day. For any halo identified at a given time, its most massive progenitor in the last snapshot is referred to as its main progenitor. Tracing the main progenitors back in time gives the main trunk of the merger tree of a halo identified at $z = 0$.

For a given halo at present day, we select all of its progenitors that are not parts of the main trunk but whose first generation descendants are main trunk halos. These halos are referred to as infall halos. The main progenitors, into which these infall halos are falling, are called host halos. The redshift at which an infall halo is identified is referred to as the infall redshift, $z_{\rm inf}$, of the infall halo. Infall halos are therefore merging with their hosts at a redshift around $z_{\rm inf}$. Some infall halos may have been sub-halos of their hosts at $z > z_{\rm inf}$ but have later moved outside of their hosts and are now falling back onto the hosts. The orbits of these halos may have been severely altered by interactions with the internal structures of the hosts, and so are not suitable for our investigation of large-scale environmental effects. Unfortunately, such halos cannot be directly identified because our merger trees constructed by using FOF halos cannot trace the evolution of subhalos within host halos. As an approximation, we adopt the method developed in Wang, Mo & Jing (2009) to identify these halos. For an infall halo 'A', we trace its main progenitor back in time until its earliest main progenitor 'B' is found in a snapshot, say n. We then check whether or not more than half of the particles of halo 'B' belong to the main progenitor of the host halo of 'A' at an earlier snapshot $n - 1$. If yes, then 'A' is considered to have been ejected by the host at an early time, and is excluded from our analysis. Thus, we only consider halos that are in their first infall.

A tiny fraction of infall halos are not contained in their host halos at $z = 0$

(Ludlow et al., 2009; Wang, Mo & Jing, 2009; Bahé et al., 2012; Li et al., 2013). They are either ejected by their hosts after being accreted or flybys fortuitously linked to their massive neighbors by the FOF algorithm. This population may have important implications for understanding the existence of quenched galaxies near clusters and groups in the local Universe (Wang et al., 2009; Li et al., 2013; Wetzel et al., 2014). To study the environmental dependence of halo assembly in detail, we identify this population in the following way. If more than half of the particles in an infall halo are not contained in its host (or descendant) at $z = 0$, the infall halo is thought to have finally escaped. This population will be referred to as ejected halos. Other infall halos, which stay as subhalos within their hosts at $z = 0$, are referred to as the staying population.

Limited by finite mass resolution and small number statistics, here we focus on the merger histories of host halos in two mass ranges, $10^{12.5} \geq M_0 \geq 10^{12}\,h^{-1}\mathrm{M}_\odot$ (MW size) and $M_0 \geq 10^{13}\,h^{-1}\mathrm{M}_\odot$ (massive group size), where M_0 is the halo mass at $z = 0$. The total numbers of host halos in the two mass ranges are listed in Table 5.1. For the host halos in the lower mass bin, infall halos with masses $M_{\rm inf}$ given by $M_{\rm inf}/M_0 \geq 20m_{\rm p}/10^{12} \simeq 0.01$ are taken into account. These infall halos are divided into two samples. The first sample, denoted by M12(S), consists of only staying infall halos. The second, M12(E), contains infall halos that eventually are ejected by their hosts. The infall halos of the massive hosts are divided into four samples. The first, M13(S), consists of all infall halos with $M_{\rm inf}/M_0 \geq 0.01$ in the staying population. The mass threshold adopted here is the same as that for M12(S), and so one can investigate the dependence on host halo mass by comparing M12(S) and M13(S). The second, M13(S'), consists of infall halos with $0.01 > M_{\rm inf}/M_0 \geq 20m_{\rm p}/10^{13} \simeq 0.001$, again in the staying population. A comparison between M13(S) and M13(S') may help us to understand the dependence on the mass of infall halos. The third and fourth samples, M13(E) and M13(E'), contain infall halos of the ejected population, with masses in the same ranges as for M13(S) and M13(S'), respectively. The numbers of infall halos in all the six samples are listed in Table 5.1.

Figure 5.1 shows the distributions of $z_{\rm inf}$ for the six infall halo samples described above. M12(S) on average has higher $z_{\rm inf}$ than M13(S), as expected from the fact that smaller halos are, on average, older than more massive ones. Infall halos that stay as sub-halos are accreted over a wide range of redshift. In order to minimize possible dependence on redshift, we consider infall halos accreted in two relatively narrow redshift ranges, a low-redshift range $z_{\rm inf} \leq 0.4$ and a high redshift range, $0.75 \leq z_{\rm inf} \leq 1.25$. The numbers of halos in these two redshift bins for samples M12(S), M13(S) and M13(S') are also listed in Table 5.1. The distributions of the ejected halos are much narrower, with peaks at $z \sim 0.5$, and the majority of such halos have infall redshifts below $z = 1$. Because of this we do not split ejected halos further according to infall redshifts.

Table 5.1: Number of host halos and infall halos in the samples. M_0 is the mass of host halos at $z = 0$, in unit of $h^{-1}\mathrm{M}_\odot$, N_h is the number of host halos at $z = 0$. $N_{\rm inf}$ is the number of infall halos. Low $z_{\rm inf}$ indicates $z_{\rm inf} \leq 0.4$ and high $z_{\rm inf}$ indicates $0.75 \leq z_{\rm inf} \leq 1.25$.

$\log M_0$	≥ 13						12 - 12.5		
N_h	5793						37124		
Infall halo	M13(S')		M13(S)		M13(E')	M13(E)	M12(S)		M12(E)
$N_{\rm inf}$	214720		49503		37014	1718	330221		30818
$z_{\rm inf}$	low	high	low	high			low	high	
$N_{\rm inf}$	54088	38251	12135	9772			56767	55946	

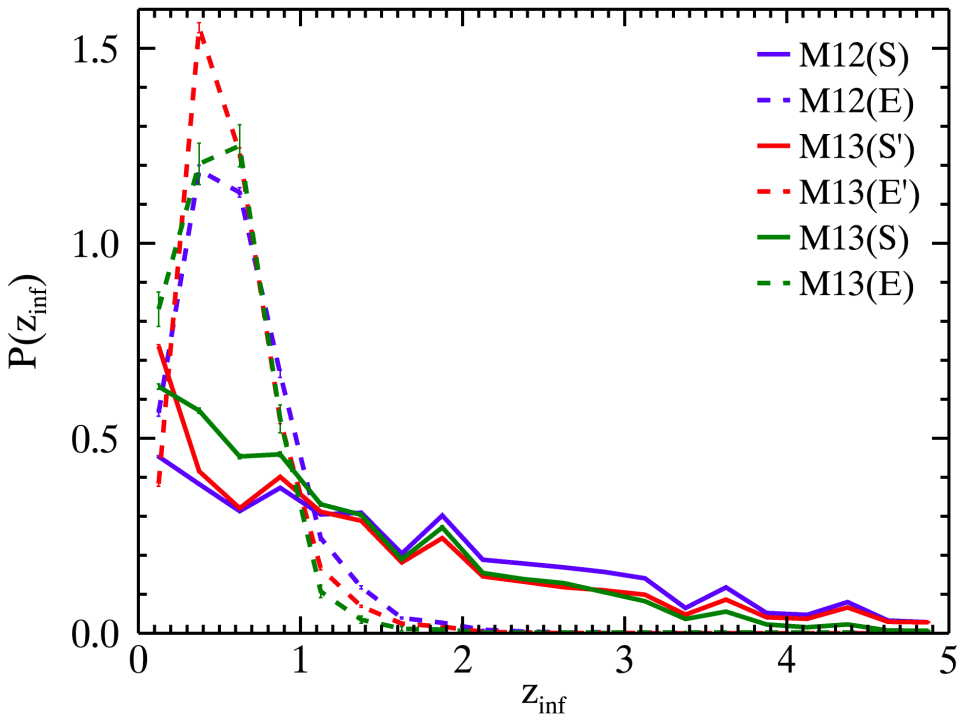

Figure 5.1: The probability distribution of infall redshift, $z_{\rm inf}$, for the six infall halo samples as indicated in the figure. See Section 5.1.2 for sample selections.

5.1.3 Large scale tidal field

A number of quantities can be used to characterize the large scale environment of dark matter halos, including halo bias parameter, local mass over-density, morphology of large scale structure (i.e. cluster, filament, sheet and void), velocity shear field and large scale tidal field (Mo & White, 1996; Gao, Springel & White, 2005; Maulbetsch et al., 2007; Hahn et al., 2007; Wang et al., 2011; Libeskind et al., 2013a; Libeskind, Hoffman & Gottlöber, 2014). In this work, we adopt the (external) tidal field at the location of a halo to represent the large-scale environment in which the halo resides. The (external) tidal field is estimated by summing up the tidal forces exerting on the halo by all other halos above a mass threshold, $M_{\rm th} = 10^{12}\,h^{-1}{\rm M}_{\odot}$, and is normalized by the self-gravity of the halo in question (Wang et al., 2011). The normalized tidal force on the surface of a given halo, in direction $\boldsymbol{t}$ is

$$\begin{aligned} f_i(\boldsymbol{t}) &= \frac{\sum_{i=1}^{N} \frac{GM_i}{r_i^3} R_h[1/2 + 3/2\cos(2\theta_i)]}{GM_h/R_h^2} \\ &= \sum_{i=1}^{N} \frac{R_i^3}{2r_i^3}(1 + 3\cos 2\theta_i) \end{aligned} \tag{5.1}$$

where M_h and R_h are the mass and radius of the halo in question, M_i and R_i are the masses and radii of all other halos exerting the tidal force, r_i is the distance from the halo "h" to halo "i", and θ_i is the angle between $\boldsymbol{t}$ and $\boldsymbol{r}_i$. The second equation stands for the fact that $M_h \propto R_h^3$ and $M_i \propto R_i^3$. $\boldsymbol{t}_1$ and $\boldsymbol{t}_3$ are defined as the direction where the tidal force reach the maxima and minima. They are the eigenvectors of the halo tidal tensor, and perpendicular to each other. The third eigenvector $\boldsymbol{t}_2$ is perpendicular to both $\boldsymbol{t}_1$ and $\boldsymbol{t}_3$. The tidal forces along $\boldsymbol{t}_1$, $\boldsymbol{t}_2$, and $\boldsymbol{t}_3$ are denoted as t_1, t_2, and t_3(by definition, $t_1 > t_2 > t_3$). The three eigenvalues satisfy $t_1 + t_2 + t_3 \equiv 0$, so t_1 is always positive and t_3 is always negative. Thus, the large scale tidal field stretches the material along $\boldsymbol{t}_1$ but compresses it along $\boldsymbol{t}_3$. In this work, we use t_1 as an indicator of the local tidal field strength.

The other method for calculating the tidal field, often adopted in the literature (e.g. Hahn et al., 2007; Zhang et al., 2009), directly makes use of the mass density field to get the *mass tidal field*. As shown in Wang et al. (2011), $\boldsymbol{t}_1$, $\boldsymbol{t}_2$ and $\boldsymbol{t}_3$ defined above are tightly aligned with the corresponding eigenvectors of the mass tidal field. Different from the mass tidal field, the tidal field defined above does not include the contribution of the self-gravity of the halo, and therefore is more closely related to the large-scale environment. Moreover, two halos that reside in a similar environment may suffer very differently from the local environment. For example, a 'hot' environment for a small halo can be quite 'cold' for a massive halo. To take into account this halo mass-dependent effect, our tidal field is normalized

by the self-gravity of the halo, so that one can compare the environmental effects for halos of different masses. More details about the tidal field defined here and its correlations with other environmental quantities can be found in the appendix of Wang et al. (2011).

We consider halos accreted at different redshifts. The environmental indicator can be chosen to be either the tidal field within which the $z = 0$ descendant halo resides or the tidal field when the accretion process occurs. In this work, we use the tidal field at $z = 0$ as an environmental indicator. There are two primary reasons for this choice. First, our eventual goal is to study similar effects in observational data (see Section 5.4). As shown in Yang et al. (2007), galaxy groups properly selected from large redshift surveys of galaxies can be used to represent the halo population. Dark matter halos are biased tracers of the underlying density field and can be used to estimate the large scale tidal field (Wang et al., 2012). Currently, such a galaxy group catalog is only available at low redshift. Second, one of the purposes of this work is to use the environmental dependence of halo accretion to interpret the environmental dependence of dynamical properties of halos at $z = 0$ (Section 5.3). The local tidal field within which these halos reside provides one such environmental indicator that can be estimated from observation.

One interesting question is how the tidal field around a halo evolves with redshifts. To answer this question, we analyze the alignments and correlations of the external tidal field around a $z = 0$ halo with those around its main progenitors at $z = 0.4$ and $z = 1.0$. Note that the external tidal field at a high redshift is also calculated without including the contribution of surrounding halos that will end up in the final halo. The results for the alignments and the correlations of t_1 are shown in Figure 5.2 and 5.3, respectively. The reason for choosing these two particular redshifts is that our following analyses focus on infall halos in the two redshift ranges, $z_{\rm inf} \leq 0.4$ and $0.75 \leq z_{\rm inf} \leq 1.25$. Clearly, the eigenvectors of the tidal fields at both $z = 0.4$ and $z = 1.0$ are strongly aligned with the corresponding vectors at $z = 0$. The alignments between $z = 0.4$ and $z = 0$ are stronger than those between $z = 1.0$ and $z = 0$, and the dependence on halo mass is rather weak. For both halo mass ranges, the tidal field strength at $z = 0.4$ is tightly correlated with that at $z = 0$, and the correlation becomes weaker for $z = 1.0$. Overall, the tidal field at $z = 0$ can be used as a proxy of the tidal field at higher redshift, at least to $z \sim 1$, and particularly for the orientation of the tidal field.

5.2 Environmental dependence of halo accretion

In this section, we investigate the environmental dependence of halo accretion from three different aspects. We emphasize again that we use the $z = 0$ tidal field as our environmental indicator. We first study the mass function of infall halos residing

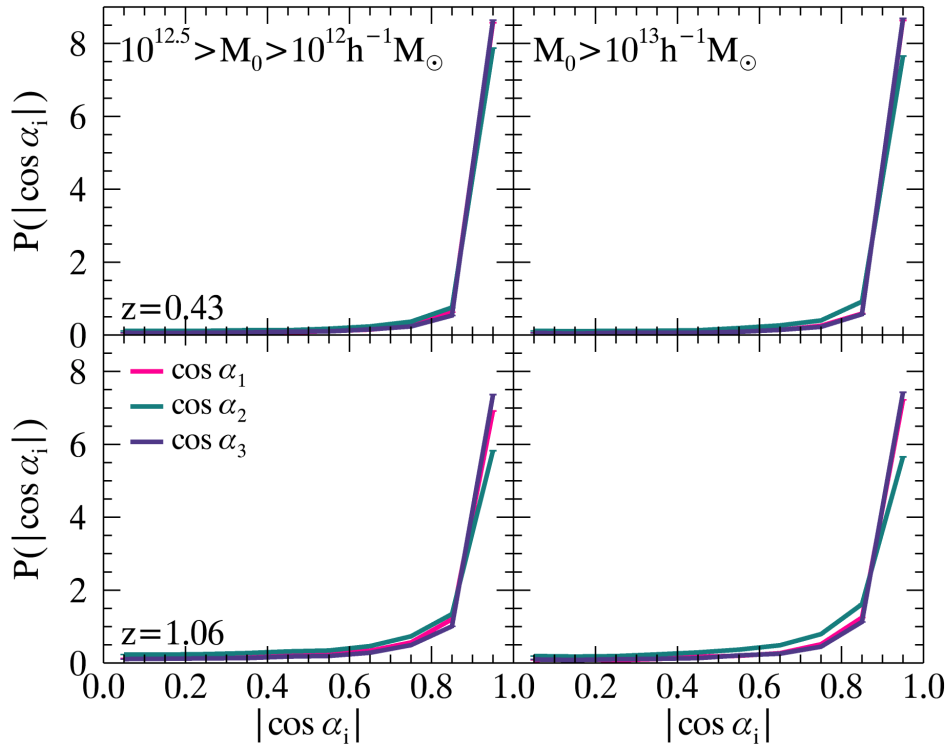

Figure 5.2: The probability distributions of $|\cos\alpha_i|$, where α_i is the angle between the eigenvectors $\boldsymbol{t}_i(i = 1, 2, 3)$ of the tidal field around a $z = 0$ halo and the corresponding eigenvectors around its main progenitors at $z = 0.4$ (upper panels) and $z = 1.0$ (lower panels). The right and left panels show the results for MW sized and massive group sized halos, respectively.

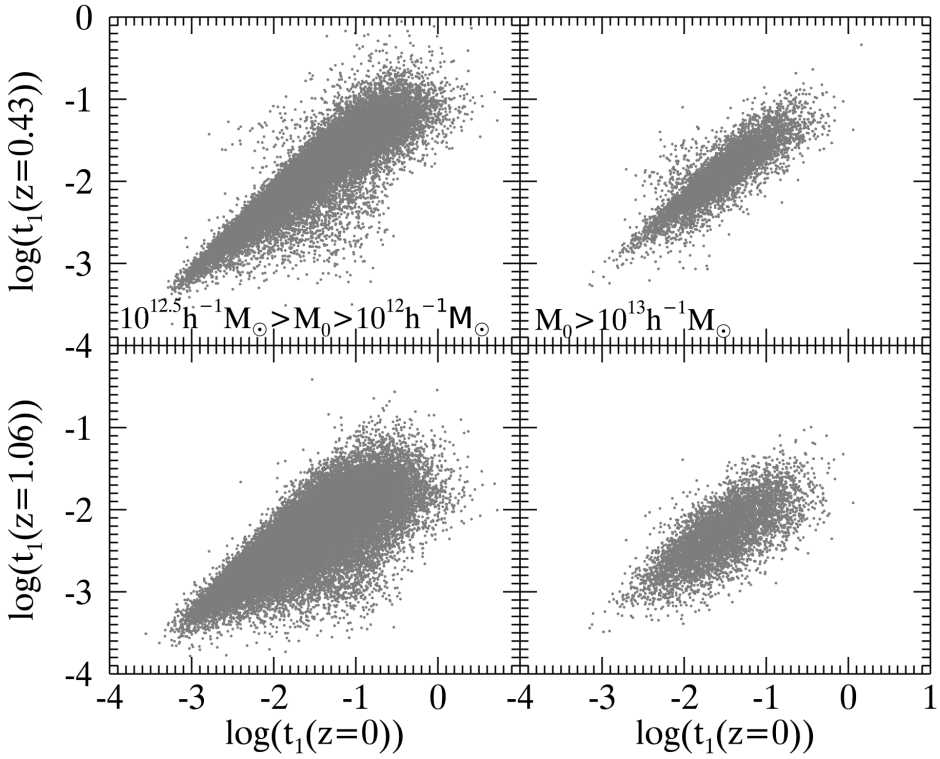

Figure 5.3: The comparison between the tidal field strength (t_1) around a $z = 0$ halo and that around its main progenitors at $z = 0.4$ (upper panels) and $z = 1.0$ (lower panels). The right and left panels show the results for MW sized and massive group sized halos, respectively.

in different environments (Subsection 5.2.1), and then investigate the correlations between the tidal field and the orbital properties of infall halos (Subsection 5.2.2). Finally, in Subsection 5.2.3, we examine the alignment between the position and velocity vectors of infall halos and the local tidal field.

5.2.1 Infall halo mass function

The infall halo mass function, sometimes also called the un-evolved subhalo mass function in the literature, is often used to study the evolution of subhalos within their hosts (Giocoli, Tormen & van den Bosch, 2008; Yang et al., 2011). Here we examine whether the infall halo mass function depends on the large scale environment. To this end we calculate the mean infall mass functions for host halos which are located in regions of the highest, intermediate and lowest 20 percetiles of the t_1 distribution. The results are shown in Figure 5.4. In each panel, the three dotted lines show the mass functions of staying infall halos, while the dotted lines connecting squares are the results for the ejected population. To ensure completeness, we only use infall halos in samples M12(S) and M12(E) to calculate the mass functions for host halos of $10^{12.5} \geq M_0 \geq 10^{12.0}\,h^{-1}\mathrm{M}_\odot$, and samples M13(S)+M13(S') and M13(E)+M13(E') for host halos of $M_0 \geq 10^{13}\,h^{-1}\mathrm{M}_\odot$.

The mass functions of infall halos obtained from samples M12(S) and M13(S) +M13(S') are almost independent of t_1. Since these halos are the ones that will stay in their hosts, they are the major sources of halo growth, in the sense that the integration of the mass function should be roughly equal to one. The mass function is also quite independent of host halo mass, consistent with previous findings (Giocoli, Tormen & van den Bosch, 2008). We fit the simulation data with the formula proposed by Giocoli, Tormen & van den Bosch (2008),

$$\frac{dN}{d\ln(m_v/M_0)} = N_0 x^{-\alpha} e^{-6.283x^3}, \quad x = \frac{m_v}{\alpha M_0} \tag{5.2}$$

where m_v is set to be $M_{\rm inf}$. The resultant mean fitting lines are shown in the figure for comparison. As one can see, the empirical formula fits our results well, demonstrating the robustness of our merger tree construction. The mean fitting parameters are $\alpha = 0.67$ (0.68) and $N_0 = 0.43$ (0.40) for M12(S) [M13(S)+M13(S')]. The slopes α obtained here are slightly less than $\alpha = 0.8$ obtained by Giocoli, Tormen & van den Bosch (2008), but the amplitudes are significantly higher than their value, $N_0 = 0.2$. The difference may be caused by different cosmological models and the definition of halos in the two analyses.

Different from the staying population, the mass functions for M12(E) and M13(E)+M13(E') strongly depend on the large scale tidal field. The ejected halo population is much more abundant in regions of stronger tidal field, and the difference becomes larger as the infall halo mass increases. At the high mass

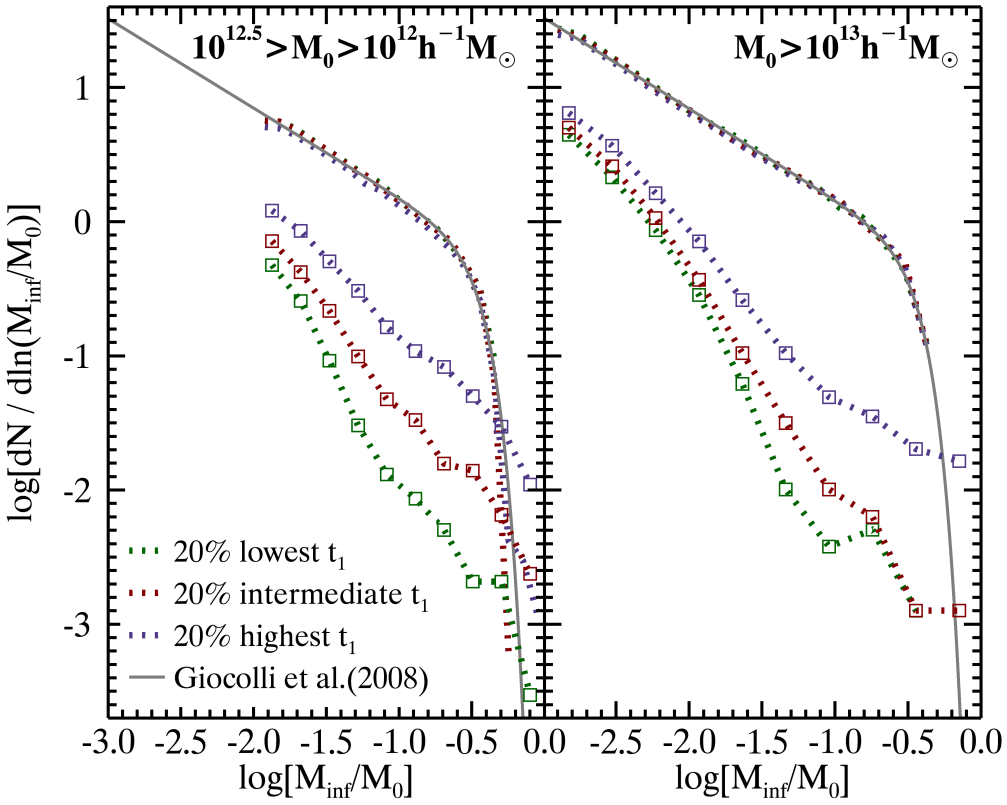

Figure 5.4: The comparison of infall halo mass functions in different environments. The blue, red and green lines correspond to the host halos in the lowest, intermediate, and highest 20 percentiles of t_1. The left panel shows the results for host halos of $10^{12.5} \geq M_0 \geq 10^{12}\,h^{-1}\mathrm{M}_\odot$, and the right panel shows the results of $M_0 \geq 10^{13}\,h^{-1}\mathrm{M}_\odot$. The dotted lines show the staying population of infall halos. Note that the results for the three t_1 samples almost overlap. The dotted lines connecting squares are for ejected halos. The gray lines are the best-fitting results based on the function given by Giocoli, Tormen & van den Bosch (2008).

end, the ejected halo abundance in the 20% highest t_1 regions is about 10 times higher than that at the 20% lowest t_1 regions. This suggests that the large-scale tidal field can affect the accretion of halos, and infall halos in 'hotter' (strong tide) environments are more likely to escape from the potential well of their hosts. The slope of the mass function for the ejected halo population is, on average, steeper than the mass function of the staying population, indicating that halos with lower masses are easier to be ejected. Overall, the ejected population is only a small fraction of the total, and the fraction is higher for lower mass host halos (see Table 5.1).

5.2.2 Orbits of infall halos

Radial and tangential infall velocities

Since the staying population dominates the total infall halos, we first investigate how their acquisitions by their host halos are affected by environmental effects. Let us first look at $v_{\rm r}$ and v_θ, the radial and tangential velocities of infall halos relative to the hosts at $z_{\rm inf}$. The radial direction is defined as the position vector of the infall halo relative to the minimum potential position of the host halo; a negative radial velocity means that the halo is moving towards its host. Figure 5.5 and 5.6 show, respectively, the probability distributions of $v_{\rm r}$ and v_θ, both normalized by the circular velocity of the host, $v_{\rm vir}$, at $z_{\rm inf}$, for samples M12(S), M13(S) and M13(S') in the highest, intermediate and lowest 20 percentiles of the t_1 distribution. Results are shown separately for two narrow infall redshift ranges, low ($z_{\rm inf} \leq 0.4$) and high ($0.75 \leq z_{\rm inf} \leq 1.25$). As one can see, the $v_{\rm r}$ distribution peaks around $-0.9v_{\rm vir}$, while v_θ peaks at a smaller value. These results are in qualitative agreement with those obtained before (Benson, 2005; Wang et al., 2005; Wetzel, 2011; Jiang et al., 2014). The fact that the free-fall velocity near the host virial radius is about $-v_{\rm vir}$ suggests that the radial velocity of an infall halo is primarily produced by the gravity of the host. This interpretation is also supported by the similarity between the distributions for host halos of different mass [samples M12(S) versus M13(S)] at different redshifts. A small fraction of halos are moving outward with very low (positive) velocities and are expected to turn back shortly.

The gravity of the host is not the sole factor that affects the velocity distributions of the infall halos. In fact, the distributions also depend on the environments where the hosts reside. First, the average tangential velocity increases as the tidal force increases. As shown in the top left panel, the peak value of the tangential velocity distribution for low redshift M12(S) increases from $\sim 0.3v_{\rm vir}$ for the lowest 20% of t_1 to $\sim 0.6v_{\rm vir}$ for the highest 20%, in contrast to the peak of the $v_{\rm r}$ distribution, which is almost independent of t_1. Second, the distributions of both $v_{\rm r}$ and v_θ are broader in a stronger tidal field, and the effect is more significant for radial velocity.

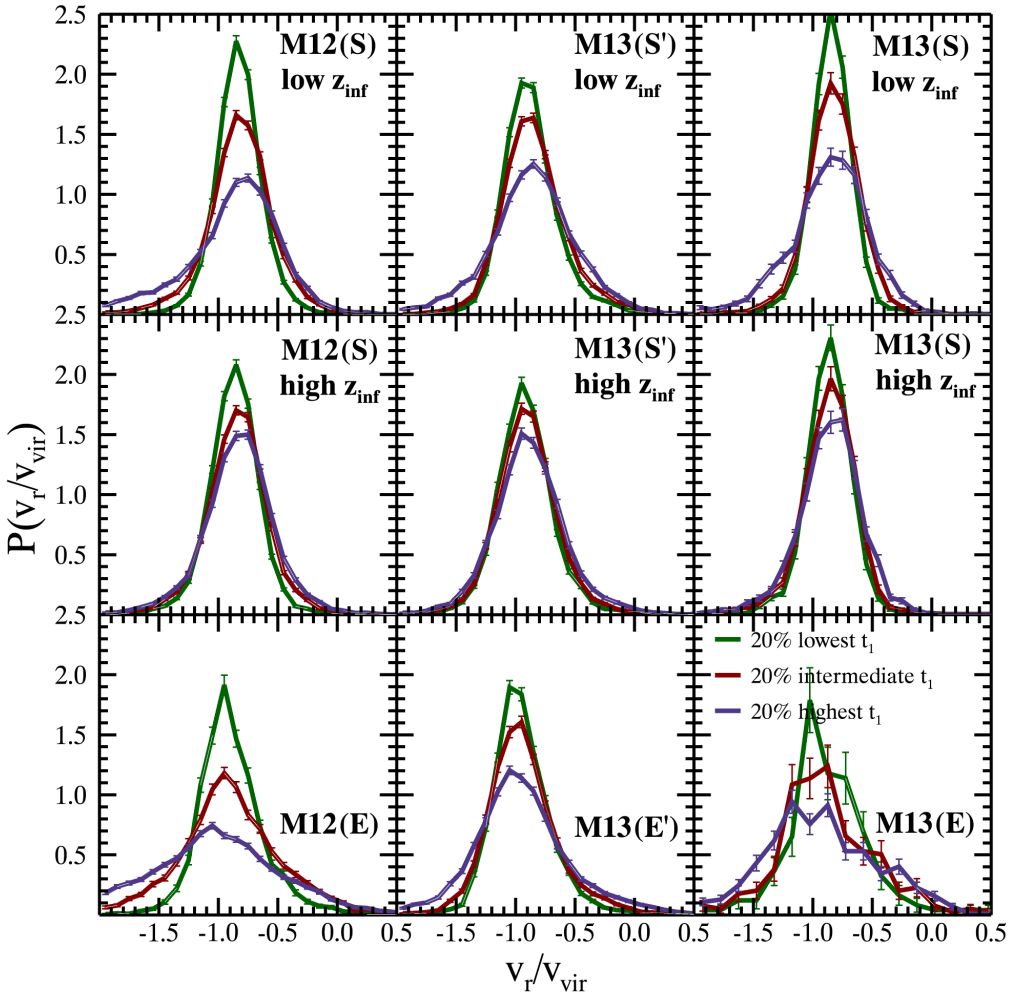

Figure 5.5: The radial velocity distributions of infall halos in different environments. The blue, red and green lines show the results for host halos in the lowest, intermediate and highest 20 percentiles of t_1. Results are shown for infall halos in two different redshift ranges, as indicated in each panel. The velocity is normalized by $v_{\rm vir}$, the virial velocity of the host halo at the infall redshift. The error bars are Poisson errors.

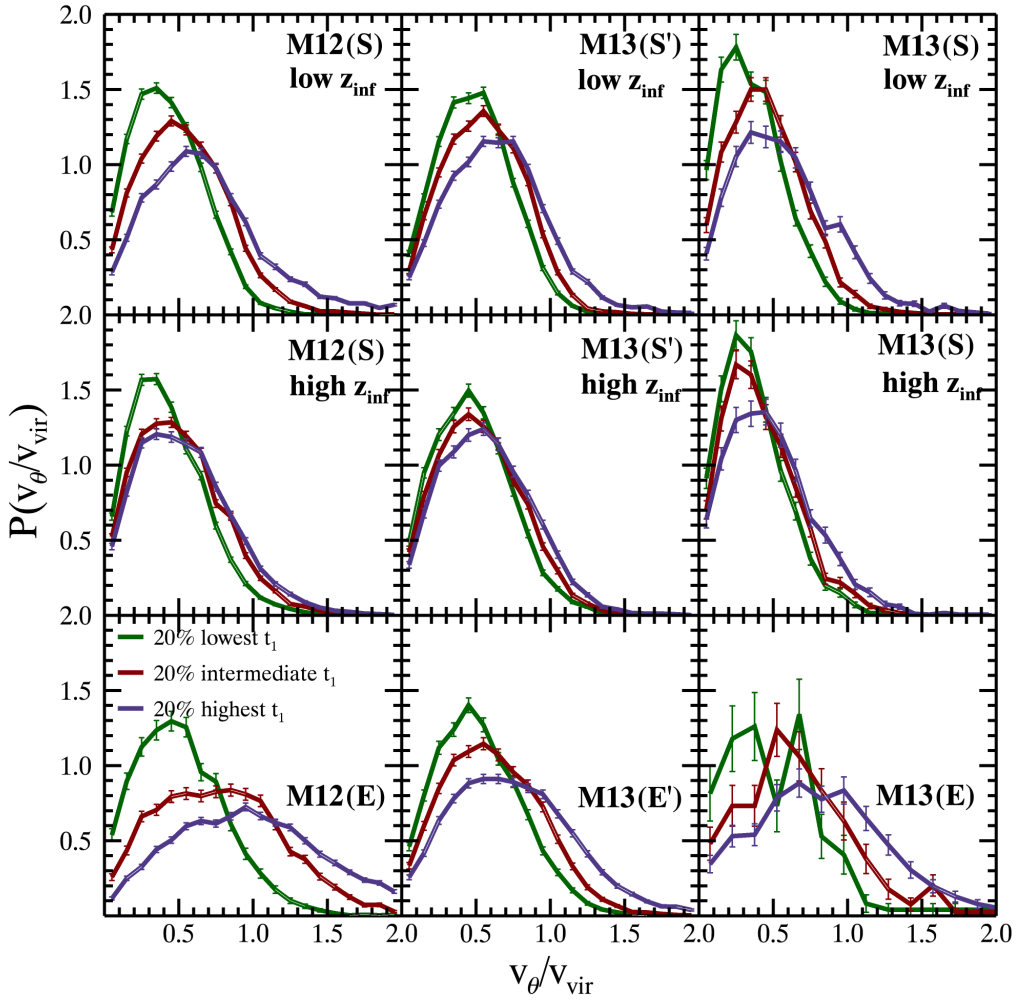

Figure 5.6: The same as Figure 5.5 but for the tangential component of the infall velocity.

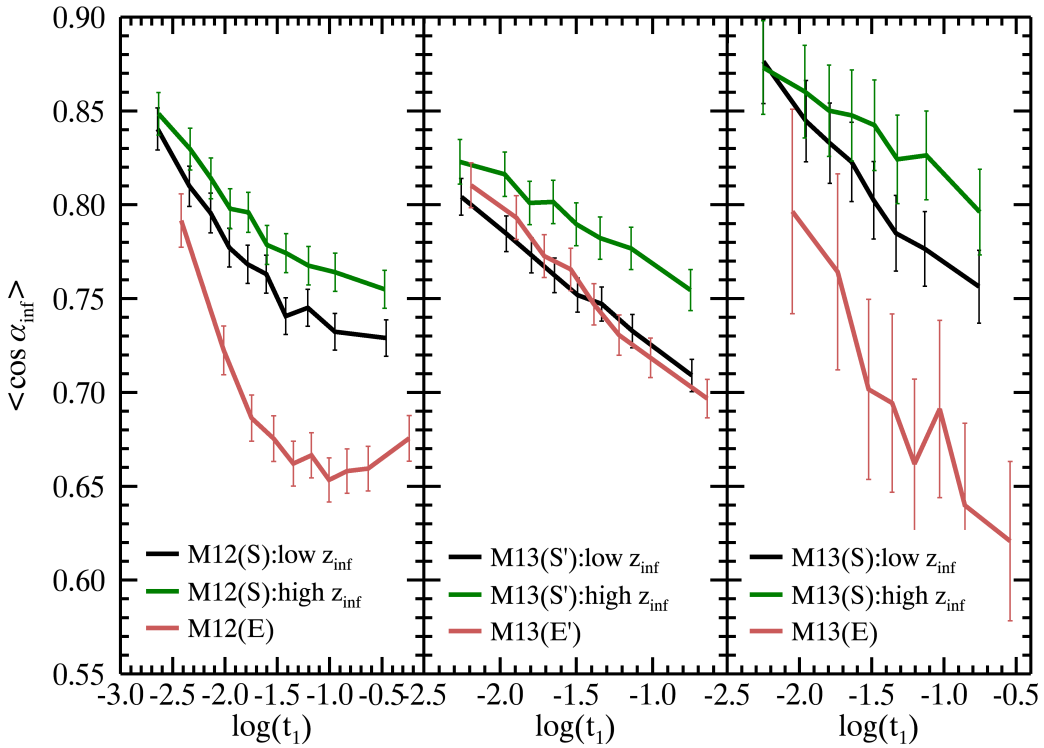

Figure 5.7: The mean cosine of the infall angle $\alpha_{\rm inf}$, defined in equation (5.3), as a function of the tidal field strength, t_1, for different samples as indicated in the panels. For each curve, the t_1 bin sizes are chosen so that each bin contains the same number of halos. The error bars are Poisson errors.

Take the low-redshift M12(S) as an example, the dispersion in the $v_{\rm r}$ distribution changes from 0.19 to 0.27 and to 0.44 from low t_1 to intermediate t_1 and to high t_1, while the dispersion in the v_θ distribution changes from 0.25 to 0.30 and to 0.32.

The dependence on the tidal strength appears weaker for infall halos at higher redshift. There are two possible reasons for this. First, the tidal field, which is estimated from halos at $z = 0$, might not be a good tracer of environments at high redshift. Second, environmental effects are indeed weaker at higher redshift. We will come back to this question later.

Infall angle

Another useful quantity is the infall angle, $\cos\alpha_{\rm inf}$, defined as

$$\cos\alpha_{\rm inf} = \frac{|v_{\rm r}|}{\sqrt{v_{\rm r}^2 + v_\theta^2}}\,. \tag{5.3}$$

We split the infall halo sample into several equal-sized subsamples according to their local t_1, and calculate the mean values of $\cos\alpha_{\rm inf}$ and t_1 for each of these subsamples. The results are shown in Figure 5.7. Note that radial velocity is the dominating component when $v_{\rm r}^2 \geq v_\theta^2/2$, i.e. when $\cos\alpha_{\rm inf} \geq 0.58$. The results clearly show that the accretion flow preferentially moves radially in all environments. Moreover, there is clear dependence of infall angle on the redshift and on the masses of both the infall halo and the host. The accretion flow at high redshift is more dominated by radial motion than at low redshift. This is expected, because environmental effects relative to the self gravity of the hosts are weaker at higher redshift. A comparison between the results for M12(S) and M13(S) suggests that the accretion flow around a more massive host is also more radial.

The infall angle is strongly correlated with the strength of the tidal force, t_1. As the tidal force increases, the mean $\cos\alpha_{\rm inf}$ decreases significantly for all samples. This is consistent with the velocity distributions shown in Figures 5.5 and 5.6. Interestingly, such environmental dependence for infall halos accreted at high redshift ($z_{\rm inf} \sim 1$) is almost as strong as for those with lower $z_{\rm inf}$. This suggests that the tidal field around a halo at $z = 0$ is correlated with the tidal field around its main progenitors at high redshifts. As the large-scale structure in the Universe evolves, the strength of the tidal field at the location of a halo is expected to evolve with time. The tidal field obtained from the halo population at $z = 0$ may serve as an approximation of the *scaled* version of the tidal field at high z (see Section 5.1.3 for more discussion).

Finally, let us look at the ejected halo population, whose results are also presented in Figures 5.5, 5.6 and 5.7. Compared to the staying population, the ejected population has slightly higher mean radial velocities, significantly higher tangential velocities and much broader velocity distributions. These results are expected. A higher tangential velocity means that the orbit is both more loosely bound, which makes a final merger less likely, and more circular, which makes orbital decay due to dynamical friction less effective. Both effects make the sub-halo easier to escape from the host. The dependence of the tangential velocity distribution on the tidal field strength is stronger for ejected halos than for the staying ones, as shown in the lower panels of Figure 5.6, and the dominance of the radial component of the infall velocity also decreases with increasing t_1 more rapidly, as shown in Figure 5.7.

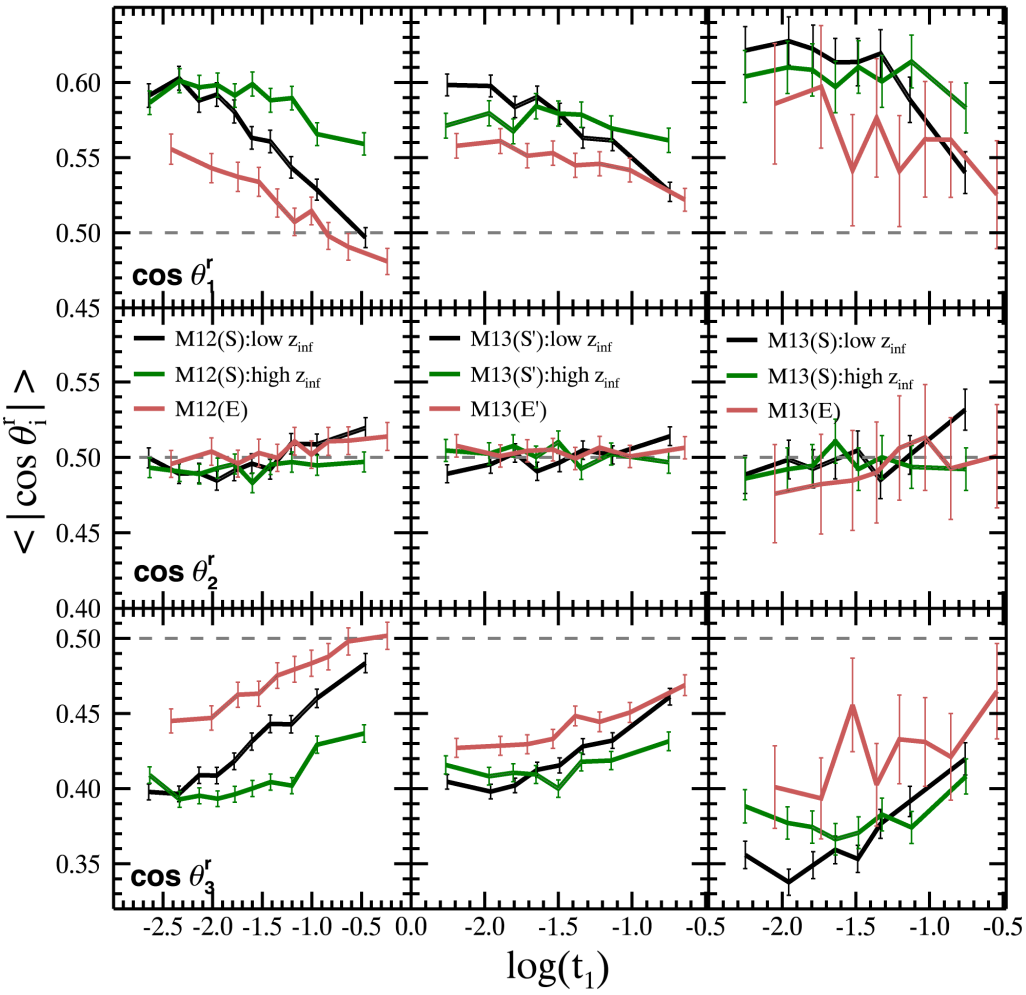

Figure 5.8: The mean of $|\cos\theta_i^r|$ ($i = 1, 2, 3$) defined in equation (5.4), as a function of t_1. From top to bottom, results are shown for $i = 1$ (major axis), $i = 2$ (intermediate axis) and $i = 3$ (minor axis). From left to right, results are shown for different samples as indicated in the intermediate-row panels. The dashed lines indicate isotropic distribution. The error bars are Poisson errors.

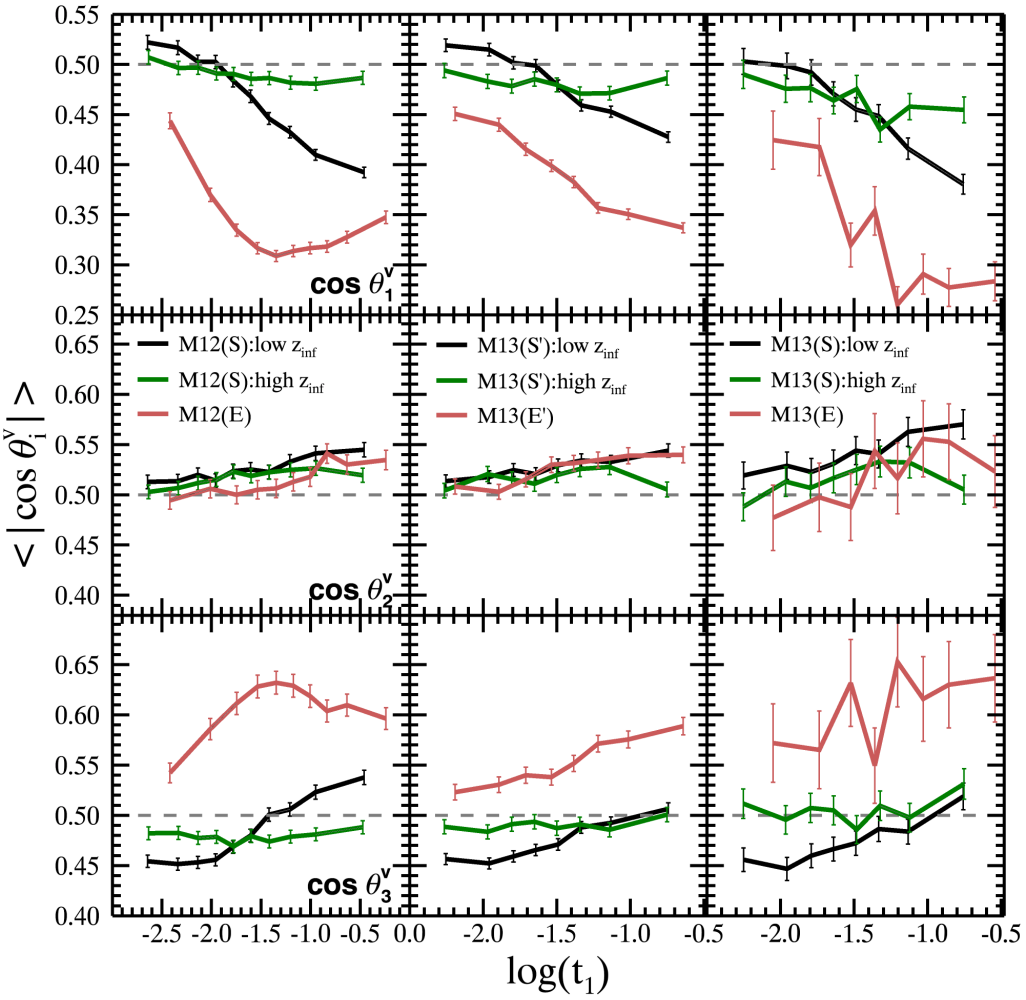

Figure 5.9: The same as Figure 5.8 but for θ_i^v, defined in equation (5.4).

5.2.3 Alignment of accretion flow with tidal tensor

The results shown above may suggest that the velocity field of accretion flow is regulated by the local large scale tidal field.[1] Cosmological tidal field is known to be strongly anisotropic: it stretches the accretion flow along the $\boldsymbol{t}_1$ direction, while compresses it along $\boldsymbol{t}_3$. This suggests that the spatial distribution and velocity field of infall halos are also likely to be anisotropic, and perhaps have alignments with the local tidal tensor. In this subsection, we investigate the alignments of the three eigenvectors of local tidal tensor with the position and velocity vectors of infall halos. The position vector, $\boldsymbol{r}$, of an infall halo is defined to be the vector from the minimum potential position of its host to the infall halo itself, while the velocity vector, $\boldsymbol{v}$, is defined to be its velocity relative to the velocity of the host. We use θ_i^r (θ_i^v) to denote the angle between the position (velocity) vector and tidal eigenvector $\boldsymbol{t}_i$ ($i = 1, 2, 3$), i.e.

$$\cos(\theta_i^r) = \frac{\boldsymbol{r}\cdot\boldsymbol{t}_i}{|\boldsymbol{r}||\boldsymbol{t}_i|}\,; \quad \cos(\theta_i^v) = \frac{\boldsymbol{v}\cdot\boldsymbol{t}_i}{|\boldsymbol{v}||\boldsymbol{t}_i|}\,. \tag{5.4}$$

Here again, we first present the results for the staying population of the infall halos. Figure 5.8 shows the mean $|\cos\theta_i^r|$ as a function of t_1. It can be seen that the position vectors have a strong tendency to align with $\boldsymbol{t}_1$ (the stretching direction) and to be perpendicular to $\boldsymbol{t}_3$ (the compressing direction), and are almost uncorrelated with $\boldsymbol{t}_2$. According to the definition of the tidal field, the large scale mass distribution around a host halo tends to be in a filament along $\boldsymbol{t}_1$ or within a sheet perpendicular to $\boldsymbol{t}_3$. Thus, the accretion mass flows towards the hosts are expected to be preferentially within these large scale structures, and the alignments shown in Figure 5.8 follow directly from this expectation. These results are consistent with that of Libeskind et al. (2014), who found that mass accretion has the preference to be along the direction of the weakest collapse, which is the $\boldsymbol{t}_1$ direction defined here. Comparing the black and green lines in Figure 5.8, we see that the average alignment signal is stronger for infall halos at higher redshift, particularly for low-mass hosts and for hosts located in high t_1 regions. This is unexpected as the tidal tensor is estimated using halos at $z = 0$. One possible reason is that nonlinear effects, which tend to suppress alignment, are weaker at higher z. This interpretation is consistent with the fact that the alignments are weaker in higher t_1 regions where nonlinear effects are expected to be stronger. Regardless its origin, this result suggests that our $z = 0$ tidal field is a valid environmental indicator for halos at high redshift (at least to $z \sim 1$).

Figure 5.9 show the mean $|\cos\theta_v^i|$ as a function of t_1. Like $|\cos\theta_i^r|$ shown in Figure 5.8, $|\cos\theta_v^i|$ shows a strong correlation with the strength of the tidal force,

[1] Note that correlation does not necessarily imply causation unless other possibilities are exhausted. A proof of causation, therefore, needs a much more detailed analysis.

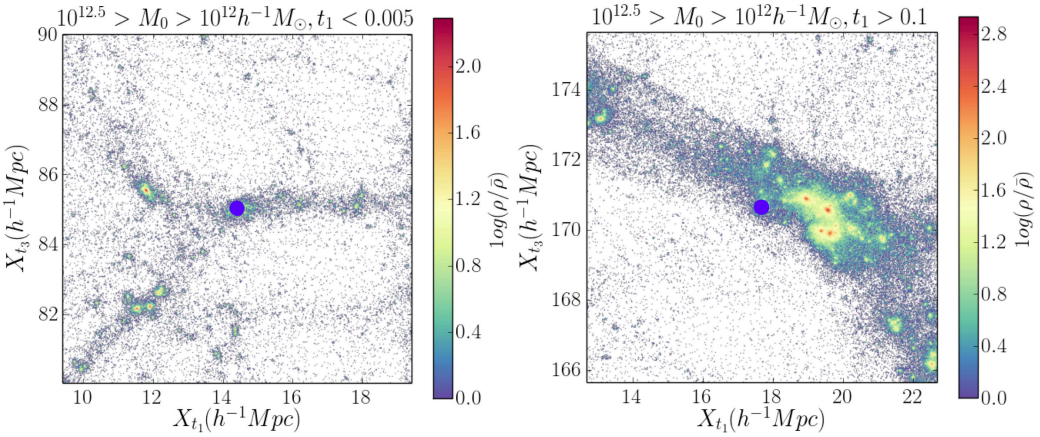

Figure 5.10: The projected density contrast maps around two MW sized halos in weak and strong tidal fields as indicated in the panels. The two halos are shown as blue solid circles at the centers of the panels. The maps are shown in the $\boldsymbol{t}_1$- $\boldsymbol{t}_3$ plane, and the thickness is $5h^{-1}$Mpc. The values of the density contrast are color coded, as shown in the color bars.

and the dependence is stronger for low-mass hosts at low redshift. For example, for M12(S) at low redshift, there appears to be two different accretion patterns depending on the environment within which the host is embedded. In a weak tidal field, infall halos are preferentially accreted along the directions that are parallel with $\boldsymbol{t}_1$ and perpendicular to $\boldsymbol{t}_3$ (see the black solid lines in the left panels of Figure 5.8). The velocity vectors of these infall halos have a weak tendency to be parallel with $\boldsymbol{t}_1$ but a strong tendency to be perpendicular to $\boldsymbol{t}_3$, as shown by the black solid lines in the left panels of Figure 5.9. In contrast, in a strong tidal field, infall halos are accreted along directions that are almost uncorrelated with the tidal tensor, while the velocity vectors tend to be perpendicular to $\boldsymbol{t}_1$ and parallel with $\boldsymbol{t}_3$. For sample M13(S) and M13(S'), and for infall halos with high $z_{\rm inf}$, the overall trends are very similar, albeit weaker.

The dependence on the tidal strength described above is interesting. In particular, why are the alignment signals stronger for host halos located in weak tidal field where large scale tidal field is expected to have a weak impact? The large scale (usually filamentary) structure surrounding a halo in a weak tidal field is not expected to be massive in comparison to the halo itself, and the thickness of the filamentary structure is likely to be comparable to the size of the halo (see Figure 5.10 for an example). For a host halo residing in a small filament, where the eigenvectors $\boldsymbol{t}_1$ and $\boldsymbol{t}_3$ are expected to be parallel with and perpendicular to the filament, respectively, the gravitational field is dominated by the host halo itself. The infall halos, which are located in the filament, are expected to have the

tendency to move along the filament as they fall onto the host, so that the position and velocity vectors of the infall halos both have the tendency to be aligned with the filament. In this case, the role of the tidal field is to produce a 'cold' filamentary structure from which the halo accrete new material. In contrast, for halo located in a strong tidal field, the surrounding structure is usually larger than the halo, even if it is a filamentary structure on a larger scale (see Figure 5.10). In this case, the halo can accrete infall halos from different directions, producing a weak alignment between the position vectors and the tidal eigenvectors. In such an environment, the large scale tidal field plays an important role in determining the motions of infall halos, which generates deceleration of accretion along $\boldsymbol{t}_1$ and acceleration of accretion along $\boldsymbol{t}_3$. This explains why in a strong tidal field, the velocities of the infall halos tend to be parallel with $\boldsymbol{t}_3$ and perpendicular to $\boldsymbol{t}_1$ (Fig. 5.9), even though they still have a (weak) tendency to be distributed along $\boldsymbol{t}_1$ at the time of accretion (Fig. 5.8).

The ejected halos exhibit similar dependence of $|\cos\theta_i^r|$ on t_1. The mean alignment signal is weaker than that for the staying population, indicating that the ejected halos fall onto their hosts in a more isotropic manner. The difference between ejected and staying populations is particularly large in the velocities of infall halos, with the ejected population showing a much stronger tendency of their velocity vectors to be perpendicular to $\boldsymbol{t}_1$ and parallel with $\boldsymbol{t}_3$ in all environments. In the weak tidal field, this velocity - tidal field alignment for ejected halos is opposite to that for the staying population (Figure 5.9). These results together suggest that ejected halos are a special population of infall halos even before they are accreted by their hosts.

5.3 Environmental dependence of halo dynamical properties

In the previous section we have shown that the accretion patterns of halos are correlated with the tidal field at $z = 0$. Since the intrinsic properties of dark matter halos are expected to depend on their formation histories, halo intrinsic properties are expected to be correlated with environment as well. Wang et al. (2011) have investigated the correlation between various halo structural properties with environment. Here we focus on the dynamical properties of dark matter halos, such as halo velocity structure and spin. There have been investigations about how the velocity anisotropy, spin and velocity ellipsoid of halos are affected by environment (Faltenbacher & White, 2010; Bett et al., 2007; Gao & White, 2007; Hahn et al., 2007; Zhang et al., 2009, e.g.). Our approach is different from these studies in that we use tidal field as an environmental indicator. More importantly, we try to

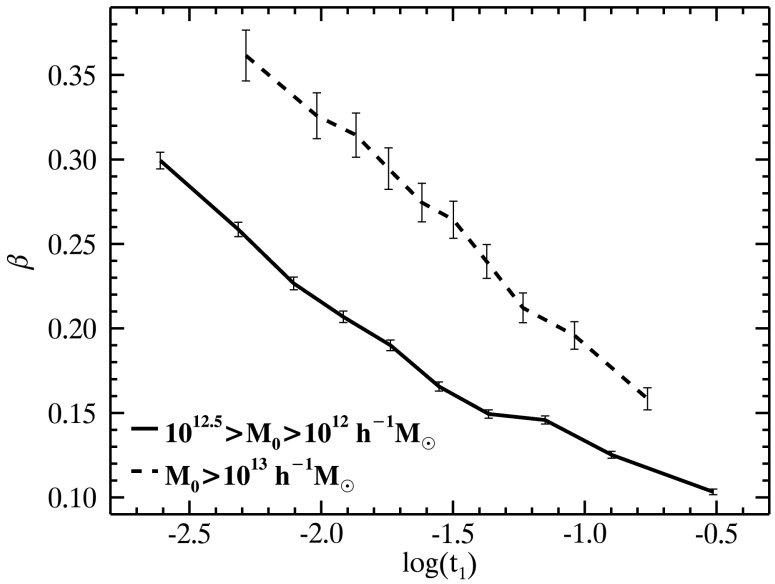

Figure 5.11: The correlation between velocity anisotropy, β defined in equation (5.5), of host halos and t_1 for two mass ranges. All t_1 bins contain equal number of halos. The curves connect the median values of β, while the error bars are Poisson errors.

interpret the environmental effect in terms of the environmental dependence of the accretion we obtained above.

Velocity anisotropy parameter β

We first investigate the velocity anisotropy parameter, which is defined to be

$$\beta = 1 - \frac{\sigma_\theta^2}{2\sigma_{\rm r}^2}\,, \tag{5.5}$$

where $\sigma_{\rm r}$ and σ_θ are, respectively, the radial and tangential velocity dispersion, evaluated using all halo particles. By definition, a negative (positive) value of β implies dominance of tangential (radial) motion, and $\beta = 0$ indicates an isotropic velocity field. Figure 5.11 shows β as a function of t_1 for host halos at $z = 0$ in two mass ranges. There is a clear trend that β decreases monotonically with increasing t_1. The internal velocity fields are dominated by radial motion for halos in weak tidal fields, and are almost isotropic for halos in strong tidal fields. Faltenbacher & White (2010) found that halos of low β are more clustered than those of high β. Given that the tidal field is on average stronger in higher density regions (Wang et al., 2011), our results are consistent with theirs. Note that for a given t_1, β is higher (meaning radial velocities is more dominating) for higher mass halos.

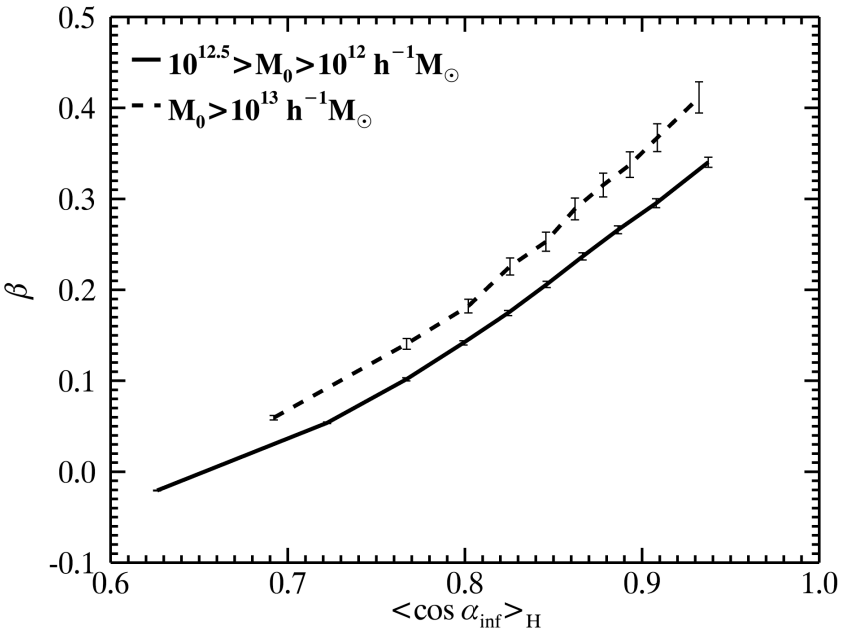

Figure 5.12: The correlation between the velocity anisotropy β and $\langle\cos\alpha_{\rm inf}\rangle_{\rm H}$. For each host halo, $\langle\cos\alpha_{\rm inf}\rangle_{\rm H}$ is the mass-weighted average value over all of its infall halos in the staying population. All $\langle\cos\alpha_{\rm inf}\rangle_{\rm H}$ bins contain equal number of halos. The curves connect the median values of β, while the error bars are Poisson errors.

The velocity anisotropy of halos very likely reflects the anisotropy in the velocity distribution of infall halos. As a test of this, we calculate the mean cosine of the infall angle, $\langle \cos \alpha_{\rm inf} \rangle_{\rm H}$, weighted by the infall halo mass, for each host halo and show β versus $\langle \cos \alpha_{\rm inf} \rangle_{\rm H}$ in Figure 5.12. Here, only staying infall halos are used to calculate $\langle \cos \alpha_{\rm inf} \rangle_{\rm H}$. We see a very strong positive correlation between these two quantities. The more tangential the mean orbit of the infall halos is, the more dominated the host halo is by tangential motions. Given the strong correlations between $\cos \alpha_{\rm inf}$ and t_1 shown in Figure 5.7, the dependence of β on t_1 is straightforward to understand.

To investigate the velocity anisotropy in more detail, we estimate the velocity anisotropy profile, $\beta(r/r_{vir})$, for individual host halos. Here r is the distance to the minimum potential position in the host halo, and $r_{\rm vir}$ is its virial radius. Here we use all particles in each radius bin to calculate the dispersion. Some non-halo particles may be included, but our test showed the effect is small. Figure 5.13 presents the results separately for halos residing in the highest, intermediate and lowest 20% t_1 environments. For clarity, in each case, we only show the profiles of 2% halos randomly selected from the total sample. The median β profiles and the one sigma scatter are also plotted for reference. The large scatter in the innermost bins for the low mass halos are due to small number statistics. These profiles are in broad agreement with those obtained by Ludlow et al. (2011) from a much higher resolution simulation. As one can see from the right panels, the anisotropy profile depends significantly on the tidal field. For halos in the lowest 20 percentile of t_1 distribution, the median β increases monotonously with increasing radius, indicating that the orbits of dark matter particles become increasingly radial as r increases. In contrast, for halos in the highest 20 percentile of t_1, the median β first increases and then decreases with r, reaching a maximum value of $\beta \sim 0.2$ at $r \sim 0.16 r_{\rm vir}$. The velocity dispersion on average approaches isotropy ($\beta \to 0$) in the outermost regions of such halos. The environmental effect decreases with decreasing radius, becoming unimportant at $r < 0.1 r_{vir}$. In the innermost region, the velocity dispersion is quite isotropic (i.e. $\beta \sim 0$), independent of the tidal field.

As shown in Zhao et al. (2003b), a cold dark matter halo grows in an inside-out fashion after its potential well is established. Thus, the outer parts of halos are expected to be dominated by newly accreted material, and the material in the outer part should contain more information about the recent accretion events. This is the primary reason why the velocity structure in the outer parts of halos depends strongly on t_1. The behavior in the inner parts is more difficult to understand. As shown in Figure 5.7, radial accretion is actually more dominating at higher redshift. Since the inner parts are expected to have formed earlier, the weak anisotropy seen in the inner region cannot be due to the initial orbits of infall halos. It is possible that non-linear evolution, such as radial orbit instability (Carpintero & Muzzio, 1995; MacMillan, Widrow & Henriksen, 2006; Bellovary et al., 2008)

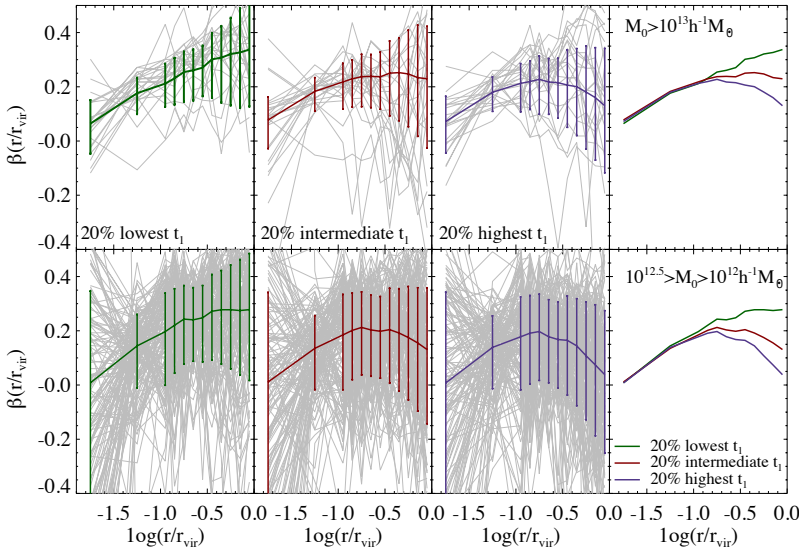

Figure 5.13: The velocity anisotropy profiles (gray lines) for $z = 0$ host halos in different tidal fields, as indicated in the panels. For clarity, profiles of 2% of the halos in each sample are plotted. The median profiles are plotted in colored lines, with error bars representing the 1σ scatter. For comparison, the median profiles for different t_1 are re-plotted in the rightest-hand column.

have suppressed the initial velocity anisotropy. It is also possible that the early assembly of halos is more dominated by major mergers, and the associated violent relaxation reduces the initial anisotropy (Lu et al., 2006).

Spin parameter λ

Next we consider another important halo property, namely the angular momentum. Following common practice, we use the spin parameter,

$$\lambda = \frac{J|E|^{1/2}}{GM_0^{5/2}} \tag{5.6}$$

to characterize the angular moment of a halo, where J is the angular momentum, E the total energy and G the gravitational constant. We adopt the method presented in Bett et al. (2007) to estimate the total energy. The direction of the angular momentum (the spin direction) of a halo is denoted by $\boldsymbol{j}$.

Figure 5.14 shows the median λ as a function of t_1. Clearly, on average halos spin faster in a stronger tidal field, and the dependence is stronger for more massive halos. This result has already been obtained in Wang et al. (2011) and is consistent with the spin-dependent halo clustering found by Bett et al. (2007).

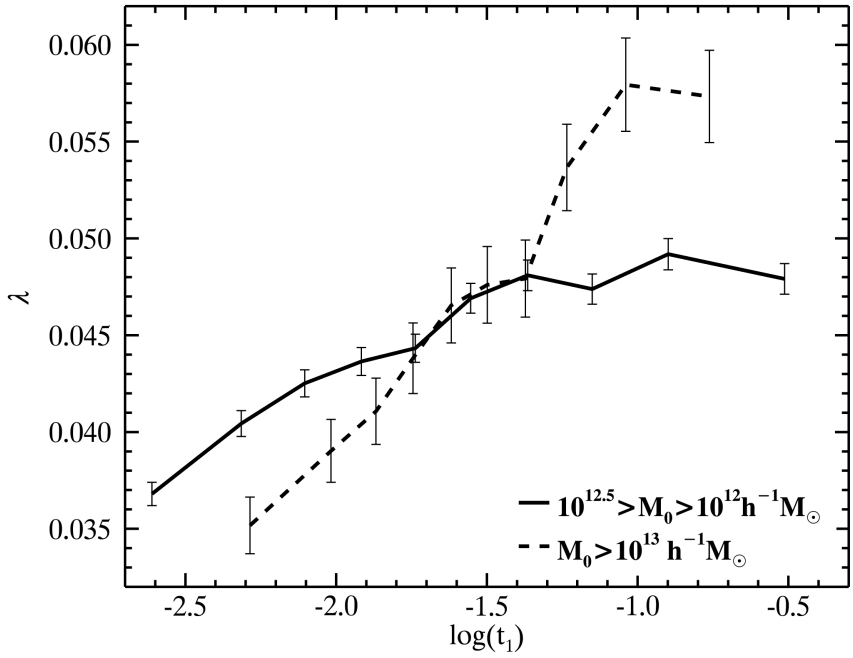

Figure 5.14: The spin parameter, λ defined by equation (5.6), of host halos as a function of t_1. All t_1 bins contain equal number of halos. The curves connect the median values of λ, while the error bars are Poisson errors.

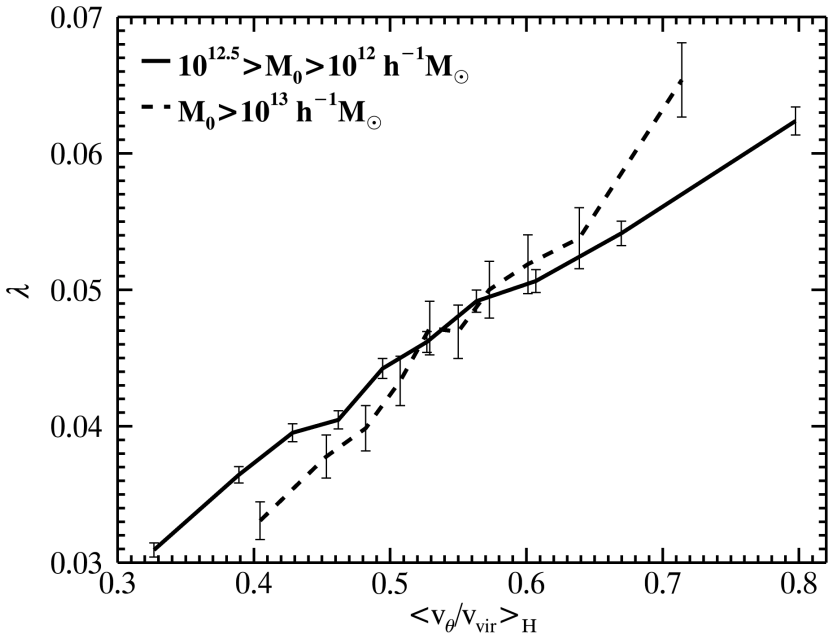

Figure 5.15: The spin parameter, λ, as a function of $\langle v_\theta/v_{\rm vir}\rangle_{\rm H}$. For each host halo, $\langle v_\theta/v_{\rm vir}\rangle_{\rm H}$ is the mass-weighted average value over all of its infall halos in the staying population. All $\langle v_\theta/v_{\rm vir}\rangle_{\rm H}$ bins contain equal number of halos. The curves connect the median values of λ, while the error bars are Poisson errors.

As shown in Figure 5.6, the tidal field can significantly enhance the tangential velocities of infall halos, which may in turn increase the orbital angular momenta of the host halo. To demonstrate this, we estimate the mean tangential velocity, $\langle v_\theta/v_{\rm vir}\rangle_{\rm H}$, of infall halos (the staying population only) for each $z = 0$ host. Figure 5.15 shows how λ depends on $\langle v_\theta/v_{\rm vir}\rangle_{\rm H}$. As expected, the spin parameter has a strong positive correlation with the mean tangential velocity of infall halos. This suggests that halos acquire their angular momenta via the large scale tidal field which regulate the orbital angular momenta of infall halos.

In the literature, halo angular momenta are believed to be generated by tidal torques of the large scale structure (e.g. Porciani, Dekel & Hoffman, 2002a). One unique prediction of the tidal torque theory is that the halo spin axis tends to be parallel with the intermediate axis the tidal field, i.e. $\boldsymbol{t}_2$, and perpendicular to $\boldsymbol{t}_1$ and $\boldsymbol{t}_3$. Wang et al. (2011) detected such alignments in their simulations, but the signals are rather weak (see also Forero-Romero, Contreras & Padilla, 2014b). Some studies also found that halo spin tends to be perpendicular to filament and parallel to sheet (e.g. Hahn et al., 2007; Zhang et al., 2009; Libeskind et al., 2013b), which is consistent with the alignment with the intermediate axis of the tidal field. As we have already demonstrated in Section 5.2, accretion patterns are quite different

between strong and weak tidal fields, and so the alignment signals may also vary with the strength of the local tidal field. To test this, we study the angle ζ_i between $\boldsymbol{j}$ and $\boldsymbol{t}_i$:

$$\cos(\zeta_i) = \frac{\boldsymbol{j} \cdot \boldsymbol{t}_i}{|\boldsymbol{j}||\boldsymbol{t}_i|} \quad (i = 1, 2, 3)\,. \tag{5.7}$$

Figure 5.16 shows the mean of $|\cos\zeta_i|$ as a function of t_1. As one can see, when the tidal field is weak, the alignments are perfectly consistent with the prediction of the tidal torque theory, in that $\boldsymbol{j}$ tends to align with $\boldsymbol{t}_2$. However, as the tidal field gets stronger, the alignments become weaker and weaker. For small halos in regions of high t_1, the trend is eventually reversed so that the spin tends to be aligned with $\boldsymbol{t}_1$ and perpendicular to $\boldsymbol{t}_2$. This reversal is caused by the strengthened tidal truncation of accretion along the $\boldsymbol{t}_1$ direction where the tearing by the tidal field is the strongest. In an analysis of spin alignments using all halos (or galaxies) without regarding their local tidal fields, the opposite trends in strong and weak fields may cancel each other and weaken the total signal. It is thus important to take into account the local tidal field strength when investigating spin alignments in both observation and numerical simulation.

Velocity ellipsoid

Finally, we examine the second moment tensor of the internal velocity field of a halo, defined as

$$I^v_{jk} = \sum_n v_{n,j} v_{n,k}\,, \tag{5.8}$$

where $v_{n,j} (j = 1, 2, 3)$ are the three velocity components of the nth particle in the halo. The square root of the eigenvalues of the tensor can be used to represent the principal axes, I^v_1, I^v_2 and I^v_3 ($I^v_1 \geq I^v_2 \geq I^v_3$), and the axis ratios, such as I^v_3/I^v_1, to characterize the velocity ellipsoid. The corresponding eigenvectors, $\boldsymbol{I}^v_1$, $\boldsymbol{I}^v_2$ and $\boldsymbol{I}^v_3$, represent the directions of the major, intermediate and minor axes of the velocity ellipsoid, respectively.

To check the alignment between the eigenvectors of the velocity tensor and the tidal field, we use the angle ϕ^v_i defined as

$$\cos(\phi^v_i) = \frac{\boldsymbol{I}^v_i \cdot \boldsymbol{t}_i}{|\boldsymbol{I}^v_i||\boldsymbol{t}_i|} \quad (i = 1, 2, 3)\,. \tag{5.9}$$

Figure 5.17 shows the mean of $|\cos\phi^v_i|$ as a function t_1. In weak tidal field, $\boldsymbol{I}^v_1$ tends to be parallel with $\boldsymbol{t}_1$, but an opposite trend is seen in strong tidal field. The trend in $|\cos\phi^v_3|$ is very similar but slightly weaker, and there is no significant alignments between $\boldsymbol{I}^v_2$ and $\boldsymbol{t}_2$ regardless of tidal field strength. The transition is similar to what is seen in the relationship between $\cos\theta^v_i$ and t_1 (see Section 5.2.3), and it

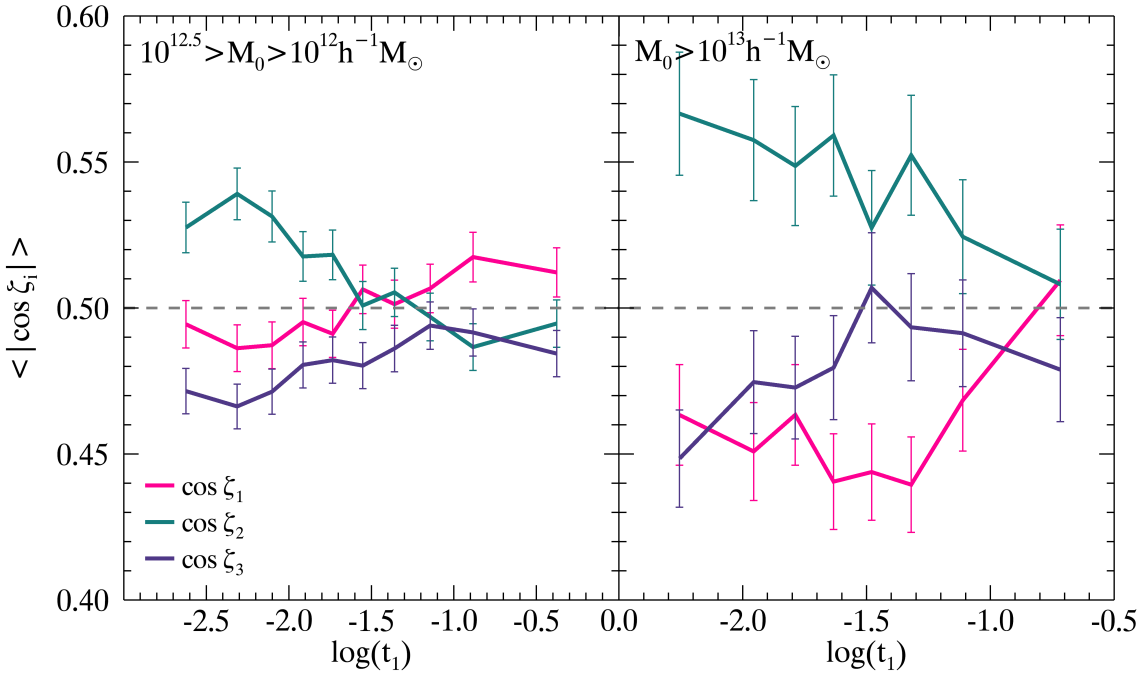

Figure 5.16: The mean of $|\cos\zeta_i|$, a measure of the alignment between the tidal field and halo spin defined by equation (5.7), as a function of tidal field strength t_1. All t_1 bins contain equal number of halos. The error bars are Poisson errors. The horizontal lines indicate no alignment.

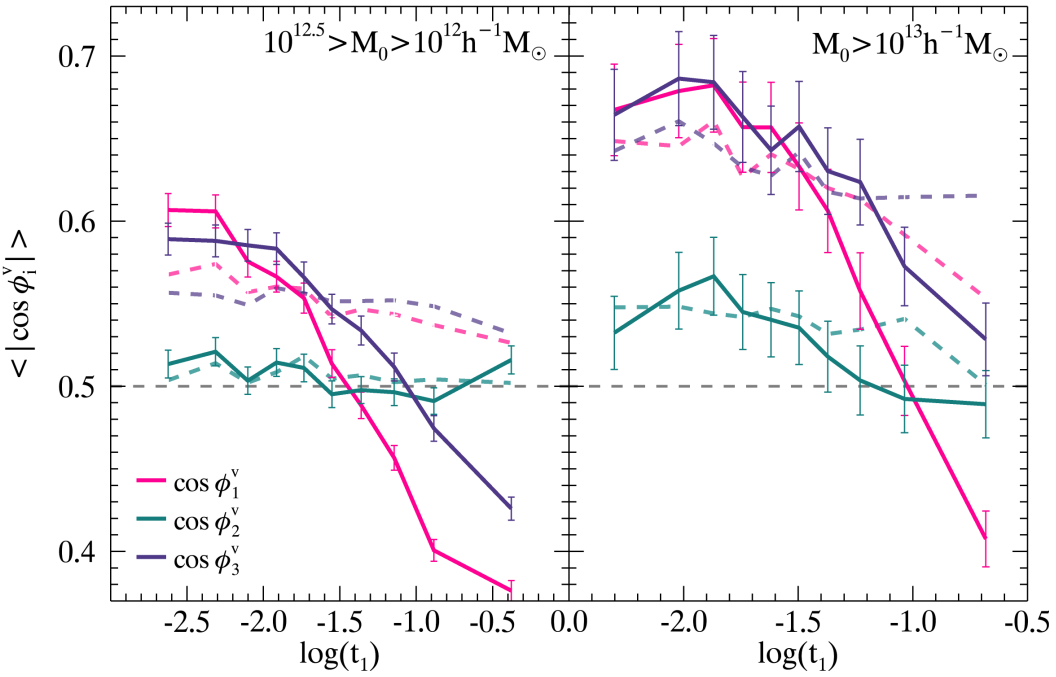

Figure 5.17: The mean of $|\cos\phi_i^v|$, defined by equation (5.9), as a function of t_1. All t_1 bins contain equal number of halos. The solid lines are obtained from using all particles in a halo, while the dashed lines use halo particles in the inner part with $r \leq 0.1 r_{vir}$. The Poisson errors, which are the same for both the solid and dashed curves at a given t_1, are shown only on the solid curves. The horizontal lines indicate isotropic distribution.

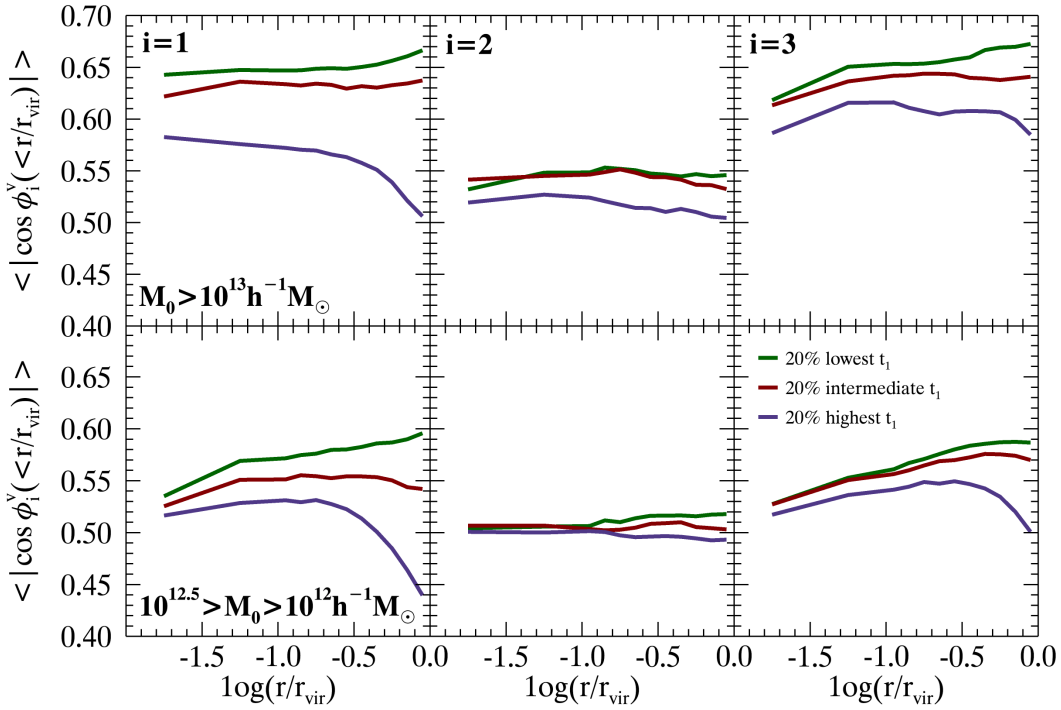

Figure 5.18: The mean alignment profile within individual halos located in tidal fields of three different t_1 20 percentile intervals. Here $|\cos\phi_i^v(< r/r_{vir})|$ measures the alignment between tidal field tensor and velocity ellipsoids obtained using particles within r/r_{vir}.

may be possible that the results shown in Figure 5.17 can be understood in terms of halo accretion. As shown in Figure 5.9, the velocities of infall halos tend to be parallel with $\boldsymbol{t}_1$ and perpendicular to $\boldsymbol{t}_3$ in weak tidal field. If the host halo retains the velocity structure of the infall halos, the major (minor) principal axes of its velocity ellipsoid are expected to be parallel with $\boldsymbol{t}_1$ ($\boldsymbol{t}_3$), as shown in Figure 5.17. Similarly, the different accretion pattern at high t_1 can also explain why $\boldsymbol{I}_1^v$ ($\boldsymbol{I}_3^v$) tends to be perpendicular to $\boldsymbol{t}_1$ ($\boldsymbol{t}_3$) in strong tidal fields.

In is interesting to see how the velocity ellipsoid in the inner halo regions, where galaxies are located, are aligned with the local tidal field. To do this, we calculate the alignment between the tidal field and the velocity ellipsoid of the halo particles within some radius r. The dashed curves in Figure 5.17 show the results for $r = 0.1r_{\rm vir}$, and the averages of $|\cos\phi_i^v(< r/r_{vir})|$ are shown as functions of r/r_{vir} in Figure 5.18. It is evident that the velocity ellipsoids of the inner halo regions align with the tidal field in a different way from the whole halos. In weak tidal fields, the alignment signals in the inner regions are slightly weaker than those for the whole halos. In strong tidal field, however, the alignments of the inner

ellipsoids one average are opposite to the whole halo. For example, for low mass halos, the major and minor principal axes of the inner velocity ellipsoids tend to be parallel with $\boldsymbol{t}_1$ and $\boldsymbol{t}_3$, respectively, but they tend to be perpendicular to each other for the whole halos. This suggests that the accretion pattern at early epoch is similar to that in weak tidal field environments at low redshift.

5.4 Discussion and summary

In this work, we investigate the environmental dependence of halo accretion and their impact on the halo dynamical properties. We construct halo merger trees from N-body simulations and identify infall halos that are about to merge with their hosts. The infall halos are divided into two populations: the staying population which remain as subhalos within their hosts at $z = 0$; the ejected population which are ejected by their hosts at presented day. We use the large scale tidal field estimated from the halo population at $z = 0$ as environmental indicator.

We first investigate the infall halo mass functions in various tidal fields. The mass function for the staying population is quite independent of both the tidal field and host halo mass. In contrast, the ejected halo mass function depends strongly on the tidal field. In a stronger tidal field, infall halos are more easily ejected by their hosts at $z = 0$, and smaller infall halos are more likely to be ejected than massive ones.

We then check the dependence of the orbital parameters of infall halos on local tidal field. The tidal field does not significantly affect the average radial velocities of infall halos, but can generate tangential motions. Consequently, infall halos in stronger tidal fields tend to have higher mean tangential velocities, larger infall angles and higher velocity dispersions. These results suggest that tidal field tends to pull the accretion flow into the orbit of the host and enhance the velocity dispersion among the infall halos, making the accretion flow 'hotter' and more difficult to capture by the host.

We find that the accretion patterns are different between strong and weak tidal fields. In weak tidal fields, the positions of infall halos relative to their hosts have a strong tendency to be parallel with the stretching direction of the tidal field, $\boldsymbol{t}_1$, and perpendicular to the compressing direction, $\boldsymbol{t}_3$. Similarly, the velocities tend to be parallel with $\boldsymbol{t}_1$ and perpendicular to $\boldsymbol{t}_3$. The situation in strong tidal fields is rather different, or even the opposite: the alignments between the position and tidal vectors become weaker or even absent, and the velocities tend to be perpendicular to $\boldsymbol{t}_1$ and parallel with $\boldsymbol{t}_3$. Such difference is particularly strong for infall halos at low redshift around low-mass hosts.

The ejected population shows very different behavior from the staying population. They have much higher tangential velocities. In particular, the velocities have

a strong tendency to be perpendicular to $\boldsymbol{t}_1$ and parallel with $\boldsymbol{t}_3$ in both weak and strong tidal fields. Ejected halos are more abundant in stronger tidal fields because the larger and more tangential velocities generated by the tidal forces make the infall halos more difficult to hold by their hosts.

The environmental effects of halo accretion are imprinted on the halo dynamical properties. The environmental dependence of infall angles results in a correlation between the velocity anisotropy and tidal field. In particular, the large scale tidal field can affect the anisotropy down to radius much smaller than the virial radius. Tidal field increases the tangential velocities of infall halos, producing a positive correlation between halo spin and the strength of local tidal field. The alignment signal of spin with tidal field is different between weak and strong tidal fields; only in weak tidal fields does the spin-tidal field alignment follow the prediction of the tidal torque theory, with the spin parallel to the intermediate axis and perpendicular to the major axis of the tidal tensor, while in strong fields the alignment is the opposite, at least for low-mass halos. Finally, we find a dramatic transition in the alignment between the principal axes of halo velocity ellipsoid and the tidal field tensor in strong and weak tidal field, A radial dependence for this alignment is also found, which differs between weak and strong tidal fields. All these indicate that large scale tidal field affects halo dynamical properties via regulating the flow patterns around halos.

Our results suggest the tidal field describes well the following two aspects of environmental effects. First, strong tidal field (i.e. larger t_1) tends to make the surrounding environment 'hotter', thereby boosting the fraction of the ejected sub-halos, and increasing the tangential component of velocity and the velocity dispersions. This affects halo dynamical properties, making the internal velocity field less radial and boosting the angular momentum in a way that is different from the predictions of the tidal torque theory. Second, the local tidal field describes well the local density and velocity structures from which material is accreted in halos, which in turn explains how halo intrinsic properties are correlated with local tidal fields.

Our results have important implications for observations. For example, our results suggest that the correlation between spin axes of disk galaxies and the large scale structure should be studied separately for the weak and strong tidal fields. The fact that strong alignments of halo velocity ellipsoids with local tidal fields extend all the way to halo central parts suggests that the orientations of elliptical galaxies should be tightly correlated with the local tidal fields. The predicted dependence of such alignments on the strength of local tidal fields can also be tested using a large sample of elliptical galaxies. Furthermore, the infall patterns around halos can be studied by using the distributions and velocity fields traced by satellite galaxies in and around dark matter halos represented by galaxy groups. Since the tidal fields enhance the tangential velocities of infall halos, we may expect the dynamical time

scales relevant to mergers to be larger for those located in stronger tidal fields. This difference in dynamical time scales may lead to differences in the abundance and properties of the satellite population. We will come back to some of these problems in our future work.

Chapter 6

Bimodal Age Distribution of Accreted Subhalos

The importance of halo assembly history is realized by more and more people. While for a subhalo, to fully understand its whole lifetime is much more complicated. Before being accreted by its host, it survived as a distinct halo with its own formation history. After accretion, there exist complicated interactions between subhalo and host, subhalo and subhalo, including tidal stripping, dynamical friction, etc.. However little work has been done for the asesembly history of subhalos before accretion. Sheth (2003) developed a model for the spatial distribution and abundance of sub-clumps in halos. He found subhalos of the same mass with hosts of different mass have quite different formation redshifts. In this work, we are going to study the pre-accretion phase for subhalos using N-body simulations.

Although a full understanding of the baryonic process inside halo is far beyond, people found good relations between some basic properties between galaxies and halos. For example, the total stellar mass of galaxies and halo mass. A recent study (Bray et al., 2016) using the cosmological hydrodynamic simulation "Illustris" shows the existence of the relation between galaxy color and halo age. Even though it has a non-neglected scatter, the trend showing red galaxies live in old halos is pretty certain. Another indirect evidence for this color-age relation is the widely success of the "age matching" method (Hearin & Watson, 2013; Hearin et al., 2014; Chaves-Montero et al., 2016; Paranjape et al., 2015). "Age matching" first matches the abundance of the subhalos beyond a certain mass with the abundance of galaxies beyond a certain stellar mass as previous abundance matching technique, then it exploits one more halo property representing its formation history to connect with galaxies' color or SFR. "Age matching" gives consistent measurements with observations in galaxy clustering of red and blue galaxies, shear measurement and "galactic conformity" (Hearin, Behroozi & van den Bosch, 2016; Kauffmann et al., 2013). All those studies show the necessity of a thorough study on formation history

especially for subhalos. Further more, "age matching" successfully reproduces the galaxy color bimodality, which is mainly contributed by satellite galaxies (Skibba & Sheth, 2009). Such kind of bimodality has not yet been found in N-body dark matter simulations. In this work, we report for the very first time a bimodal feature of subhalos' formation time.

The structure of the chapter is as following. In Section 6.1, we introduce the details on the simulation we used, and the methods for identifying the accreted subhalos. Also, we will give the definitions for accretion redshifts and subhalos' formation redshifts. In Section 6.2, we show the results for $P(\frac{1+z_{\rm f}}{1+z_{\rm peak}}|z_{\rm peak})$ and explain its bimodality using two phase halo MAH. Section 6.3 gives the final summary and discussion.

6.1 Numerical simulations and halo merger tree

6.1.1 Simulation and halo merger tree

In this work, we use a N-body simulation run by Gadget-2 (Springel, 2005). The simulation adopted a flat ΛCDM cosmological model from WMAP9 constraints (Hinshaw et al., 2013), with $\Omega_{\Lambda,0} = 0.718$, $\Omega_{\rm m,0} = 0.282$, $\Omega_{\rm b,0} = 0.046$, $h = H_0/(100\,{\rm km\,s^{-1}\,Mpc}) = 0.697$, $\sigma_8 = 0.817$ and $n_s = 0.96$. The CDM density field is traced by 2048^3 particles, each with mass $m_{\rm p} \approx 7.29 \times 10^7\,h^{-1}{\rm M}_\odot$, from $z = 120$ to $z = 0$ in a cubic box of a side length $200\,h^{-1}$Mpc. The gravitational force is softened isotropically on a comoving length scale of $2\,h^{-1}$kpc (Plummer equivalent). We output 100 snapshots from $z = 20$ to $z = 0$ equally spaced in the logarithm of the expansion factor.

The dark matter halos are identified with FOF group algorithm (Davis et al., 1985) with a linking length of 0.2b, where b is the mean inter particles separation. We resolve all groups with at least 20 particles. Further more, we run SUBFIND (Springel et al., 2001) to acquire the self-bound subhalo catalog for each snapshot. Then we use those subhalos to construct merger trees (Boylan-Kolchin et al., 2009). Each subhalo could have at most one descendant which inherits the largest particles (weighted by the binding energy of the particle) from its progenitors. Throughout the paper, we define the halo mass to be the mass contained in a spherical region (centered on the lowest gravitational potential well point) with average density equals $200\rho_{\rm crit}$, where $\rho_{\rm crit}$ is the critical density of the universe. For subhalos, we do not measure their halo mass, since they are located within the main halos and usually severely stripped by the gravitational potential of their main halos.

The halo merger trees are constructed using the algorithm shown in Springel et al. (2005). Here, we give a brief introduction to it. For a given subhalo (or main halo), their particles are assigned a weight that decreases with the binding

energy, which is calculated using the particles within this halo. We then search in the subsequent snapshot the subhalos and main halos, which contain some of particles of the halo in consideration. Among these halos, the one, which have the highest weight of common particles, is chosen as the descendant of the halo. This method allows one to trace the complex evolution history of a halo, for example, that a main halo is accreted and becomes a subhalo or a subhalo is ejected out and becomes a main halo.

6.1.2 Accreted subhalo identification

The accreted subhalos are identified in a similar way as in Xie & Gao (2015), that is, to identify all the distinct halos whose descendants have ever shown up in a host halo's main trunk. Below is a brief description of the searching method.

First, we find all main trunks by tracing the most massive progenitors of hosts. Then we recognize all distinct halos at $z > 0$ whose descendants are/used to be within the virial region R_{vir} of the main trunk as accreted subhalos. By applying this algorithm, we're able to include all merger events that has ever happened on the merger tree, including sub-branch or sub-sub-branch merger events.

The accetion redshift $z_{\rm peak}$ is defined as the redshift when the accreted subhalo's mass $M_{\rm peak}$ reaches its peak value in its lifetime. Similar to the formation redshift definition of host halos, $z_{\rm f}$ of subhalos is defined as the redshift when the accreted subhalo first reaches $M_{\rm peak}/2$. We would like to specify here that we only do such calculation for accreted subhalos with at least 100 particles. Throughout the paper, M_0 is the notification for the mass of host halo at $z = 0$, and we restrict our study for halos with $10^{11} < M_0 < 6 \times 10^{14}\, h^{-1}{\rm M}_\odot$, $M_{\rm peak} > 100 m_{\rm p}$, and $M_{\rm peak}/M_0 < 1$.

6.2 Bimodal formation redshift distribution

In this section, we are going to show explicitly the main results for the distribution of formation redshift and provide a consistent explanation.

Intriguingly, we found a bimodal $z_{\rm f}$ distribution for accreted subhalos when $z_{\rm peak}$ is fixed, as shown in the left panel of Figure 6.1. The bimodal feature is mostly obvious when we use the parameter $(1 + z_{\rm f})/(1 + z_{\rm peak})$ which cancels the effects of the bin width. Further more, the distribution can be fitted very well by a double log-normal distribution (see the solid lines in the figure). For subhalos accreted at very high redshift ($z_{\rm peak} \sim 7$), almost all of them form right before the accretion, as shown by the narrow one peak distributions. As $z_{\rm peak}$ decreases, a second peak appears, and it becomes more and more dominant. At $z_{\rm peak} \sim 2$, the two components are even comparable to each other. When $z_{\rm peak}$ is very low ($z_{\rm peak} \sim 0$), the first peak is getting less obvious. In the following, we are going to

denote the subhalos contributing to the first peak as the *young population*, and the others that contribute to the second peak as the *old population*. A more careful check reveals that for the young population, its peak value and dispersion don't vary too much with $z_{\rm peak}$. On the contrary, both the peak value and dispersion of the old population increase significantly with decreasing $z_{\rm peak}$. At fixed $z_{\rm peak}$, if we further divide the samples using host halo mass M_0 or accretion mass $M_{\rm peak}$, we found the bimodal distribution barely depends on M_0, yet weakly depends on $M_{\rm peak}$, as shown by the right two panels of Figure 6.1. As an indicative example, we choose only the subhalos with $1.4 < z_{\rm peak} < 1.5$, thus we could have relatively good statistics and clear bimodal feature at the same time. Basically, the young population is larger for high $M_{\rm peak}$ sample, which is consistent with the fact that massive halos usually form later. And the weak dependence on M_0 and $M_{\rm peak}$ shows explicitly that the bimodal feature in the left panel does not originate from the dependence on $M_{\rm peak}$ and M_0 for either $z_{\rm f}$ or $z_{\rm peak}$. In Section 6.2.1, we will give an explanation for these counter-intuitive trends.

Numerical simulations suffer varying numerical effects. To relieve the concern that the above bimodal feature is raised from some numerical effects, we have done various check. We first checked how resolution affects our results. We use a simulation with boxsize of $500\,h^{-1}$Mpc and traced by 3072^3 particles, with all the other settings are the same as the one we used. We found when we apply the same cut on M_0, $M_{\rm peak}$, and $z_{\rm peak}$, the distribution of $z_{\rm f}$ measured in the two simulations are indistinguishable from each other. This proves that our results are free of resolution effect. As a consistent check, we did the same measurements on the two suits of ultrahigh resolution simulations of individual dark matter haloes from the Phoenix and the Aquarius projects (Gao et al., 2012; Springel et al., 2008). The bimodal feature persists. The same stands when we do the measurements with Millennium simulation (Springel, 2005).

The other main concern is the definition of accretion redshift and formation redshift. The definition adopted by us, i.e. $z_{\rm peak}$ is found to be more related with the stellar mass of satellite galaxies (Guo et al., 2010; Watson & Conroy, 2013). Other commonly used definition for accretion redshift are: the time when $V_{\rm max}$ reaches the maximum value in its lifetime (Conroy, Wechsler & Kravtsov, 2006), and the time right before becoming a subhalo of a FOF halo (Li & Mo, 2009; Shi, Wang & Mo, 2015). We did a test with the definition based on $V_{\rm max}$, and found the accretion redshift, $z(V_{\rm peak})$ is slightly higher than $z_{\rm peak}$, yet the bimodal feature for $z_{\rm f}$ won't disappear. However, when adopting the second accretion definition, the bimodal feature is getting less obvious yet still existing. This is the mainly caused by the fact that, when a halo approaches a larger halo, the tidal effects are getting stronger and the imprints from its assembly history may be smeared off. Things are getting more complicated when it comes to the definition of $z_{\rm f}$ (for a comprehensive review and comparison, see Li, Mo & Gao (2008)). Here we

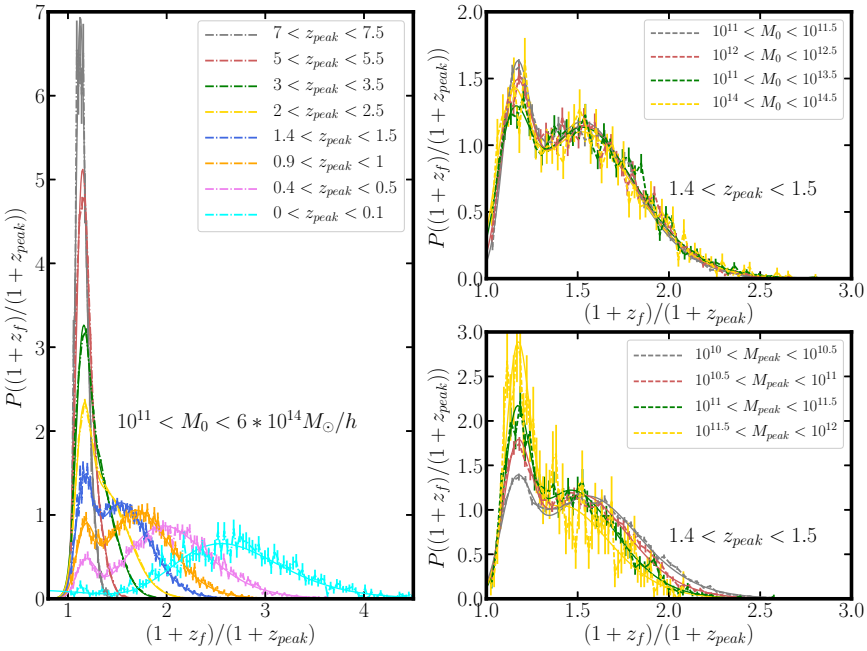

Figure 6.1: Left panel: Distribution of $(1 + z_f)/(1 + z_{peak})$ for subhalos accreted at varying redshift, z_{peak}, as shown by the label. Here $M_{peak} > 100 m_p$. Right Panel: Distribution of $(1 + z_f)/(1 + z_{peak})$ for varying host halo mass, M_0 (upper panel), and for varying subhalo halo mass, M_{peak} (lower panel). In both panels, we show only the distribution for subhalos with $1.4 < z_{peak} < 1.5$ for clarity. The solid lines are double log-normal fitting results. The error bars are Poisson errors.

simply adopt the most common definition. As you will see in the following section, even though $z_{\rm f}$ might be too simple for characterizing the mass accretion history (MAH), it does describe explicitly the general trend rather well. We would like to emphasize that the above check is by no means comprehensive, but it support the reliability of the bimodal feature.

One more thing that is worthy to be mentioned is that tests show that the existence of the bimodal feature doesn't relate with the state/final fate of the accreted halos. More specifically, we checked the distribution for several populations: the "wavering" population, i.e., halos enter the host at high redshift and leave and re-enter later; the "surviving" population, i.e. halos with their descendants survived the tidal effect and being a subhalo of the host at z=0. We found the bimodal feature persists for both the "wavering" population and the "surviving" population.

As discussed in the above, the definition of $z_{\rm f}$ is still under debate. Perhaps a more direct check would be plotting the MAH, $M(z)$, for the two populations. The MAH traces the mass growth history of the most massive progenitors. In Figure 6.2, we plot $M(z)$ normalized by $M(z_{\rm peak})$ versus $(1+z)/(1+z_{\rm peak})$ for young population (left two columns) and old population (right two columns) separately. The upper panels are for intermediate host halo and lower panels are for massive host halos. We further divide the samples into two $M_{\rm peak}$ ranges: $10^{10}-10^{10.5}\,h^{-1}{\rm M}_\odot$ and $10^{11}-10^{11.5}\,h^{-1}{\rm M}_\odot$, as shown in the titles. Clearly, the two population have quite different MAH. The old population is characterized by a fast growth at high z, and its mas accretion slows down before reaching $M_{\rm peak}$. In contrast, the young population shows much faster accretion both at high z and low z than the old population, especially for the short period before $z_{\rm peak}$. This provides a consistent check on the robustness of our measurements with $z_{\rm f}$.

To understand the origin of this bimodal feature, we start by comparing them with the general distinct halo samples. We choose four snapshots with redshift $z_{\rm i}=0.2,1,2,3$ and exclude the ejected halos from the sample, here the subscript i stands for the "i*th*" snapshot. The probability distribution function of $z_{\rm f}$ for two mass ranges, $10^{11}<M_{\rm i}<10^{11.5}\,h^{-1}{\rm M}_\odot$ and $10^{12}<M_{\rm i}<10^{13}\,h^{-1}{\rm M}_\odot$, are shown by the green lines in Figure 6.3. Correspondingly, we choose accreted subhalos with $z_{\rm peak}\sim 0.2,1,2,3$ and with the same $M_{\rm peak}$ ranges, plotted with the red lines. Note that the accreted halos at $z_{\rm peak}$ are members of the distinct halos at $z_{\rm i}=z_{\rm peak}$. And note that we are mainly interested in the difference of the distribution for the host halos and the accreted halos. The $z_{\rm f}$ distributions for the distinct halos show the existence of two components, but not as obvious as the to be accreted ones. At low $z_{\rm i}$, the hosts are rather old, with a tiny bump at the low $z_{\rm f}$ end, and the $z_{\rm f}$ distribution can be fitted by a log-normal distribution. As $z_{\rm i}$ becomes larger, the hosts are in general young, and a second younger component emerges. When $z_{\rm i}$ is larger than 3, the hosts are very young, and the distribution is dominated by one component which can be fitted by a log-normal distribution again. Comparing the

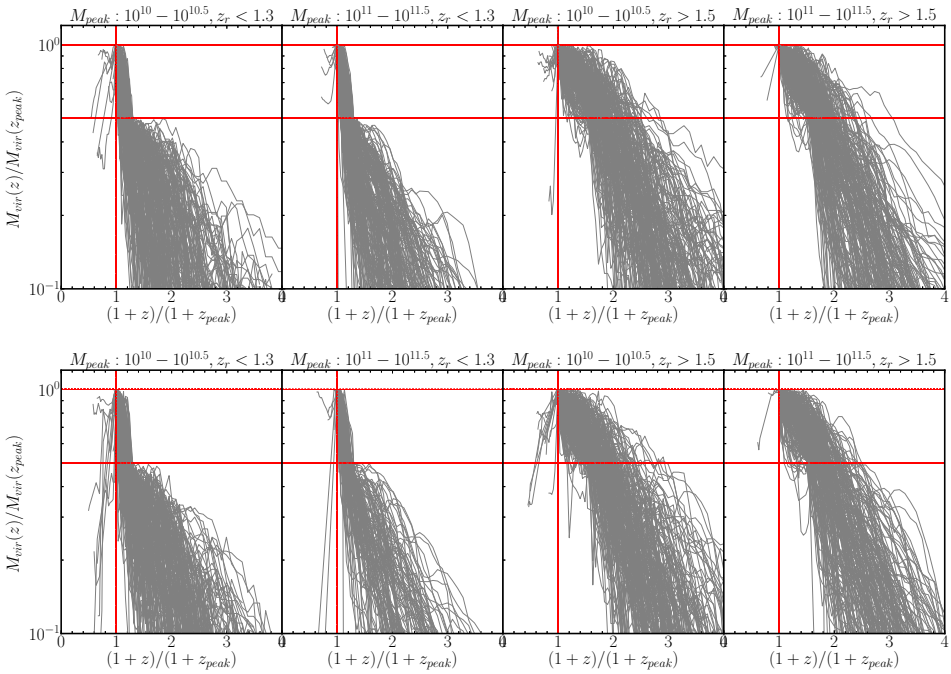

Figure 6.2: Mass accretion history for accreted subhalos. Define $z_{\rm r} = (1 + z_{\rm f})/(1 + z_{\rm peak})$, then subhalos with $z_{\rm r} < 1.3$ belong to the young population, and subhalos with $z_{\rm r} > 1.5$ belong to the old population. The upper panel is for $10^{12} < M_0 < 10^{13}\,h^{-1}{\rm M}_\odot$ and the lower panel is for $10^{13} < M_0 < 10^{14}\,h^{-1}{\rm M}_\odot$. Two subhalo mass ranges are chosen: $10^{10} - 10^{10.5}\,h^{-1}{\rm M}_\odot$ and $10^{11} - 10^{11.5}\,h^{-1}{\rm M}_\odot$, as indicated in the title of each panel. The two horizontal red lines mark the positions with redshifts corresponding to $z_{\rm peak}$ and $z_{\rm f}$.

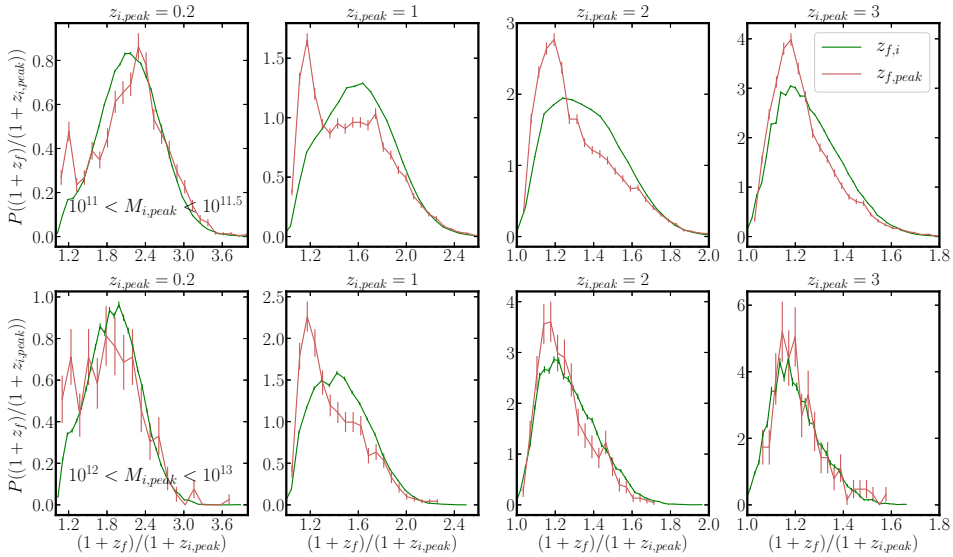

Figure 6.3: Formation redshift distribution of distinct halos with redshift $z_{\rm i} = 0.2, 1, 2, 3$, indicated by the green lines. The red lines are for subhalos accreted at $\langle z_{\rm peak}\rangle = 0.2, 1, 2, 3$. Upper panels are for small halos with $10^{11} < M_{\rm i} < 10^{11.5}\,h^{-1}{\rm M}_\odot$, and lower panels are for larger halos with $10^{12} < M_{\rm i} < 10^{13}\,h^{-1}{\rm M}_\odot$. The error bars are Poisson errors.

distribution of the hosts with the accreted subhalos, we found the peak positions of them roughly overlapping with each other. However, the bimodal feature is not as obvious as the accreted subhalos with $z_{\rm peak} = z_{\rm i}$, and the accreted halos have larger young population. This implies halos with different fate, i.e. being accreted or to be accreted later, have different MAH at a certain redshift.

6.2.1 Origin of the two populations

The above results can be understood if we consider them with the two phase accretion history of halos (Zhao et al., 2003a,b). Basically, Zhao et al. (2003a) found the average MAH of a halo at $z = 0$ follows a universal two phase MAH described by the formula:

$$\frac{M_{\rm vir}(z)}{M_{\rm vir}(z_{\rm tp})} = \frac{t^{0.3}}{1 - a + at^{-1.8a}}\ , \tag{6.1}$$

where $t \equiv \rho_{\rm vir}(z_{\rm tp})/\rho_{\rm vir}(z)$, $a = 0.75(0.42)$ for fast (slow) accretion phase and $z_{\rm tp}$ stands for the turning point. For more information on this formula, we refer the

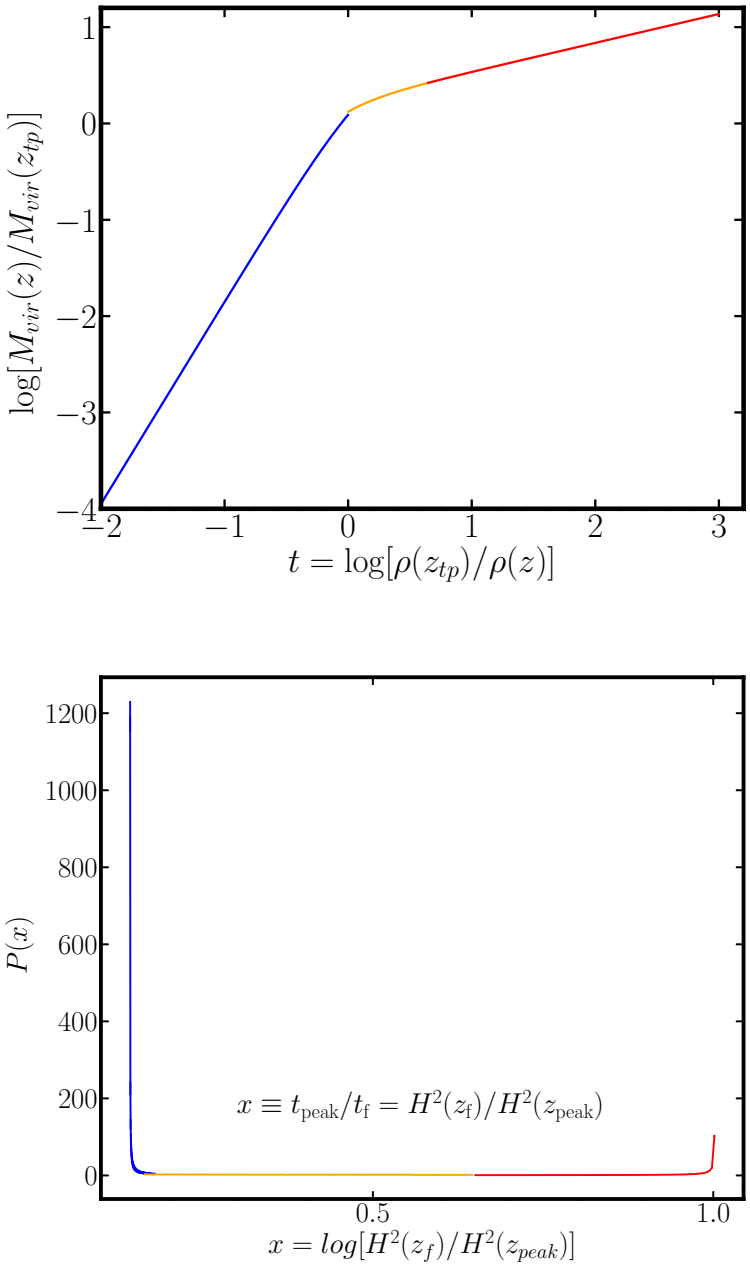

Figure 6.4: Upper: The average mass accretion history given by equation 6.1. The blue, orange, and red color indicate three possible phases a halo may lie on at accretion time $z_{\rm peak}$. Lower: The distribution of $\log x = \log[H^2(z_{\rm f})/H^2(z_{\rm peak})]$ for the three phases by evenly sampling along the x axis of the upper panel.

readers to Zhao et al. (2003a,b) for more details. This average MAH is plotted on the upper panel of Figure 6.4. If we take some values of t (with a corresponding $[M_{\rm vir}(z)]/[M_{\rm vir}(z_{\rm tp})]$), we can calculate the $t_{\rm f}$ corresponding to $[M_{\rm vir}(z)]/[2M_{\rm vir}(z_{\rm tp})]$. Thus we will have the resulting $\log x \equiv \log(t/t_f) = \log\left[H^2(z_{\rm f})/H^2(z_{\rm peak})\right]$ values, where $H^2(z) = \left[\Omega_\Lambda + \Omega_m(1+z)^3\right]$. The lower panel of Figure 6.4 is the distribution of $\log x$ by evenly sampling along $\rho_{\rm vir}(z_{\rm tp})/\rho_{\rm vir}(z)$. The simple calculation shows there are three general phases a halo might lie on when accretion happend, highlighted by the blue, orange, and red colors. For a halo gotten accreted when it is still at fast accretion phase (blue line), then the value of $\log x \equiv \log\left[\rho(z_{\rm f})/\rho(z_{\rm peak})\right] = \left[H^2(z_{\rm f})/H^2(z_{\rm peak})\right]$ peaks at around 0.14 (see the blue line in the lower panel). If a halo gotten accreted when it has just passed the fast accretion phase (orange line), then the corresponding possible value of $\log x = \log\left[H^2(z_{\rm f})/H^2(z_{\rm peak})\right]$ lies between 0.16 and 0.65. While for a halo gotten accreted when it has been slow accretion phase for a while (red line), the $\log x = \log\left[H^2(z_{\rm f})/H^2(z_{\rm peak})\right]$ peaks at around 1. In Figure 6.5 we re-plot the left panel of Figure 6.1 with the newly defined parameter $\log x = \log\left[H^2(z_{\rm f})/H^2(z_{\rm peak})\right]$. We found that the result is consistent with the expectation from the above naive/simple calculation. The young population peaks around $\log x \sim 0.2$, with the peak value decreasing with the decreasing $z_{\rm peak}$. The scatter might be due to the intrinsic variation of the MAH. The old population peaks in the range of ~ 0.3 to $\sim 1.$, showing they are contributed by the population that recently settle down on slow accretion phase (orange lines in the above figure) and the population that steadily settle down on slow accretion phase (red lines in the above figure). The contribution from the latter one increase with $z_{\rm peak}$. Again, taking the intrinsic variation of MAH into consideration, the scatter of $\log x$ can be explained.

By far, the physical origin of the bimodal feature is basically fully explained. At very high redshift, almost all halos are in fast accretion phase, with a quite young age when accreted. As the redshift decreases, more and more halos start to enter the slow accretion phase, with relatively old ages. However, there is still some halos in the fast accretion phase. At very low redshift, most halos are in the slow accretion phase, with quite old ages.

As discussed in Zhao et al. (2003a,b), the slow phase and fast phase accretion is tightly correlated with the halo concentration parameter c, with the slow accretion phase characterized by a nearly constant c and the fast accretion phase accompanied by a steadily increase of c with time. To verify further our two-phase accretion explanation for the bimodal $z_{\rm f}$ distribution. We plot $(1+z_{\rm f})/(1+z_{\rm peak})$ against $V_{\rm max}/V_{200}$ in Figure 6.6 for four chosen $z_{\rm peak}$ bins. The upper and lower 8 panels are for varying M_0 ranges, and the first/second rows are for varying $M_{\rm peak}$ ranges. Here we adopt the simple yet robust parameter $V_{\rm max}/V_{200}$ to characterize the concentration (Gao & White, 2007), where $V_{\rm max}$ is the peak value of the rotational velocity

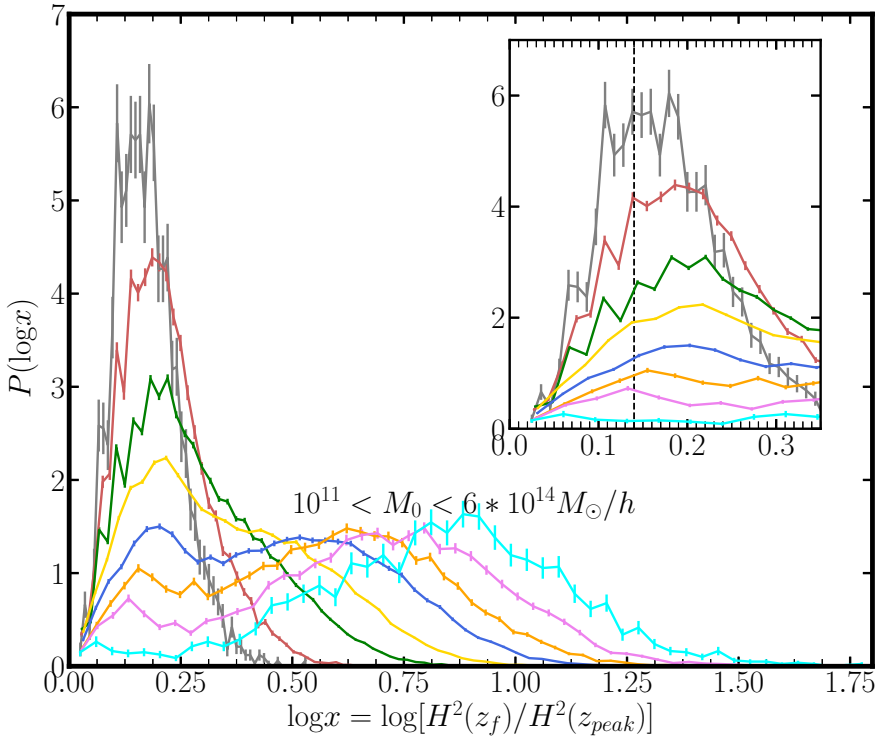

Figure 6.5: Similar as the left panel in Figure 6.1, except now it is the distribution of $logx = log\left[H^2(z_{\rm f})/H^2(z_{\rm peak})\right]$.

calculated with only particles bound to main subhalo, and $V_{200} = V_c(r_{200})$ is the circular velocity at the virial radius. Halos accreted at fast accretion phase (lower $(1+z_{\rm f})/(1+z_{\rm peak})$) tend to have relatively low concentration, while halos accreted at slow accretion phase (higher $(1+z_{\rm f})/(1+z_{\rm peak})$) tend to have higher concentration. The $z_{\rm f}$-c relation for accreted subhalos is consistent with our knowledge on the general $z_{\rm f}$-c relation for hosts. However, we did notice the relatively large scatter for the young population, especially when at high $z_{\rm peak}$.

6.2.2 Results with EPS merger trees

All previous calculation is done in the N-body simulation merger trees. However, merger trees generated with EPS formalism is also widely used in halo mass accretion history studies and early semi-analytic studies (Kauffmann & White, 1993; Parkinson, Cole & Helly, 2008; Sheth & Lemson, 1999; Jiang & van den Bosch, 2014). They have the advantage of being efficient, quick and free of resolution limit. It would be interesting to do the same measurements in the EPS merger trees. Using the merger tree building code developed by Parkinson, Cole & Helly (2008) and setting the same cosmology parameters as in the simulation, we generate thousands of merger trees for four host mass values: $10^{11.25}\,h^{-1}{\rm M}_\odot$, $10^{12.25}\,h^{-1}{\rm M}_\odot$, $10^{13.25}\,h^{-1}{\rm M}_\odot$, and $10^{14.25}\,h^{-1}{\rm M}_\odot$. Figure 6.7 shows the resulting distribution of $(1+z_{\rm f})/(1+z_{\rm peak})$ with similar $z_{\rm peak}$, M_0, and $M_{\rm peak}$ bins as in Figure 6.1. The bimodal feature is not existing in EPS merger trees. This either implies that current EPS merger tree generating formalism needs further improvements or there is some hidden numerical effects in the simulation that are not taken good care of.

6.3 Summary & discussion

In summary, we found a bimodal formation redshift distribution for the accreted subhalos, which naturally arises from the two phase accretion history of halos. Further test with EPS generated merger trees shows no bimodal feature at all.

Our results have important implications for galaxy formation. Halo assembly history is believed to correlate tightly with galaxy properties. For example, a key assumption in "age matching" model (Hearin & Watson, 2013; Hearin et al., 2014; Watson et al., 2015) is that at fixed stellar mass, the color/SFR of a galaxy is determined by the formation redshift of halo, which is verified in hydro-dynamical simulations (Bray et al., 2016). If we make the similar assumption that the halo age is correlated with the color/SFR of a galaxy, then our results imply some bimodal galaxy property distribution at position already even before post-accretion phase. However, galaxy formation is way more complicated and the key halo parameter

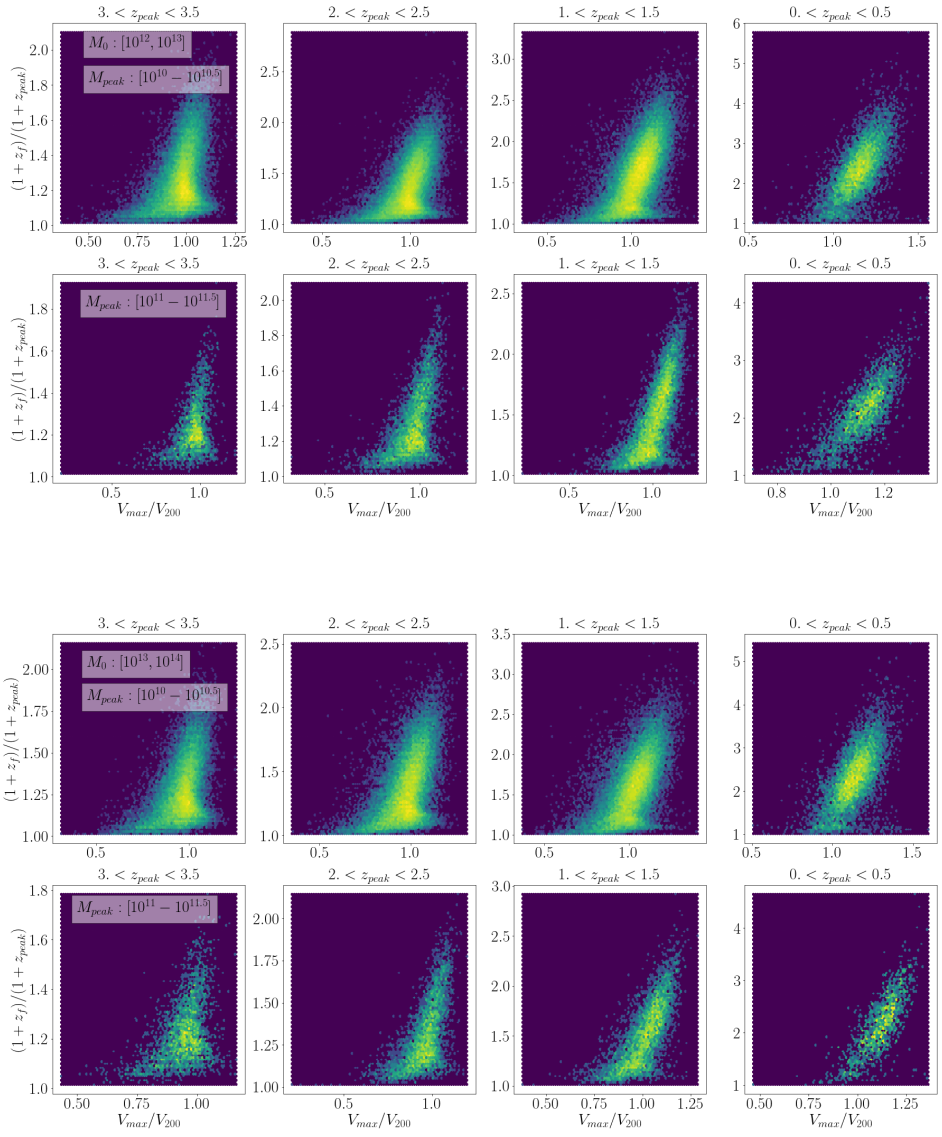

Figure 6.6: Concentration parameter (represented by $V_{\rm max}/V_{200}$) versus $(1+z_{\rm f})/(1+z_{\rm peak})$ for varying $z_{\rm peak}$ bins, as marked in the title of each panel. The above eight panels are for $10^{12} < M_0 < M^{13}\,h^{-1}{\rm M}_\odot$ and the lower eight panels are for $10^{13} < M_0 < M^{14}\,h^{-1}{\rm M}_\odot$. The first/third row is for small halos with $10^{10} < M_{\rm peak} < 10^{10.5}\,h^{-1}{\rm M}_\odot$, and second/forth row is for larger halos with $10^{11} < M_{\rm peak} < 10^{11.5}\,h^{-1}{\rm M}_\odot$.

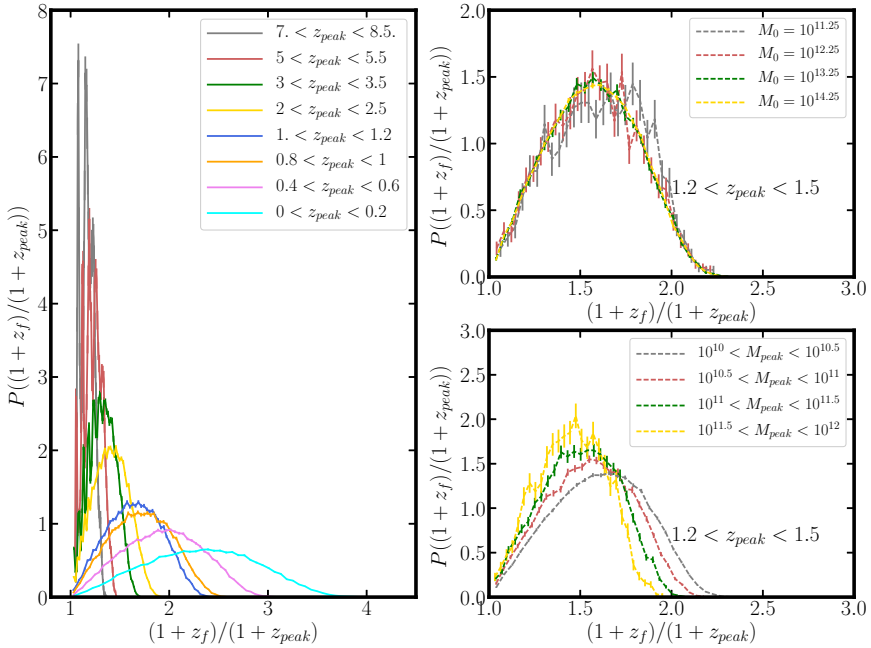

Figure 6.7: Same as Figure 6.1, but for subhalos on the merger trees generated with EPS formalism. Error bars are Poisson errors.

that is connected with the specific galaxy properties is still under debate. We don't want to over-interpret our results as finding the proof for the origin of the color bimodality from the dark side. Yet we stress that our results do imply the pre-accretion phase should be taken more good care of, i.e. not only $M_{\rm peak}$ and $z_{\rm peak}$ matters, but also $z_{\rm f}$ is important. It would be very interesting to study further the impact of the such halo formation redshift bimodality in shaping the observed color/SFR bimodality.

We also notice that in Hearin et al. (2014), they pronounced that they didn't found any bimodal feature for the halo age parameter they defined. We propose two main reasons for the non-detection. One is that they didn't slice the sample into accretion redshift bins, since the stack of the various $z_{\rm peak}$ bins may totally blur the bimodal feature. The other is that the definition of their formation redshift differs from ours in the sense that they define the formation redshift based on the concentration parameter, c (Wechsler et al., 2002). Their definition is meant to define $z_{\rm f}$ as the redshift when fast to slow accretion transition happens. However, at high z, more and more halos are lying on the fast accretion phase, with a constant c. $z_{\rm f}$ based on c thus won't be able to distinguish the halos lying in the fast accretion phase with same c yet different MAH. In fact, Hearin & Watson (2013) did mention that 10% of the population have a long high $z_{\rm f}$ tail. The success of "age matching" did prove the importance of formation redshift and accretion redshift (by definition, formation redshift is tightly correlated with $z_{\rm peak}$) are key parameters for galaxy formation, however ignoring the true bimodal distribution may miss some information.

An another interesting aspect is related with the satellite quenching. In some model, (e.g. the *delayed-then-rapid* model, see Wetzel, Tinker & Conroy (2012)), satellites are assumed to evolve as the centrals before accretion, with some further quenching mechanism functioning after accretion. First, our result suggest different assembly history of centrals and satellites even when they are not accreted yet (see Figure 6.3). Second, it also suggest both the pre-accretion and post-accretion phase should be considered with care when understanding the current satellite properties.

In summary, to characterize the assembly history of accreted subhalos, we emphasize the importance of three key parameters: $M_{\rm peak}$, $z_{\rm peak}$ and $z_{\rm f}$. And the successful model for satellites evolution need to consider either all of them or parameter combination that correlate with them. We hope our study may be helpful for understanding better the halo galaxy connection.

Part III:

Angular Momentum of Galaxies

Chapter 7

Angular Momentum in LTGs and ETGs

The relevance of the angular momentum issue in galaxy formation and evolution has been recently reassessed by Romanowsky & Fall (2012) and Fall & Romanowsky (2013), who critically reviewed previous results and pointed out the still-open problems and the main perspectives toward solving them.

In fact, the origin of angular momentum in galaxies has been hotly debated for a long times, well before the establishment of the modern CDM paradigm for structure formation. Hoyle (1949) first pointed out that the tidal field generated by an irregular matter distribution around a proto-galaxy may transfer to it a large amount of angular momentum. Such irregular distribution of matter is indeed expected to develop and operate as a consequence of gravitational instability (see Sciama 1955; Peebles 1969; Doroshkevich 1970; White 1984). This idea was then successfully applied to compute the angular momentum acquired by galactic DM halos in the context of the standard cosmological framework (e.g., Catelan & Theuns 1996).

On the observational side, Takase & Kinoshita (1967) and Freeman (1970) investigated the relationship between the total angular momentum $J_\star$ of the stellar disc and the stellar mass $M_\star$ for local spiral galaxies, finding a power-law behavior with a slope of $\approx 7/4$. Fall (1983) pointed out that a more relevant quantity is constituted by the specific angular momentum $j_\star = J_\star/M_\star$, given by the product of a length scale and a rotational velocity. He also showed that both spiral and elliptical galaxies follow a $j_\star$ versus $M_\star$ relation with similar slope ≈ 0.6, but with the former exhibiting systematically larger values of $j_\star$ by a factor of ≈ 5.

The angular momentum of spiral and elliptical galaxies, considered in connection with their structural properties and the angular momentum of their host DM halos, became and still remains a key aspect of galaxy formation and evolution (e.g. Efstathiou & Jones 1979, 1980; Davies et al. 1983; Mo, Mao & White 1998; van

den Bosch, Burkert & Swaters 2001; Dutton & van den Bosch 2012; Burkert et al. 2016; for a textbook, see Mo, van den Bosch & White 2010). Fall & Efstathiou (1980) discussed the origin of the rotational properties in disc galaxies within DM halos by comparing the expectations from the theoretical framework outlined by White & Rees (1978) to the available data.

The favored scenario for LTGs envisages that the specific angular momentum of the material forming the disc mirrors that of the host DM halo (see Fall & Efstathiou 1980; Fall 1983; Mo, Mao & White 1998). Such an assumption is indeed endorsed by the results of more recent numerical simulations (e.g., Governato et al. 2007; Zavala et al. 2016; Lagos et al. 2017). However, galaxy outflows and tidal stripping have also been advocated in order to rearrange the observed angular momentum in LTGs with different bulges over a total mass ratio B/T (see Maller & Dekel 2002; Sharma, Steinmetz & Bland-Hawthorn 2012; Brook et al. 2012; Dutton & van den Bosch 2012).

By contrast, the origin of the low angular momentum measured in ETGs is still open to debate, with a particular focus on the role of merging processes (e.g., Hopkins et al. 2009) versus disc instabilities (e.g., Shlosman & Noguchi 1993; Noguchi 1999; Immeli et al. 2004a,b; Bournaud, Elmegreen & Elmegreen 2007; for a review, see Bournaud 2016) as possible mechanisms to transfer and/or lose angular momentum.

An original approach to the issue of angular momentum in galaxy formation has been sketched by Eke, Efstathiou & Wright (2000) and Fall (2002), starting from the well known fact that only a fraction $f_{\rm inf}$ of the baryons associated with the DM halo are eventually found in the luminous components of galaxies, namely, stars, ISM, and dust (see Persic & Salucci 1992; Fukugita, Hogan & Peebles 1998). Then, it is reasonable to envisage that only the gas in the inner regions undergoes collapse and fuels star formation, while the outer portions of the galaxy are somehow refrained from forming stars. Since the specific angular momentum of the host DM halo decreases toward the inner regions (e.g., Bullock et al. 2001), the stars formed there should exhibit a lower $j_\star$. Romanowsky & Fall (2012) put forward this 'biased collapse' scenario and analyzed its merits and drawbacks.

In the present chapter, we show that the infall fraction $f_{\rm inf}$ that provides a quantitative description of the biased collapse scenario can be inferred from observations of the star-formation efficiency and chemical abundance of galaxies. The data indicate that the fraction $f_{\rm inf}$ is appreciably different for ETGs and LTGs, implying that the two galaxy types occupy distinct loci in the specific angular momentum versus stellar mass diagram. As a consequence, ETGs and LTGs are found to have retained in their stellar components a different fraction f_j of the angular momentum initially associated with the infalling baryons. We estimate such quantities and discuss how to physically interpret them in light of a a biased collapse plus merger scenario.

The plan of the chapter is as follows. After a brief presentation of the argument (Section 7.1), in Section 7.2, we show how to infer a robust estimate of the infalling gas fraction as a function of the stellar mass for both ETGs and LTGs by exploiting their observed star-formation efficiency and metal abundance. Section 7.3 is devoted to presenting and summarizing the available data on star-formation efficiency and metallicity in ETGs and LTGs. The infalling gas fraction and its impact on the specific angular momentum of both galaxy types are investigated in Section 7.4. In Section 7.5 we discuss our results and compare them with recent observational data and numerical simulations. Section 7.6 summarizes our key findings.

Throughout this work, we adopt the standard flat cosmology from Planck Collaboration et al. (2016) with round parameter values: matter density $\Omega_M = 0.31$, baryon density $\Omega_b = 0.05$, Hubble constant $H_0 = 100\,h$ km s^{-1} Mpc^{-1} with $h = 0.67$, and mass variance $\sigma_8 = 0.83$ on a scale of $8\,h^{-1}$ Mpc. Stellar masses and star formation rates (or luminosities) of galaxies are evaluated assuming the Chabrier (2003) IMF.

7.1 The initial specific angular momentum of inflowing gas

The galaxy angular momentum acquired by proto-galaxies is classically presented in terms of the dimensionless spin parameter

$$\lambda \equiv \frac{J\,|E|^{1/2}}{G\,M^{5/2}}, \tag{7.1}$$

which is a combination of basic galactic physical quantities, namely, the total angular momentum J, the total energy E, and the total mass M (DM and baryons; see Peebles 1969, 1971). The distribution of the spin parameter as a function of mass, redshift, and environment has been studied with both analytic approximations and numerical simulations (e.g., Barnes & Efstathiou 1987; Macciò et al. 2007; Bett et al. 2007; Rodríguez-Puebla et al. 2016). The emerging picture envisages that the halo spin parameter exhibits a lognormal distribution with average $\langle\lambda\rangle \approx 0.035$ and dispersion $\sigma_{\log\lambda} \approx 0.25$ (Rodríguez-Puebla et al., 2016), nearly independent of mass and redshift but somewhat dependent on environment (e.g., Bett et al. 2007; Macciò et al. 2007; Macciò, Dutton & van den Bosch 2008; Shi, Wang & Mo 2015). After Romanowsky & Fall (2012), we can define the specific angular momentum $j \equiv J/M$ of a spherically symmetric DM halo with mass distribution following a NFW profile (Navarro, Frenk & White 1996, 1997) extended out to the conventional virial radius $r_{\rm vir}$,

$$j(r_{\rm vir}) \approx 4.2\times10^4\lambda\left(\frac{M_{\rm vir}}{10^{12}\,M_\odot}\right)^{2/3} E(z)^{-1/6}\ {\rm km\,s^{-1}\,kpc}, \tag{7.2}$$

where $E(z) \equiv \Omega_\Lambda + \Omega_M\,(1+z)^3$. Note that the redshift dependence is weak; for instance, a halo at $z \approx 2$ features a momentum $j(r_{\rm vir})$ lower by a relatively small factor of ≈ 1.4 than that of a halo with the same mass at $z = 0$.

Barnes & Efstathiou (1987) and Bullock et al. (2001) pointed out via $N-$body simulations that the radial distribution of the halo specific angular momentum is well described by a power law with exponent $s \approx 1$, i.e.,

$$j(r) = j(r_{\rm vir}) \left[\frac{M(\leq r)}{M(\leq r_{\rm vir})} \right]^s \tag{7.3}$$

implying that the inner regions of halos exhibit a lower specific angular momentum than the outer ones. In Appendix B.2 we exploit state-of-the-art, high-resolution $N-$body simulations to derive the distribution of the parameter s as a function of mass and redshift (see also Figures. B.1 and B.2).

Next, we assume that the baryonic mass initially follows the same radial distribution of the DM with ratio $f_b \equiv M_b/M_{\rm vir} = \Omega_b/\Omega_M$; thus, the distributions of specific angular momentum for the baryonic gas $j_b(r)$ and the DM $j(r)$ mirrors each other, i.e., $j_b(r) = j(r)$. However, it could happen that only a fraction $f_{\rm inf}$ of the baryons associated with the galaxy halo are able to cool down and flow inward to reach the inner regions, where most of the star formation occurs. Then such baryons are expected to feature a specific angular momentum lower than $j_{\rm vir}$. More in detail, after equation (7.3) the fraction of baryons involved in the formation of the galaxy $f_{\rm inf} \equiv M_{\rm inf}/f_b\,M_{\rm vir} = M_b(\leq r_{\rm inf})/M_b(\leq r_{\rm vir}) \leq 1$ has an initial specific angular momentum

$$j_{\rm inf} = j(r_{\rm vir})\,f_{\rm inf}^s\,. \tag{7.4}$$

Note that this equation is very similar in spirit to equation (14) by Fall (1983), who advocated tidal stripping as a possible mechanism to prevent baryon in the outer regions of halos hosting ETGs collapse.

As we see below (Sections 7.3.1 and 7.3.3), the halo mass for galaxies endowed with stellar mass $M_\star$ can be estimated via various techniques. The outcome is usually expressed in terms of the star-formation efficiency $f_\star \equiv M_\star/f_b\,M_{\rm vir}$ as a function of the stellar mass $M_\star$. Plugging the definition of $f_\star$ into equations (7.2) and (7.4), we can write the intrinsic angular momentum of the inflowing gas as a function of the stellar mass and star-formation efficiency,

$$j_{\rm inf} \approx 3.1\times10^4\,\lambda\,f_\star^{-2/3} \left(\frac{M_\star}{10^{11}\,M_\odot}\right)^{2/3} f_{\rm inf}^s\,E(z)^{-1/6}\ {\rm km\,s^{-1}\,kpc}\,. \tag{7.5}$$

The above formula differs from equation (15) of Romanowsky & Fall (2012) in two respects: (i) we introduce the dependence on redshift (see also Burkert et al. 2016), and (ii) we focus on the specific angular momentum of the infalling gas. By

comparing the observed $j_\star$ to $j_{\rm inf}$, we aim to determine the fraction $f_j \equiv j_\star / j_{\rm inf}$ of the initial specific angular momentum retained by the stellar component (see Romanowsky & Fall 2012).

The next section is devoted to developing a method aimed at estimating the infalling baryon fraction $f_{\rm inf}$ from the observed star-formation efficiency and metal abundance for both ETGs and LTGs.

7.2 Fraction of inflowing gas from stellar efficiency and metal abundance

In the local universe, most of the baryonic mass within the central region (size $\lesssim 10-20$ kpc) of galaxies comprises three main components: stars, dust, and the ISM. An additional diffuse component of warm/hot gas, often dubbed the CGM (e.g., Tumlinson et al. 2011), pervades a much larger volume up to hundreds of kpc. These components descend from the diffuse gas of mass M_b associated with the galactic halo at the epoch of halo virialization. A portion (or all) of the gas cools down from the initial virial temperature, allowing star formation to occur (especially in clumpy regions) and chemical enrichment of the galactic components to proceed. A fraction of the cooled gas can eventually be expelled from the central regions by energy/momentum feedback associated with SN explosions/stellar winds and outbursts from the central active galactic nucleus (AGN). These feedbacks, depending on the history of star formation and AGN accretion, can be so efficient as to quench star formation and forbid further cooling of the hot/warm gas (see White & Frenk 1991; Bressan, Granato & Silva 1998; Cole et al. 2000). This is particularly true for AGNs, which are indeed expected to originate large-scale outflows (see Granato et al. 2004; Di Matteo, Springel & Hernquist 2005; Lapi et al. 2006). Statistical evidence of the latter can be recognized in the chemical enrichment of the intracluster medium (e.g., Leccardi, Rossetti & Molendi 2010; Böhringer 2014).

The total mass of the observed baryonic components, namely, the mass in stars $M_\star$ (including stellar remnants), ISM $M_{\rm ISM}$, dust $M_{\rm dust}$, and CGM $M_{\rm CGM}$ should not exceed the mass M_b of the baryons associated with the galaxy halo. On the other hand, the balance of the baryonic mass that cools and infalls toward the central regions $M_{\rm inf}$, the mass of the baryons still in the galaxy $M_{\rm gal}{=}M_\star{+}M_{\rm ISM}{+}M_{\rm dust}$, and the mass $M_{\rm out}$ of the gas expelled from the central regions by feedback mechanisms can be written as

$$M_{\rm gal} \equiv M_{\rm inf} - M_{\rm out} \; ; \tag{7.6}$$

note that the CGM does not enter the galaxy mass balance. As for the budget of metals, Fukugita & Peebles (2004) have shown that most of them are locked

up in compact objects, such as white dwarfs, neutron stars, and stellar mass BHs. However, here we are interested in the budget of metals produced by stars but not locked up in their compact remnants; we denote theses as *accessible* metals. Observations of stellar metallicity in galaxies essentially refer to that of main sequence stars after proper luminosity weighting.

In order to evaluate the accessible metals produced in a galaxy, a relevant quantity is constituted by the true metal yield y_Z of a single stellar population. Here we adopt the classic definition of y_Z that includes a normalization to $1-R$, where R is the return fraction of gaseous material from the formed stars (e.g., Vincenzo et al. 2016). In the following, we assume instantaneous recycling, but we have checked with detailed chemical evolution models that this is indeed a good approximation in our context (see also Feldmann 2015; Vincenzo et al. 2016). Note that y_Z depends on the assumed Chabrier IMF and mildly on the chemical composition of the stars. However, for our purposes, this is a second order effect, so we just exploit the average yields appropriate for reasonable chemical abundances (e.g. Peeples et al. 2014; Feldmann 2015; Vincenzo et al. 2016). Under these assumptions, the total mass of accessible metals produced by stars is then

$$M_Z = y_Z\, M_\star\ , \tag{7.7}$$

where $y_Z \approx 0.069$ applies for a Chabrier IMF (Krumholz & Dekel, 2012).

The budget of accessible metals inside the galaxy reads

$$M_{Z,\rm gal} = M_{Z,\star} + M_{Z,\rm ISM} + M_{Z,\rm dust} = \langle Z_\star\rangle\, M_\star + \langle Z_{\rm ISM}\rangle\, M_{\rm ISM} + M_{\rm dust}\ , \tag{7.8}$$

where we set $M_{Z,\star} = \langle Z_\star\rangle\, M_\star$, $M_{Z,\rm ISM} = \langle Z_{\rm ISM}\rangle\, M_{\rm ISM}$, and $M_{Z,\rm dust} = M_{\rm dust}$, i.e. $\langle Z_{\rm dust}\rangle = 1$. The metal mass conservation implies (see, e.g. Peeples et al. 2014)

$$M_Z = M_{Z,\rm gal} + M_{Z,\rm out}\ , \tag{7.9}$$

where $M_{Z,\rm out} = \langle Z_{\rm out}\rangle\, M_{\rm out}$ is the mass of metals expelled from the galaxy and disseminated in the CGM and IGM (see Peeples et al. 2014). The above equation assumes that (i) the cool gas inflowing from the galactic halo has a negligible metal content and (ii) outflowing mass and metals do not fall back at later times (i.e., no circulation due to a galactic fountain). We discuss in Appendix B.1 how relaxing such assumptions does not appreciably alter our results and conclusions.

Replacing $M_{Z,\rm gal}$ and $M_{\rm out}$ after equations (7.8) and (7.6), we get

$$y_Z\, M_\star = \langle Z_\star\rangle\, M_\star + \langle Z_{\rm ISM}\rangle\, M_{\rm ISM} + M_{\rm dust} + \langle Z_{\rm out}\rangle\, (M_{\rm inf} - M_\star - M_{\rm ISM} - M_{\rm dust})\ . \tag{7.10}$$

Then, we express the average metal abundance of the outflowing gas in terms of the stellar metallicity via the parameter $\zeta \equiv \langle Z_{\rm out}\rangle / \langle Z_\star\rangle$ and insert the star-formation efficiency $f_\star \equiv M_\star / f_b\, M_{\rm vir}$ and infall fraction $f_{\rm inf} \equiv M_{\rm inf} / f_b\, M_{\rm vir}$, to obtain

$$f_{\rm inf} = f_\star \left(\frac{y_Z}{\zeta\, \langle Z_\star\rangle} - \frac{M_{Z,\rm gal}}{\zeta\, \langle Z_\star\rangle\, M_\star} + \frac{M_{\rm gal}}{M_\star} \right)\ . \tag{7.11}$$

We can infer ζ from general arguments. In the case of feedback originated by stellar winds and supernova explosions, the outflow rate is proportional to the star formation rate $\dot{M}_{\rm out} \approx \epsilon_{\rm out}\,\dot{M}_\star$, where $\epsilon_{\rm out}$ is the mass loading factor. Then $M_{\rm out}(\tau) \approx \epsilon_{\rm out}\,M_\star(\tau)$ holds at any galactic age τ (e.g. Feldmann 2015), implying that both the stellar metallicity $Z_\star$ and the outflow metallicity $Z_{\rm out}$ can be computed as

$$Z_X(\tau) = \frac{1}{M_X(\tau)} \int_0^\tau {\rm d}\tau'\, Z_{\rm gas}(\tau')\,\dot{M}_X(\tau')\,, \tag{7.12}$$

with $X = \star$ or $X = {\rm out}$. As a consequence, the metallicity of the stars and of the outflows are quite close to each other, $Z_{\rm out}(\tau) \approx Z_\star(\tau)$. Therefore, for galaxies with outflows dominated by stellar feedback, e.g. LTGs, $\zeta \approx 1$ applies.

By contrast, the effect of the AGN feedback, relevant in the case of ETGs, can simply be described as an abrupt quenching of star formation, where most of the gas is assumed to be removed. If the feedback occurs at time $\tau_{\rm AGN}$, then the metallicity reads

$$Z_{\rm out} = \frac{M_{\rm Z,out}}{M_{\rm out}} = \frac{Z_\star(\tau_{\rm AGN})\,\epsilon_{\rm out} M_\star(\tau_{\rm AGN}) + Z_{\rm gas}(\tau_{\rm AGN})\,M_{\rm gas}(\tau_{\rm AGN})}{\epsilon_{\rm out}\,M_\star(\tau_{\rm AGN}) + M_{\rm gas}(\tau_{\rm AGN})}\,. \tag{7.13}$$

Since the gas metallicity $Z_{\rm gas}$ is increasing with time, equation (7.12) implies that the metal abundance of the stars is lower than that of the gas for small galactic age $\tau \ll 10^8$ yr, but they converge, $Z_{\rm gas}(\tau) \approx 1.1\,Z_\star(\tau)$, after a few 10^8yr. As a result, $Z_{\rm out} \approx Z_\star$ also holds in the case of AGN feedback. Summing up, we conclude that $\zeta \approx 1$ applies for both ETGs and LTGs.

7.3 Star Formation efficiency and metallicity of ETGs and LTGs

In this section, we examine the star formation efficiency (or equivalently, the stellar to halo mass ratio) and metal abundance in ETGs and LTGs.

The host halo mass of galaxies has been investigated by exploiting different observational approaches and theoretical assumptions; the more common techniques involve satellite kinematics, weak gravitational lensing, and abundance matching. Satellite kinematics and weak lensing offer the important opportunity to separately study ETGs and LTGs (e.g. More et al. 2011; Wojtak & Mamon 2013; Hudson et al. 2015; Velander et al. 2014; Mandelbaum et al. 2016). In particular, weak lensing has been exploited to investigate large samples of galaxies via stacking techniques, even at significant redshift $z \lesssim 0.7$ (e.g., Hudson et al. 2015). Abundance matching also provides insights on the galaxy-to-halo mass ratio at substantial redshift (e.g., Shankar et al. 2006; Moster, Naab & White 2013; Behroozi, Conroy & Wechsler

2010; Behroozi, Wechsler & Conroy 2013; Aversa et al. 2015; Huang et al. 2017a), although the separation between galaxy types is more challenging.

7.3.1 Star-formation efficiency of ETGs

In Figure 7.1 (top panel), we present the star-formation efficiency of ETGs as a function of their stellar mass for relatively local samples at $z \lesssim 0.3$. Data are from recent estimates based on satellite kinematics (More et al. 2011; Wojtak & Mamon 2013), weak lensing (Hudson et al. 2015; Velander et al. 2014; Mandelbaum et al. 2016), and abundance matching (Rodríguez-Puebla et al. 2015). Most data refer to the central/brightest red galaxy of a halo, possibly corrected for the contribution from satellites. This procedure is quite complex and can significantly contribute to the observed scatter of about 0.2 dex (see Behroozi, Wechsler & Conroy 2013; Reddick et al. 2013; Huang et al. 2017a), as shown by the red shaded area in the top panel of Figure 7.1.

Now we turn to the problem of estimating the star-formation efficiency at the reference redshift/epoch when most ($\gtrsim 70\%$) of the stars have been formed in the ETG progenitors. The notions that ETGs are quite old systems (formation redshift $z \gtrsim 1$) and that they formed in a relatively short timescale $\lesssim 1$ Gyr are time honored (e.g., Bower, Lucey & Ellis 1992; Thomas et al. 2005, 2010; for a review, see Renzini 2006). This is strongly supported by recent archeological studies on massive, passively evolving galaxies at substantial redshift $z \lesssim 1$, which show that they formed most of their stars at $z \sim 1.5 - 2$ (e.g. Trujillo, Ferreras & de La Rosa 2011; Onodera et al. 2015; Lonoce et al. 2015; Citro et al. 2016; Siudek et al. 2017; Kriek et al. 2016; Gallazzi et al. 2006, 2014; Choi et al. 2014; Glazebrook et al. 2017). Even lower mass ETGs formed mostly at $z \sim 1$, as pointed out by Siudek et al. (2017). We further notice that the cosmic stellar mass density increased by $\approx 40\%$ from $z \approx 1$ to the present (see Madau & Dickinson 2014; Aversa et al. 2015); this increase corresponds to the present-day fraction of stellar mass density contributed by disc dominated galaxies, including Sa (e.g., Moffett et al. 2015).

Investigations of the fraction of close galaxy pairs and galaxies with disturbed morphologies in large catalogs (e.g., Man, Zirm & Toft 2016) indicate that the mass growth of massive galaxies $M_\star \gtrsim 7 \times 10^{10}\, M_\odot$ is constrained within a factor of $\approx 1.5 - 2$ in the redshift interval $z \sim 0.1 - 2.5$. Limited mass evolution $\Delta \log M_\star \approx 0.16 \pm 0.04$ is also confirmed for a sample of quiescent galaxies at redshift $z \lesssim 1.6$ by Belli, Newman & Ellis (2014).

In the following, we assume for ETGs a reference formation (when $\gtrsim 70\%$ of the stars have been formed) redshift $z \approx 2$ and an average stellar mass increase of 50% since then. Because the stellar mass function at $z \approx 2$ is mainly dominated by the ETG progenitors, it's reasonable for us to exploit the abundance matching

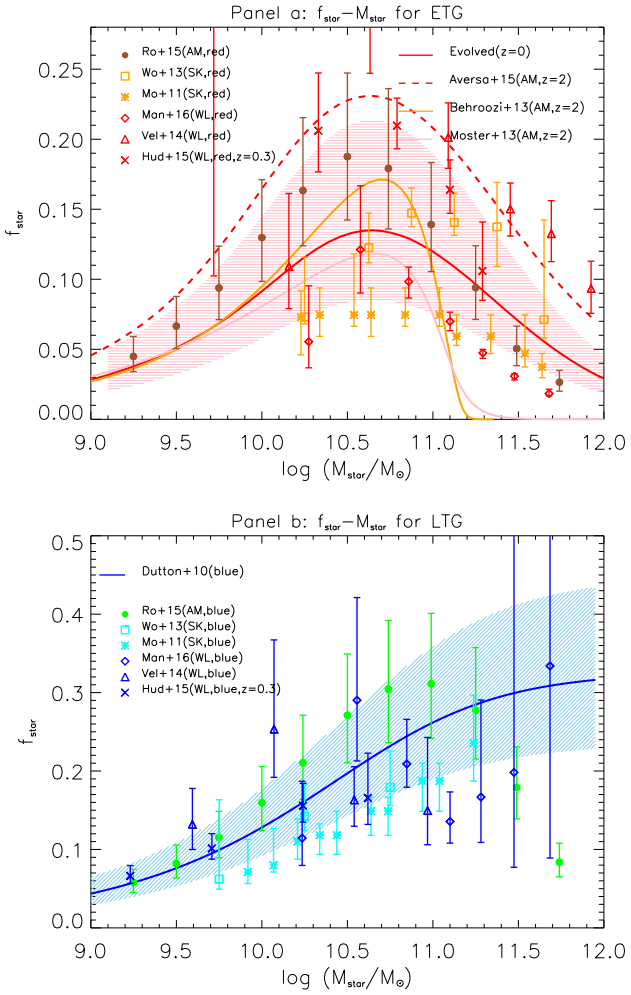

Figure 7.1: Star formation efficiency $f_\star$ versus stellar mass $M_\star$ for ETGs (top panel) and LTGs (bottom panel). Top panel: the red dashed line represents the relationship at $z = 2$ for ETGs inferred from Aversa et al. (2015) via the abundance matching technique, while the red solid line is the same relationship evolved to $z = 0$ (see details in Section 7.3.1), with the red shaded area showing the 1σ uncertainty. The orange and pink lines are the abundance matching results at $z = 2$ from Behroozi, Wechsler & Conroy (2013) and Moster, Naab & White (2013), respectively. Filled circles are the abundance matching data for red galaxies at $z = 0$ from Rodríguez-Puebla et al. (2015). Other datapoints are weak lensing or satellite kinematic measurements in the local universe from Wojtak & Mamon (2013), More et al. (2011), Mandelbaum et al. (2016), Velander et al. (2014) and Hudson et al. (2015) at $z = 0.3$. Bottom panel: the blue solid line represents the $f_\star$ versus $M_\star$ relation for LTGs from Dutton et al. (2010), with the blue shaded area indicating the 1σ uncertainty. Data are from the weak lensing and satellite kinematic observations cited above, but for blue galaxies.

technique applied to galaxies at $z \approx 2$ in order to derive an estimation of the star-formation efficiency in ETG progenitors.

In Figure 7.1 (top panel), we present the outcome of the abundance matching at $z \approx 2$ between the stellar and halo mass functions computed by Aversa et al. (2015). The results from Moster, Naab & White (2013) and Behroozi, Wechsler & Conroy (2013) are also shown for comparison. The resulting star-formation efficiencies differ by no more than a factor of 2. A relevant check on the efficiency can be done by comparing the estimate at $z \approx 2$ to the low redshift estimates based on weak lensing and satellite kinematics. Evolution in both halo and stellar mass must be taken into account. For the stellar mass change, we assume an increase of 50% as mentioned above.

The halo mass evolution has been computed via $N-$body simulations by McBride, Fakhouri & Ma (2009) and Fakhouri, Ma & Boylan-Kolchin (2010) and the excursion set approach by Lapi, Salucci & Danese (2013), with concordant results. The main progenitor of a present-day halo with virial mass $M_{\rm vir}$ evolves from $z \approx 2$ to the present as

$$M_{\rm vir}(z=0) \approx 4.0\, M_{\rm vir}(z=2) \left[\frac{M_{\rm vir}(z=0)}{10^{14}\, M_\odot}\right]^{0.12} . \tag{7.14}$$

The solid red line in Figure 7.1 shows how the star-formation efficiency estimated by Aversa et al. (2015) at $z \approx 2$ evolves toward $z \approx 0$ along the assumed evolutionary pattern for DM and stellar mass. The agreement with local data derived from weak gravitational lensing and satellite kinematics is good. We also checked that the proposed evolution is similar to that inferred by Hudson et al. (2015) for red galaxies with stellar mass $M \gtrsim 2 \times 10^{10}\, M_\odot$ (in our framework ETGs) between $z \approx 0.7$ and 0.3. Therefore, we adopt the estimation from Aversa et al. (2015) as the star formation efficiency for $z = 2$ ETG progenitors.

7.3.2 Metal abundance of ETGs

In order to derive the inflowing gas fraction $f_{\rm inf}$ from equation (7.11), not only the star-formation efficiency $f_\star$ but also the stellar metallicity $Z_\star$ at $z \approx 2$ is needed.

As for the stellar metallicity of ETGs, we adopt the relationship $Z_\star$ versus $M_\star$ proposed by Gallazzi et al. (2006) for a local $z \lesssim 0.2$ galaxy sample with its 1σ scatter of 0.12 dex (red line and red shaded area in the bottom panel of Figure 7.2). There is evidence that, after the main burst of star formation, the metal abundance of stars in ETGs stays practically constant (e.g., Citro et al. 2016; Gallazzi et al. 2014; Choi et al. 2014; Siudek et al. 2017), as confirmed from high redshift observations of passively evolving galaxies (see Lonoce et al. 2015; Kriek et al. 2016). Therefore, we reasonably assume that the present-day metallicity of

massive ETGs was already in place at redshift $z \approx 2$. For ETGs ,we also neglect both dust and the ISM in the mass and metals budget.

7.3.3 Star formation efficiency of LTGs

By comparing the panels of Figure 7.1, it is apparent that local LTGs exhibit a larger star-formation efficiency than ETGs. In particular, at high stellar masses, LTGs appear more efficient by a factor of $1.5 - 2$ (see Dutton et al. 2010; More et al. 2011; Wojtak & Mamon 2013; Velander et al. 2014; Rodríguez-Puebla et al. 2015; Mandelbaum et al. 2016). Despite the large scatter of the data, a higher efficiency for LTGs is found from several samples, independent of whether the halo mass is derived via abundance matching or weak lensing. In the bottom panel of Figure 7.1 we illustrate the fit to the data by Dutton et al. (2010), with its associated 1σ uncertainty, shown by the blue shaded area.

At variance with ETGs, Hudson et al. (2015) showed that the relationship between efficiency and stellar mass does not appreciably evolve between $z \approx 0.7$ and 0.3. A straightforward interpretation is that, in LTGs, the star formation and DM accretion are parallel along cosmic times. In the following, we assume that the star-formation efficiency versus stellar mass relationship in LTGs stays almost constant, close to the present-day value, along the period of disc formation.

7.3.4 Metal abundance of LTGs

In the case of LTGs, the mass in the ISM and dust is no more negligible and, as a consequence, they can contribute significantly to the global galaxy metal abundance. The amount of stars, ISM, and dust and their metal abundance have been presented by Peeples et al. (2014). We adopt their relationships with the associated scatter and defer the reader to their paper for details. Note that the stellar metallicity measurements still retain an appreciable uncertainty (Gallazzi et al. 2005; Goddard et al. 2017), especially for low mass LTGs (cf. bottom panel of Figure 7.2). Another caveat concerns the metal mass in the ISM, which includes only cold gas in the analysis of Peeples et al. (2014); the mass and metals in warm ionized gas could be as large as those in the cold gas (see Sembach et al. 2000; Haffner et al. 2009; Peeples et al. 2014). We checked that doubling the ISM mass and metals only marginally affects our results; e.g., the infall fraction $f_{\rm inf}$ (cf. Section 7.4) changes by no more than 10%.

We recall that LTGs are still forming stars in their discs, at exponentially declining rates (e.g., Chiappini, Matteucci & Gratton 1997). This implies that the metallicity increases along cosmic times; the median increases from $z \approx 0.7$ to the present has been estimated by Gallazzi et al. (2014) to be $\lesssim 0.12$ dex, which

is comparable to the uncertainties in the metallicity estimates (see Gallazzi et al. 2005; Peeples et al. 2014).

7.4 Estimated fraction of inflowing gas and specific angular momentum

Figure 7.2 shows that ETGs and LTGs occupy different loci in the $f_\star$ versus $Z_\star$ plane. At a given metallicity the efficiency is higher for LTGs; by contrast, ETGs feature higher metallicity even if the efficiency is small. These observational results directly impact the fraction $f_{\rm inf}$ of gas flowing into the central regions (cf. equation (7.11)).

In Figure 7.3 the fraction $f_{\rm inf}$ is plotted against the stellar mass; the shaded areas reflect the uncertainties in chemical abundance and stellar efficiency. In the case of LTGs, the resulting fraction $f_{\rm inf} \approx 0.9 - 1.3$ is very close to 1, except in a limited mass range $M_\star \sim 3 - 10 \times 10^9\, M_\odot$, wherein a maximum value of ≈ 1.7 is reached; however, $f_{\rm inf} \lesssim 1$ is allowed at the 1σ level.

For ETGs, the resulting infall fraction reaches a maximum $f_{\rm inf} \approx 0.7$ around $M_\star \approx 3 \times 10^{10}\, M_\odot$ and then declines at larger masses due to the combined decrease in efficiency and increase in metallicity, as shown in Figure 7.2. However, an infall fraction constant with mass $f_{\rm inf} \approx 0.3 - 0.4$ is allowed at 1σ.

Interestingly, the fraction of the inflowing gas that is then removed by feedback $M_{\rm out}/M_{\rm inf}$ is always larger than 70% for LTGs, while it is substantially lower for ETGs (dashed lines in top panel of Figure 7.4). By contrast, the fraction of inflowing mass eventually retained into stars $M_\star/M_{\rm inf}$ is larger for ETGs, reaching 60% (solid lines in top panel of Figure 7.4). This reflects the dilution needed for LTGs to keep the stellar metallicity low even in the presence of a higher star-formation efficiency.

The bottom panel in Figure 7.4 shows that only a small fraction of metals produced by stars are retained within the galaxy (i.e., in stars, ISM, and dust). We exclude the CGM from the budget because it does not enter into the galaxy mass and metal balances, though its composition carries some relevant information on complex inflow/outflow processes (see Peeples et al. 2014). For LTGs, such a fraction is $\approx 20 - 30\%$ almost constant with stellar mass, as found by Peeples et al. (2014) for a large sample of spiral galaxies. By contrast, for ETGs, we find that the fraction is increasing with stellar mass, reaching $\approx 60\%$.

In Figure 7.5 (top panel), we illustrate the relation between specific angular momentum and stellar mass predicted after equation (7.5) for LTGs and ETGs; this constitutes our main result. The differences in the inflowing fraction $f_{\rm inf}$, the efficiencies $f_\star$, and the formation redshift cooperate to yield distinct loci in

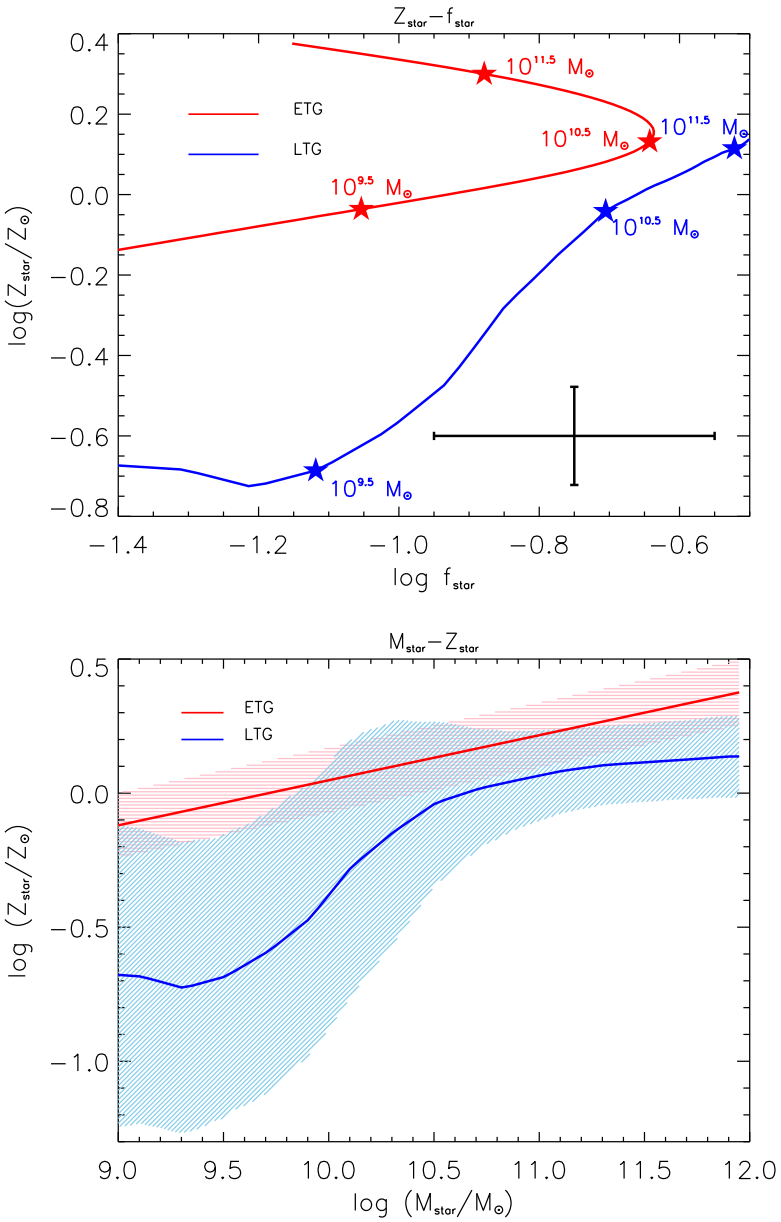

Figure 7.2: Top panel: stellar metallicity $Z_\star$ (in units of the solar value $Z_\odot$ = 0.015) plotted against star-formation efficiency $f_\star$ for ETGs (red) and LTGs (blue). The stars highlight the positions on the curves for galaxies with stellar masses $M_\star \approx 10^{9.5} - 10^{10.5} - 10^{11.5}\, M_\odot$. The error bars in the bottom right corner indicate the typical uncertainty in the measurements of $Z_\star$ and $f_\star$. Bottom panel: stellar metallicity $Z_\star$ versus $M_\star$ for ETGs (red) and LTGs (blue), taken from Gallazzi et al. (2005) and Gallazzi et al. (2006). The red and blue shaded areas show the 1σ uncertainty.

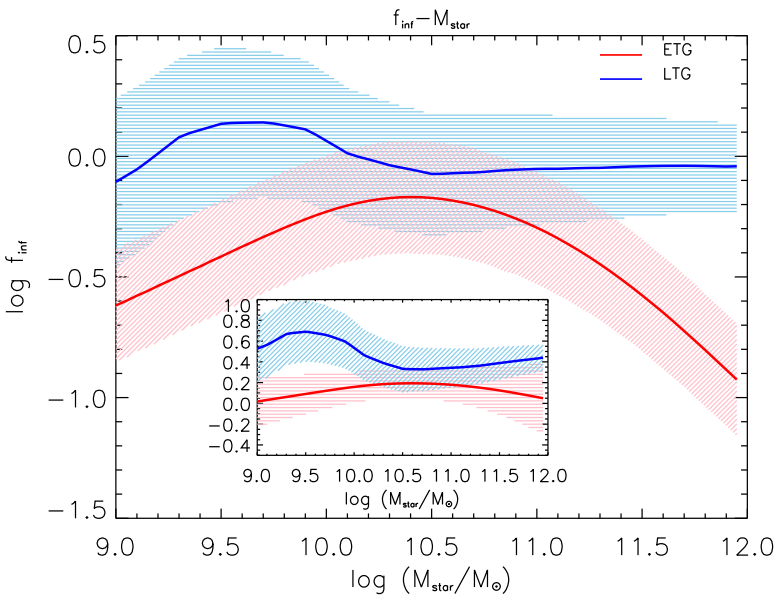

Figure 7.3: Inferred baryon infalling fraction $f_{\rm inf}$ for ETGs (red) and LTGs (blue). The shaded areas indicate the 1σ uncertainty calculated by taking into account the scatter of the parameters entering equation (7.11). In the inset, we plot for ETGs and LTGs the quantity $y_Z\, f_\star^{-2/3+s}\, Z_\star^{-s}\, M_\star^{0.15}$ together with its 1σ uncertainty (shaded areas; see text for details).

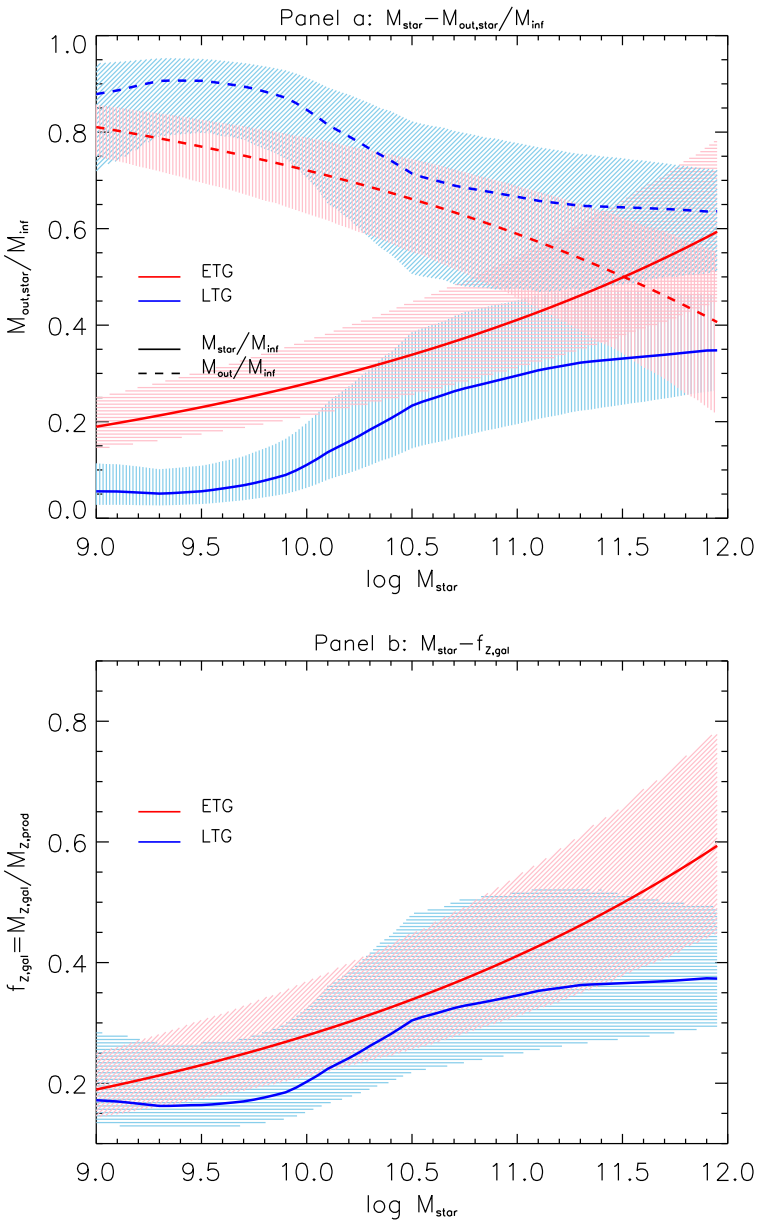

Figure 7.4: Top panel: stellar mass fraction $M_\star/M_{\rm inf}$ (solid lines) and ejected mass fraction $M_{\rm out}/M_{\rm inf}$ (dashed lines) for ETGs (red) and LTGs (blue). Bottom panel: fraction of metals retained in galaxies $f_{\rm Z,gal} \equiv M_{\rm Z,gal}/M_{\rm Z,prod}$. The shaded areas explicitly show the 1σ uncertainties of the estimates.

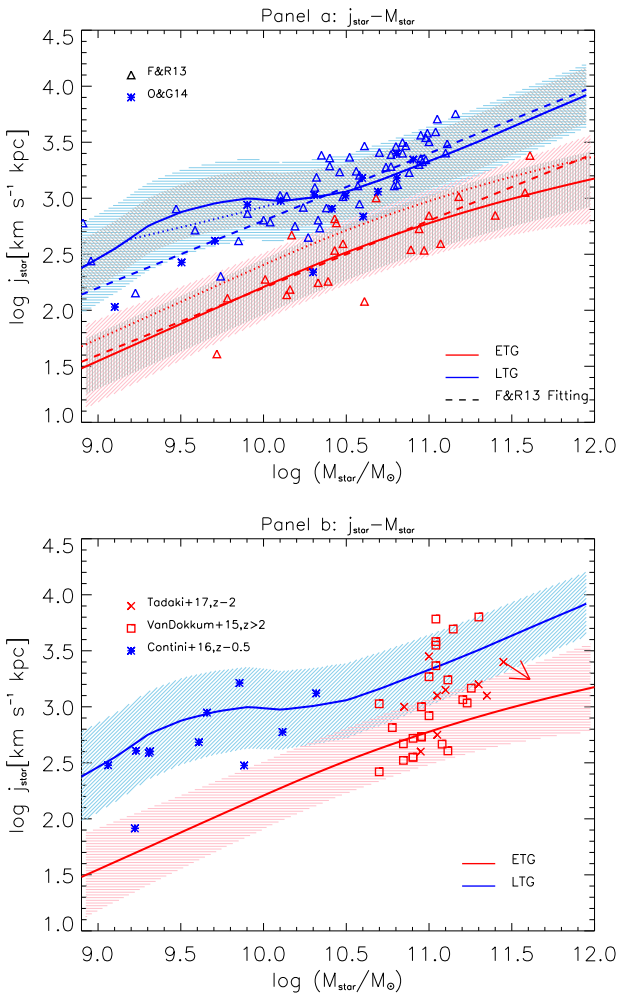

Figure 7.5: Specific angular momentum $j_\star$ versus the stellar mass $M_\star$ for ETGs (red lines) and LTGs (blue lines). Blue solid line is the result for LTGs with a retention fraction $f_j \approx 1$; dotted blue line applies when limiting the infall fraction $f_{\rm inf} \leq 1$. Red solid line is the result for ETGs taking into account stellar mass growth by dry mergers and a retention fraction $f_j \approx 0.64$; red dotted line refer to $f_j \approx 1$. In the top panel dashed lines represent the fitting formula $j_\star \propto M_\star^{0.6}$ adopted by Fall & Romanowsky (2013). The colored shaded areas indicate the 1σ uncertainty calculated by taking into account the variances of the parameters entering in equation (7.5), while the grey shaded area includes only the intrinsic variance in the halo spin parameter λ measured from numerical simulations. The blue and red triangles are data from Fall & Romanowsky (2013) for LTGs and ETGs, respectively. The blue stars are data for local spiral galaxies from Obreschkow & Glazebrook (2014). In the bottom panel data for star-forming compact galaxies at $z \approx 2$ are reported: red squares are from van Dokkum et al. (2015) and red crosses from Tadaki et al. (2017); data for disk galaxies at $z \approx 0.5$ from Contini et al. (2016) are also shown as blue stars. The red arrow shows explicitly the expected evolving direction of the high-z ETG progenitors, after considering the growth in stellar mass envisaged by Belli, Newman & Ellis (2014) and $f_j = 0.64$.

the angular momentum versus stellar mass plane for the two galaxy types (cf. equation (7.5)). To highlight the relevant dependencies, it is worth noticing that the handy approximation $f_{\rm inf} \approx y_Z\, f_\star / \langle Z_\star \rangle$ holds for both galaxy types. By plugging it into equation (7.5), the specific angular momentum is seen to scale as

$$j_\star \propto \lambda\, f_j\, f_\star^{-2/3+s}\, Z_\star^{-s}\, M_\star^{2/3}\ ; \tag{7.15}$$

where λ is independent of the host halo mass and is assumed not to introduce additional dependence on the stellar mass. The inset of Figure 7.3 shows that the product $y_Z\, f_\star^{-2/3+s}\, Z_\star^{-s}\, M_\star^{0.15} \approx$ const. is different in normalization for each galaxy type but nearly independent of $M_\star$ for both (within the 1σ uncertainty). Since $s \sim 1$ the scaling $j_\star \propto f_\star^{1/3}$ applies; hence, the uncertainty in $f_\star$ only marginally contributes to that in $j_\star$.

Our result for LTGs (blue solid lines) well describes the observed $j_\star$ versus $M_\star$ relationship of discs. Note that we allow for $f_{\rm inf} \gtrsim 1$, but we also plot (blue dotted line) the specific angular momentum under the condition $f_{\rm inf} \lesssim 1$; as expected, the estimates are within the respective 1σ uncertainties. Our result for $j_\star$ for LTGs implies a full retention of the initial specific angular momentum, i.e., $f_j \approx 1$. More quantitatively, a Monte carlo fitting that takes into account uncertainties in the metallicities, $f_\star$ and $j_\star$, yields $f_j = 1.11^{+0.75}_{-0.44}$. This is consistent within 1σ with the value around 0.8 found by Fall & Romanowsky (2013).

For ETGs, the specific angular momentum (red dotted line) has been computed by using the efficiency at $z \approx 2$ and assuming an absence of evolution in the metal abundance (see Section 7.3.1 and 7.3.2). In addition, a shift in stellar mass by a factor of 1.5 has been applied to take into account mass additions by dry mergers at late times (red solid lines; see Section 7.3.1). Comparison with local data for passive galaxies highlights that some room remains for a possible decrease of the specific angular momentum. Monte carlo model fitting that takes into account uncertainties in $Z_\star$, $f_\star$, and $j_\star$ yields $f_j = 0.64^{+0.20}_{-0.16}$. The average value may be explained by dry mergers at late times. For instance, if at later epochs the mass of the ETG progenitors is increased because of minor dry mergers with satellite galaxies (e.g., Naab, Johansson & Ostriker 2009; Belli, Newman & Ellis 2014), then a small decrease of the specific angular momentum can occur. The extent of this decrease is related to the sum of the initial momentum of the two companion galaxies and their orbital momentum. For a limited mass increase of a factor 1.5, a small decrease $j_\star \gtrsim 1/1.5 \approx 0.67\, j_{\rm inf}$ is expected, since the randomly oriented angular momentum of the companions partially cancels out (see also Romanowsky & Fall 2012). Note that a value $f_j \lesssim 0.1$, which would be needed to obtain the angular momentum of ETGs from the typical values for LTGs (and for the host halos), is excluded to more than 3σ.

The colored shaded areas in Figure 7.5 represent the 1σ uncertainty in $j_\star$, which includes the uncertainties in $f_\star$ and metallicity and the intrinsic variance in

the exponent s (see shaded areas in Figure 7.3) and spin parameter λ; the variance in λ actually dominates the overall scatter, as highlighted by the grey areas.

Focusing on the slope of the $j_\star - M_\star$ relation, Romanowsky & Fall (2012) suggested that it can deviate from the expected value of 2/3, which stems from the definition $M_{\rm vir} = M_\star / f_\star\, f_b$ and from equation (7.2); see also Catelan & Theuns (1996). Our results in Figure 7.5 feature a running slope flatter than but close to 2/3; specifically, by forcing a single power-law fitting, we get $j_\star \propto M_\star^{0.5}$ for LTGs and $j_\star \propto M_\star^{0.6}$ for ETGs. Interestingly, Fall & Romanowsky (2013) found a slope of around 0.6 for both, as indicated in Figure 7.5 (top panel) by the dashed lines.

To sum up, for LTGs, the observed metallicity and star-formation efficiency imply that the fraction of the available baryons fueling star formation must be close to unity, $f_{\rm inf} \approx 1$. Moreover, the specific angular momentum very well reproduces observations with a retention factor $f_j \approx 1$. By contrast, for ETGs, observations indicate that only a fraction $f_{\rm inf} \approx 0.4$ of the initial baryonic mass $f_b\, M_{\rm vir}$ must feed star formation; such a fraction of gas is endowed with low specific angular momentum, which turns out to be close to that observed for the stellar component in local passive galaxies. The data leave room for a small decrease $f_j \approx 0.64$ of specific angular momentum due to dry mergers possibly occurring between $z \lesssim 1$ and the present time. Since we find for both galaxy types that the product $f_\star^{-2/3+s}\, Z_\star^{-s}$ only weakly depends on $M_\star$, the slope of the $j_\star$ versus $M_\star$ relationship is close to 2/3, as observed for both galaxy types.

7.5 Discussion

In their thoughtful paper, Romanowsky & Fall (2012) reviewed the three most likely explanations for the observed location of ETGs and LTGs in the $j_\star$ versus $M_\star$ plane: (i) outflows of gas by some feedback mechanism or tidal stripping of the galactic halo, (ii) biased collapse plus merger scenario, and (iii) pure merger driven evolution of LTGs into ETGs.

We have shown that current data on the star-formation efficiency and stellar metallicity naturally imply different infalling gas fractions for LTGs and ETGs, with average values of $f_{\rm inf} \approx 1$ and 0.4, respectively. These results strongly favor the biased collapse plus merger scenario, and they naturally locate ETGs and LTGs in two distinct loci of the $j_\star$ versus $M_\star$ plane (cf. Figure 7.5). While such a scenario is likely not the unique explanation for the observed $j_\star$ versus $M_\star$ relationships in ETGs and LTGs, it points out the possibility that the history of star formation, and hence $f_\star$ and $Z_\star$, knows about the assembly of the host DM halos and their angular momentum. Below, we compare the predictions of the biased collapse plus mergers scenario to additional observational data and numerical simulations.

7.5.1 The case of LTGs

For LTGs, we infer $f_{\rm inf} \approx 1$ and show that this value reproduces the observed $j_\star$ versus $M_\star$ relationship, implying full retention of the specific angular momentum $f_j \approx 1$. Such results are in line with the main assumption of the classical framework for disc formation, namely, that discs keep the overall specific angular momentum of their hosting halos (see Fall & Efstathiou 1980; Mo, Mao & White 1998; Mo & Mao 2004; van den Bosch et al. 2002). A slow assembly of LTG discs is supported by the results of Hudson et al. (2015), which showed that the ratio of the star to the halo mass $M_\star/M_{\rm vir}$ stays constant over a long cosmological timescale (from $z \approx 0.7$ to 0.3); this is the crucial epoch for disc formation, as suggested by classical results on chemical and photometric evolution (see Pezzulli & Fraternali 2016). Accurate spectrography for large samples of $z \approx 1$ star-forming galaxies shows that rotationally dominated systems exhibit a specific angular momentum that is lower by factors of $1.5 - 2$ than those of local LTGs with the same stellar mass (see Harrison et al. 2017; Swinbank et al. 2017). However, Contini et al. (2016) presented evidence that LTGs at moderately low $z \sim 0.5$ fall on the local $j_\star$ versus $M_\star$ relationship within 1σ; this possibly suggests rather weak dependence on the redshift, such as $E(z)^{-1/6}$, (cf. equation (7.5); see also Burkert et al. (2016).

The evolution of the angular momentum in galaxies has also been analyzed in Genel et al. (2015) by exploiting the results of the *Illustris* cosmological simulation (see Vogelsberger et al. 2014a,c; Genel et al. 2014; DeFelippis et al. 2017) and in Sokołowska et al. (2017) using zoom-in simulation for MW like galaxies. These authors find that local LTGs retain 100% of the specific angular momentum of their parent halos, likely due to enforced specific recipes for feedback and/or metal recycling. Their conclusion is confirmed by the analyses of Zavala et al. (2016) and Lagos et al. (2017) based on the *EAGLE* numerical simulation (see also Schaye et al. 2015).

All in all, current observations and simulations indicate that feedback mechanisms (stellar winds, SN explosions and possibly AGNs) and ISM physics must cooperate to remove material from the galaxy star-forming regions, while cooling processes replace it with metal poor, high specific angular momentum gas; the overall outcome is that the metal content in star-forming regions is diluted and kept to low levels, while the specific angular momentum of the disc is increased. All of this occurs on cosmological timescales of order of many Gyr (see Mollá et al. 2016).

7.5.2 The case of ETGs

Romanowsky & Fall (2012) pointed out that the biased collapse scenario should be carefully considered in the case of ETGs, which apparently underwent angular

momentum loss. Their main reservation toward biased collapse stems from a constraint on the normalization of the stellar specific angular momentum, which scales as $j_\star \propto f_j\, f_\star^{-2/3}$ under the assumption that the relation $j_{\rm vir} \propto M_{\rm vir}^{2/3}$ expected for DM halos (see Catelan & Theuns 1996) transfers to $j_\star \propto M_\star^{2/3}$ for the stellar component. As a consequence, the normalization of the correlation $j_\star$ versus $M_\star$ is constrained to be $f_j\, f_\star^{-2/3} \approx 0.5$ (cf. equations (15) and (16) in Romanowsky & Fall 2012). For ETGs, they adopted the fitting formula of $f_\star$- $M_\star$ from Dutton et al. (2010), obtaining $f_j \approx 0.1$.

By contrast, we demonstrated that the chemistry and star-formation efficiency of ETGs imply a small fraction of infalling gas mass $f_{\rm inf} \approx 0.4$. This parameter just quantifies the amount of biased collapse and naturally decreases the normalization of $j_\star$ by a factor of ≈ 2.5 (since $j_\star \propto f_j\, f_\star^{-2/3}\, f_{\rm inf}^{s}$ with $s \approx 1$). We have shown that a retention fraction $f_j \approx 0.64$ is needed to reproduce observations; this can be accommodated by late-time dry mergers in terms of mass addition $\Delta M_\star / M_\star \lesssim 0.5$.

One of the most relevant predictions of the biased collapse scenario is that the specific angular momentum has been imprinted in the ETG progenitors since the very beginning, with only minor changes related to later evolution in mass and size. This prediction can be tested by computing the angular momentum of the high-z candidate progenitors of ETGs. Among the observed candidates, there are 25 compact star-forming galaxies at $z \approx 2$ that have been studied in detail by van Dokkum et al. (2015). In particular, the observed structural and kinematical data of this optically selected sample allow us to estimate the specific angular momentum of the galaxies by exploiting the approximation of Romanowsky & Fall (2012), $j \approx k_n\, V_{\rm rot}\, R_e$, where n is the Sérsic (1963) index. The median values for the sample are $n \approx 4$ ($k_4 \approx 2.3$), $r_e \approx 1.4$ kpc, and $V_{\rm rot} \approx 340$ km s^{-1}, yielding a median value of $j \approx 1000$ km s^{-1} kpc, very close to that observed in local ETGs endowed with a similar stellar mass of $M_\star \approx 10^{11}\, M_\odot$. Figure 7.5 (bottom panel) illustrates in detail that 18 out of 25 galaxies (70% of the sample) fall within 1σ of the the $j_\star$ versus $M_\star$ relationship of local ETGs.

Tadaki et al. (2017) presented estimates of the specific angular momentum for the nine optically selected star-forming galaxies at $z \approx 2$ observed with ALMA and detected at 870 μm. In Figure 7.5 (bottom panel), these galaxies are shown to exhibit a distribution in the $j_\star$ versus $M_\star$ plane similar to that of the galaxies observed by van Dokkum et al. (2015). These results suggest that most of these galaxies are in fact the progenitors of the local ETGs and that their specific angular momentum is imprinted at the epoch of formation with only minor subsequent changes, as predicted by our scenario. We stress the importance of analyzing larger galaxy samples in order to further test this conclusion.

It is also interesting to compare these observational findings to the outcomes

of recent numerical simulations, such as *Illustris* (see Vogelsberger et al. 2014a,c; Genel et al. 2014, 2015). As for LTGs, Genel et al. (2015) found in the simulation a $j_\star$ versus $M_\star$ relation similar to the observed local one. For ETGs, the situation is more complex. For a fraction of galaxies, namely, those galaxies with high final values of $j_\star$, the evolution is quite similar to that of LTGs. By contrast, for simulated ETGs with low final values of $j_\star$, Genel et al. (2015) envisaged two evolutionary paths: (i) a rapid initial growth in specific angular momentum combined with a later robust increase in mass by a factor of ~ 10 and roughly no change in specific angular momentum, and (ii) a sudden drop of the specific angular momentum mainly imposed by a major merger. These authors also found that radio-mode feedback from AGNs helps in reducing the angular momentum, particularly for high mass galaxies. In fact, while analyzing the *EAGLE* simulation (see Schaye et al. 2015), Lagos et al. (2017) put forward the possibility that even early star formation followed by a rapid quenching can be effective in producing low angular momentum galaxies.

All in all, the analyses of simulated ETGs by Zavala et al. (2016) and Lagos et al. (2017) support a strong relation between the specific angular momentum of the stars and DM in the inner star-forming region. Future data on the specific angular momentum of massive high-z galaxies will provide a crucial test for this scenario and a robust benchmark for next-generation numerical simulations of galaxy formation.

In the biased collapse scenario, the feedbacks (stellar and AGN) are key processes, since they partially offset cooling and regulate the fraction of inflowing gas. More specifically, in the case of ETGs, AGN feedback is required in order to stop the gas inflow. This yields a high stellar metallicity and a pronounced α enhancement (see Matteucci 1994; Romano et al. 2002; Thomas et al. 2005) and keeps the specific angular momentum low. The relationships between central BH mass, stellar mass, and velocity dispersion can also be explained in this context (see Silk & Rees 1998; Granato et al. 2001, 2004; Di Matteo, Springel & Hernquist 2005; Lapi et al. 2014). The impact of the biased collapse plus mergers scenario on the size evolution of galaxies at high redshift $z \gtrsim 1$ will be discussed in a forthcoming paper.

7.6 Summary and conclusions

We have investigated the origin, shape, scatter, and cosmic evolution of the observed relationship between specific angular momentum $j_\star$ and stellar mass $M_\star$ in ETGs and LTGs. Our main findings are summarized as follows.

1. We have exploited the observed star-formation efficiency $f_\star$ and chemical abundance $Z_\star$ to infer the fraction $f_{\rm inf}$ of baryons that infall toward the central

regions of galaxies (see Section 7.3). We find $f_{\rm inf} \approx 1$ for LTGs and ≈ 0.4 for ETGs weakly dependent on $M_\star$ (see Section7.4) with an uncertainties of about 0.25 dex.

2. We have highlighted that the infall fraction $f_{\rm inf}$ is the key variable in determining the distinct loci occupied by LTGs and ETGs in the $j_\star$ versus $M_\star$ diagram, with ETGs featuring relatively lower specific angular momentum than LTGs (see Section 7.4).

3. We have estimated the fraction $f_j \equiv j_\star / j_{\rm inf}$ of the specific angular momentum associated with the infalling gas eventually retained in the stellar component. For LTGs, we have found $f_j \approx 1.1^{+0.75}_{-0.44}$, which is consistent with the results from observations and simulations and matches the standard disc formation picture (see Section7.4). For ETGs, we have found that $f_j \approx 0.64^{+0.2}_{-0.16}$, which can be explained by a late-time evolution due to dry mergers.

4. We have found that the dependencies of $f_\star$ and $Z_\star$ on $M_\star$ conspire to make $j_\star \propto f_\star^{-2/3+s}\, Z_\star^{-s}$ weakly dependent on the stellar mass, with an overall shape close to $j_\star \propto M_\star^{2/3}$, see Section 7.4.

5. We have shown that the scatter in the observed $j_\star$ versus $M_\star$ relationship for ETGs and LTGs mainly comes from the intrinsic variance in the halo spin parameter λ, while the uncertainties in star-formation efficiency $f_\star$ and stellar metallicity $Z_\star$ are minor contributors (Section 7.4).

6. We have highlighted that the specific angular momentum $j_\star$ for most ($\sim 70\%$) of the observed star-forming galaxies at $z \sim 2$ is indeed very close to the local value for ETGs, as expected in our scenario (see Section 7.5.2). Recent analyses of state-of-the-art numerical simulations (e.g., Lagos et al. 2017) start to find evidence that an early star formation quenching can imprint low specific angular momentum in the stellar component, in pleasing agreement with our scenario based on biased collapse plus mergers.

All in all, we find that, for LTGs, the specific angular momentum steadily changes over cosmological timescales following the external gas inflow, while for ETGs, the specific angular momentum is mainly imprinted in a biased collapse at high redshift and then possibly undergoes a minor decrease due to late-time dry mergers. Thus, we argue that the angular momentum of both galaxy types is mainly imprinted by nature (particularly by the assembly history of their host DM halos) and not nurtured substantially by the environment.

Part IV:

Summary and Outlook

Chapter 8

Summary and Outlook

In summary, during my Ph.D, I have mainly studied several aspects related with structure growth: one is the the origin of the angular momentum in ETGs and LTGs. And the other one is halo bias and assembly and the environmental effects on them.

It has long been confirmed that mass is determent for halo bias (linear). However, the work in Chapter 4 shows in both Lagrangian and Eulerian framework that once the environment is fixed, the bias factor is basically totally determined, independent of halo mass, see equation (4.25). It shows that most of the observed environmental dependence of galaxies is coming from halo-environment relations.

Halos are cradles of galaxies and they lie in various types of large scale structures. With the advent of the phenomenon called "assembly bias", the role of large scale structures played in shaping halo and galaxy properties has raised wide interests. On the other hand, people generally assume that current halo properties are determined by their accretion history, which is quite reasonable yet not tested in the real data. In the work shown in Chapter 5, we have used two sets of high resolution simulations to recognize the halos that about to infall on two kinds of host halos: MW size and cluster size DM halos. We found tight correlation between the local tidal strength and the tangential infall velocity, which is absent between the radial infall velocity and the tidal field. Halo accretion is anisotropic and it is along the principal axes of the tidal field. Opposite accretion patterns are found in weak and strong tidal fields: in weak field, the gravity from the host dominates, resulting in radial accretion flow; while in the strong field, the accretion flow is less radial due to the increasing gravitational effect from surrounding structure. These results enrich the manifestations for "assembly bias". Our study further provides evidences for the actual link between dynamic properties of accreted subhalos with the current dynamical properties of halo. In the sense that halos with more radially dominated accretion are going to have more anisotropic internal velocity dispersion and smaller spin. These results can be used to explain how the internal

velocity anisotropy and spin of halos depend on environment. They can also be used to understand the strong alignments we find between the principal axes of the internal velocity ellipsoids of halos and the local tidal field, and their dependence on the strength of tidal field. We also found that the spin-tidal field alignment signal follows the prediction of the TTT only in the weak filed, while the trend is reversed in the strong field, which can be understood within the above results. Our work gives us a new perspective on the well-known yet still very intriguing "assembly bias". Meanwhile, it indicates the importance of both the strength and anisotropy of the tidal field. It also has important implications for the galaxy-LSS alignment measurements.

As for the assembly of subhalos, we have gotten for the first time a bimodal formation redshift distribution for accreted subhalos in the simulation (see Chapter 6). We managed to explain this bimodal feature using two phase accretion history. How will this bimodality from dark side contribute to the color/SFR bimodality observed in galaxies is a study to be done in the future.

Within the hierarchy structure formation formalism, mergers between galaxies are believed to be the main reason for morphology transition by a lot of studies. Mergers are thought be able to dissipate the angular momentum of disks and producing ellipticals with more randomized internal velocity motion. In the work shown in Chapter 7, we have found that even though mergers do exist, they may be not as important as expected in shaping galaxies statistically. We start with some commonly used assumptions, i.e., baryons and DM are very well mixed and have the same angular momentum distribution initially. Then we exploit the observed SFE and chemical abundance to infer the baryon infall fraction for ETGs to be $\sim$ 0.4 and for LTGs to be $\sim$ 1. The difference in $f_{\rm inf}$ is the main factor that determines the final angular momentum of those two types, producing effectively two parallel relations on $j_\star$ versus $M_\star$ plane. Further comparing with the observed $j_\star$ versus $M_\star$ relations reveals that the retention factors (relative to the initial angular momentum of infalling gas) for ETGs and LTGs are $0.64^{+0.20}_{-0.16}$ and $1.11^{+0.75}_{-0.44}$ separately. By carefully taking into account all possible errors and scatters in our calculation, we found that the dispersion for the observed $j_\star$ versus $M_\star$ relation for each type mainly originates from the intrinsic dispersion of halo spin distribution. Our results for LTGs are in general consistent with the classic disk formation picture. While our results for ETGs suggest a "biased collapse" plus merger scenario, with minor dry mergers contributing to the low redshift mass and size growth. This is consistent with the two phase growth scenario mentioned in Section 3.2.2.

In the future, I will expand my studies on the angular momentum to the size of galaxies, especially for ETGs. With the gas infall fraction gotten from Chapter 7, combined with the requirement for stability(Toomre, 1964), we are able to give an estimate for the size of ETGs at high z, as shown in Figure 8.1.

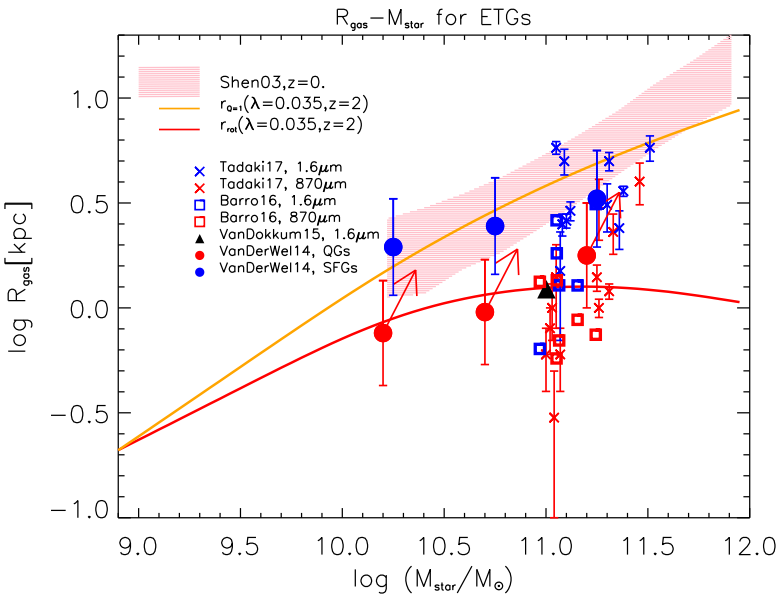

Figure 8.1: **Preliminary results:** Mass-size relation for ETGs and their high-z progenitors. The red shaded area represents measurements for local ETGs with 1σ variance from Shen et al. (2003). The solid red line is $r_{\rm rot}$ with $\lambda = 0.035$ at $z \approx 2$ while the solid orange line is $r_{Q=1}$. Here $r_{Q=1}$ is the stability radius before gas fragmentation and $r_{\rm rot}$ is the radius when the gravitational and centrifugal force balances . Data are from: Tadaki et al. (2017), blue cross for 870 μm and red cross for 1.6 μm, slightly offset for clarity; Barro et al. (2016), blue squares for 870 μm and red square for 1.6 μm; van Dokkum et al. (2015), black filled triangle is the mean of their sample at 1.6 μm; van der Wel et al. (2014), red filled circles for quiescent galaxies and blue filled circles for star-forming galaxies at $z = 2.25$. The red arrows indicate the average evolution in mass and radius via minor dry mergers, as envisaged by Belli, Newman & Ellis (2014).

Another interesting project is to use the galaxy clustering signal in varying environments (see Appendix A.1) to constrain the cosmology parameters, such as σ_8, see Figure 5 of Abbas & Sheth (2007). Further more, the 1-halo to 2-halo term transition is expected to be more distinct in underdense region, we would expect the measurement of the transition scale in varying environments could provide better constraints on the definition of halo virial radius from observation.

With our discovery of the bimodal $z_{\rm f}$ distribution, I will study further whether environment plays a role or not. It is worthy to check how this subhalo bimodality may/may not propagate to galaxies in order to shed light on the bimodal properties of galaxies from the dark side. Hydro-dynamical simulation may be a good tool to quantify those effect.

Appendix A

A.1 Relation of the work in Chapter 4 to Abbas & Sheth (2007)

It is natural and common to define the environment of a galaxy by counting the number of other galaxies within a specified distance from it. Suppose that the scale which defines the environment is substantially larger than the galaxy itself, and one selects a subset of galaxies based on this environment. If one measures the galaxy-galaxy correlation function for each such subset, then one will find that galaxy clustering is not a monotonic function of environment (Abbas & Sheth, 2007). Whereas the galaxies with the most neighbors are the most strongly clustered, those with the fewest neighbors are not the least strongly clustered: the least clustered galaxies are associated with only moderately underdense environments.

Abbas & Sheth (2007) showed that this effect was present in a mock catalog in which the number of galaxies in a halo depends on halo mass and not its environment. The agreement between the environmental trends in the data and in their mock catalog means that we can make other measurements, some of which are not possible in the data, so as to illustrate a few other interesting points.

To reduce the effect of redshift space distortions, the measurements in the data were restricted to a projected measurement. Figure A.1 shows the corresponding real-space measurement in the mock catalog. Galaxies were ranked by the number of objects within $8h^{-1}$Mpc; empty triangles show the clustering signal for the objects in the top ten percentile, and filled triangles show it for the objects between the top ten and thirty percentiles. To help set the scale, the dotted lines show ξ_{mm} in linear theory and nonlinear theory (larger on small scales). Open and filled squares show the objects in the bottom ten, and between the bottom ten and thirty percentiles. Notice the effect mentioned above: clustering is not a monotonic function of environment. In particular, the objects in moderately underdense patches are very weakly clustered (filled squares).

This non-monotonicity is a consequence of the fact that the measurement is

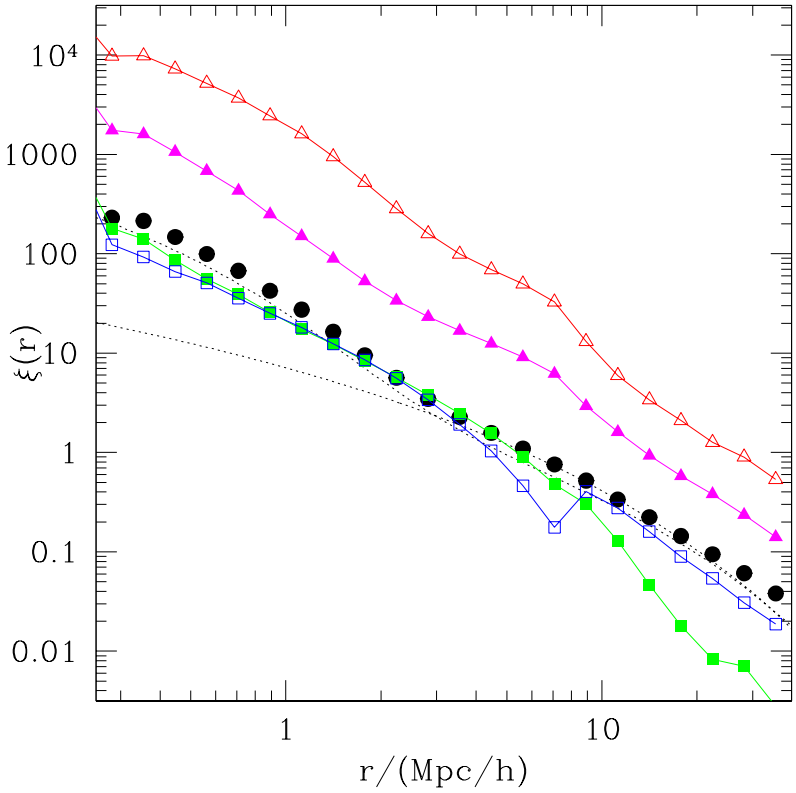

Figure A.1: Environmental dependence of the galaxy-galaxy auto-correlation function. Results for four bins in environment – defined to be the number of galaxies within $8h^{-1}$Mpc – are shown. Open triangles, filled triangles, filled squares and open squares show results for the densest to the least dense environments. This measure of clustering is not a monotonic function of environment. To guide the eye, filled circles show the auto-correlation function of the full sample, and the two dotted curves show the dark matter correlation function in linear and nonlinear theory.

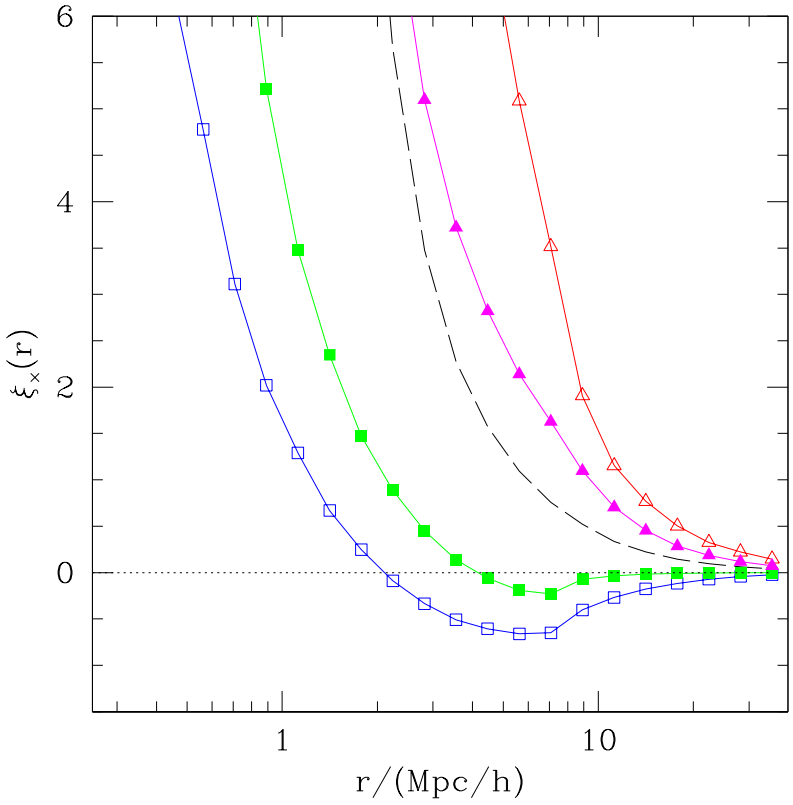

Figure A.2: Environmental dependence of the galaxy-total cross-correlation function. The symbols show the same environmental bins as before, cross-correlated with the full sample (dashed curve shows the auto-correlation function of the full sample). Note that the y-axis is linear rather than log, since the signal for underdense regions crosses zero. This signal is clearly monotonic with environment.

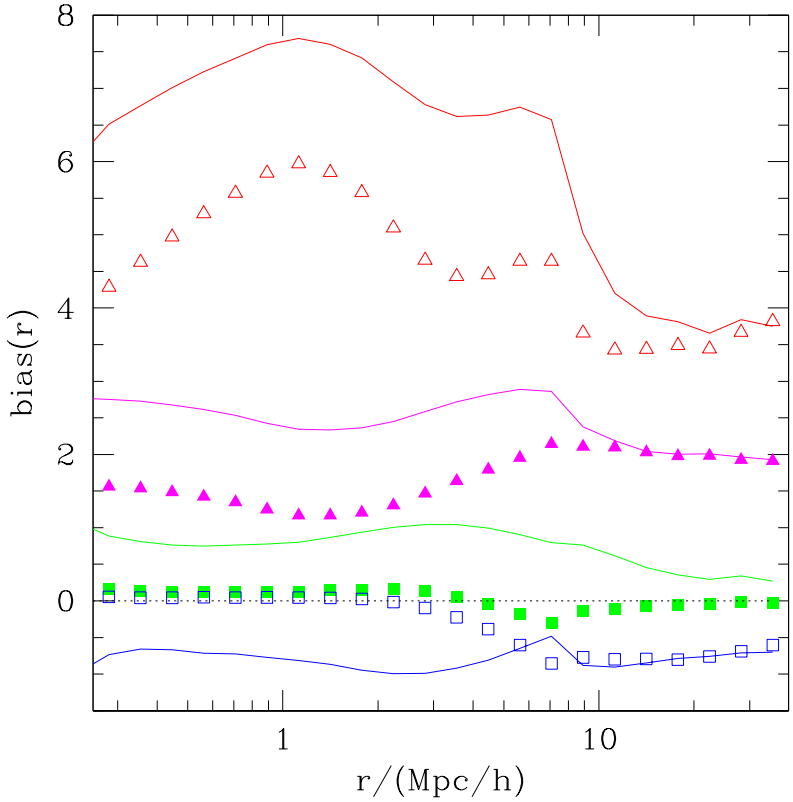

Figure A.3: Environmental dependence of galaxy bias. Symbols show the ratio of the cross-correlation to the auto correlation of the full sample (symbols divided by dashed curve in previous figure); curves show the square-root of the ratio of the ratio of the symbols divided by filled circles in Figure A.1 (and multiplied by -1 for the least dense region).

an auto-correlation function. On large scales, $\xi_{gg} \propto b_g^2 \xi_{mm}$, so the measurement cannot distinguish between positive and negative b_g. While this was implicit in their discussion, Abbas & Sheth (2007) did not show a plot illustrating that b_g itself *is* monotonic with environment (and, in particular, is negative for underdense regions). To rectify this omission, Figure A.2 shows the cross-correlation between each subsample and the total. This signal is clearly monotonic with environment.

If we use b_t to denote the bias factor of the full sample and b_g that of a subsample, then, on large scales, this cross-correlation signal should be proportional to $\xi_{gt} \propto b_g b_t \xi_{mm}$. Since b_t is the same for all the measurements, the amplitude of the signal on large scales is proportional to b_g. To highlight this, the symbols in Figure A.3 show the ratio $\xi_{gt}/\xi_{tt} = (b_g/b_t)$ for the four subsamples (while this does not matter for our argument, it may help to notice from Figure A.1 that $b_t \sim 1$).

The symbols show clearly that b_g is monotonic with environment: it is negative for the least underdense regions, close to zero for moderately underdense regions, and positive for overdense regions.

To show that the non-monotonic signal in the auto-correlation function is a consequence of it not being able to distinguish between positive and negative bias factors, the lines show $\sqrt{\xi_{gg}/\xi_{tt}}$, except for the signal from the least dense regions, which we multiply by -1. Except for the sample which had $b_g \sim 0$, the agreement with the symbols is excellent on large scales indicating that, indeed, the non-monotonicity in ξ_{gg} is because it scales as b_g^2.

The main text develops a model for the precise trend with environment. It is interesting that the bins in environment here lead to rather similar large scale bias as shown in Figure 4.1 of the main text.

A.2 Implications for galaxy bias

Figure 8 in Pujol et al. (2017) shows that a halo mass based approach (mHOD) does not recover the color dependence of galaxy bias, while a density based model (dHOD) does. Below, we express their results in our notation.

Consider the case of bias as a function of color. For Gaussian distributions, the mean overdensity Δ_0 at fixed color is

$$\langle \Delta_0 | g_c \rangle = \langle \Delta_0 g_c \rangle \frac{g_c}{\langle g_c^2 \rangle} \ , \tag{A.1}$$

where g_c stands for the constraint which specifies galaxy color. The mHOD model approximates this as

$$\int \mathrm{d}m \, \langle \Delta_0 | m \rangle \, p(m|g_c) = \frac{\langle \Delta_0 m \rangle \langle m g_c \rangle}{\langle m^2 \rangle} \frac{g_c}{\langle g_c^2 \rangle} \tag{A.2}$$

(their equation 5). This will be a good approximation if $\langle \Delta_0 m \rangle \langle m g_c \rangle / \langle m^2 \rangle \approx \langle \Delta_0 g_c \rangle$: i.e., if the Δ_0-color correlation is entirely due to the correlations of each with halo mass m. The grey curve in the upper panel of their Figure 8 shows that this is a poor approximation to the actual relation; mass alone cannot account for the Δ_0-color correlation.

The dHOD approximation uses the environment Δ_e instead of halo mass:

$$\int \mathrm{d}\Delta_e \, \langle \Delta_0 | \Delta_e \rangle \, p(\Delta_e | g_c) = \frac{\langle \Delta_0 \Delta_e \rangle \langle \Delta_e g_c \rangle}{\langle \Delta_e^2 \rangle} \frac{g_c}{\langle g_c^2 \rangle} \tag{A.3}$$

(their equation 6). The red curve in the upper panel of their Figure 8 shows that this works well, implying that $\langle \Delta_0 \Delta_e \rangle \langle \Delta_e g_c \rangle / \langle \Delta_e^2 \rangle \approx \langle \Delta_0 g_c \rangle$; the Δ_0-color correlation is almost entirely due to the correlations of each with Δ_e.

The case of bias for given luminosity is similar to the one for given color by simply replacing g_c with $g_{\rm L}$, where $g_{\rm L}$ represents galaxy luminosity. (Strictly speaking, to model the bottom panel in their Figure 8 $g_{\rm L}$ must stand for the luminosity of a red central galaxy.) At large luminosities, there is a tight $m - g_{\rm L}$ relation, so the mHOD approach (grey curve in their lower panel) provides a good approximation to the true relation. However, at the faint end, the $m - g_{\rm L}$ relation is much looser, so the mHOD reconstruction fails. As there are many more faint red galaxies than bright, the statistics in their top panel are dominated by the faint objects, for which the mHOD approach fails.

Appendix B

B.1 Additional effects on the estimate of the infalling fraction

In this appendix we consider two additional effects that can somewhat alter the estimate of the infalling fraction $f_{\rm inf}$ discussed in Section 7.2.

The first effect concerns the metallicity of the infalling gas, which was neglected in Section 7.2. We now suppose that the gas mass $M_{\rm inf}$ infalling toward the central galaxy region is endowed with a metallicity $\langle Z_{\rm inf}\rangle$. Then, the metal conservation equation (7.10) must be modified into

$$y_Z\, M_\star + \langle Z_{\rm inf}\rangle\, M_{\rm inf} = M_{\rm Z,gal} + M_{\rm Z,out}\ , \tag{B.1}$$

and, along the same line as Section 7.2 we find that the infall fraction now reads

$$f_{\rm inf} = \frac{f_\star}{1 - \langle Z_{\rm inf}\rangle/\zeta\,\langle Z_\star\rangle}\left(\frac{y_Z}{\zeta\,\langle Z_\star\rangle} - \frac{M_{\rm Z,gal}}{\zeta\,\langle Z_\star\rangle\, M_\star} + \frac{M_{\rm gal}}{M_\star}\right)\ . \tag{B.2}$$

This replaces equation (7.11) in Chapter 7, which is recovered when $\langle Z_{\rm inf}\rangle \ll \zeta\,\langle Z_\star\rangle$. The metallicity of the infalling gas is likely to be quite small, $\langle Z_{\rm inf}\rangle \lesssim$ a few $10^{-2}\,Z_\odot$, as suggested by various estimates for the IGM of local and high-redshift systems (for a review, see Madau & Dickinson (2014)). Considering that $\zeta\,\langle Z_\star\rangle \gtrsim$ a few $10^{-1}\,Z_\odot$ (cf. Figure 7.2), the correction to our estimate of $f_{\rm inf}$ is minor.

The second effect concerns the possibility that part of the outflowing gas falls back onto the galaxy, in the way of a galactic fountain circulation. We suppose that a fraction $\chi_{\rm rec}$ of the gas mass $M_{\rm out}$ outflown with metallicity $\langle Z_{\rm out}\rangle$ by feedback can fall back to the central galaxy after possible mixing with the metal poor gas in the outer regions.

The equation for the gas mass actually taking part in the galaxy formation process is now written as

$$M_{\rm inf} = M_{\rm gal} + (1 - \chi_{\rm rec})\, M_{\rm out}\ , \tag{B.3}$$

and the metal mass conservation equation is modified into

$$y_Z\, M_\star + \langle Z_{\rm out}\,\rangle \chi_{\rm rec}\, M_{\rm out} = M_{Z,\rm gal} + \langle Z_{\rm out}\rangle\, M_{\rm out}\ . \tag{B.4}$$

With respect to the equations in the main text, this amounts to a redefinition of the outflowing gas mass from $M_{\rm out}$ into $(1-\chi_{\rm rec})\, M_{\rm out}$. It is apparent that, in a one-zone model like that considered here, galactic fountain circulation does not affect the final value of $f_{\rm inf}$, which turns out to be unchanged with respect to equation (7.11). As a matter of fact, in detailed and spatially resolved chemical evolution approaches, the galactic fountain is relevant in time delaying and spatially displacing metals (e.g., Spitoni, Matteucci & Marcon-Uchida 2013).

B.2 Halo angular momentum profile

B.2.1 Simulation and halo identification

In this work, we exploit a $N-$body simulation based on the Gadget-2 code (Springel, 2005). The simulation adopted a flat ΛCDM cosmological model from WMAP9 constraints (Hinshaw et al., 2013) with $\Omega_\Lambda = 0.718$, $\Omega_M = 0.282$, $\Omega_b = 0.046$, and $h = H_0/100$ km s^{-1} Mpc^{-1} $= 0.697$, $\sigma_8 = 0.817$ and $n_s = 0.96$. The CDM density field is traced by 2048^3 particles, each with mass $m_{\rm p} \approx 7.29\times10^7\, M_\odot\, h^{-1}$, from $z = 120$ to 0 in a cubic box of a side length 200 Mpc h^{-1}. The gravitational force is softened isotropically on a comoving length scale of $2\, h^{-1}$ kpc (Plummer equivalent). We have 100 snapshots from $z = 20$ to 0 equally spaced in the logarithm of the expansion factor.

The dark matter halos are identified with the FOF group algorithm (Davis et al., 1985) and a linking length of $0.2\, b$, where b is the mean interparticle separation. We resolve all groups with at least 20 particles. Furthermore, we run SUBFIND (Springel et al., 2001) to acquire the self-bound subhalo catalog for each snapshot. We define the halo mass as the mass contained in a spherical region (centered on the dominant subhalo particle with the minimum gravitational potential) with an average density equals $200\,\rho_{\rm crit}$. In the calculation, we take the halo mass range $M_{\rm vir} \sim 10^{11} - 10^{13}\, h^{-1}\, M_\odot$.

B.2.2 Specific angular momentum profile

Bullock et al. (2001) found a power-law approximation that describes the angular momentum reasonably well:

$$j_z(M) \propto M(<r)^s \tag{B.5}$$

	$z = 0$	$z = 1$	$z = 2$	$z = 3$	$z = 4$
μ	1.120	1.043	0.927	0.817	0.737
σ	0.352	0.364	0.344	0.320	0.300

Table B.1: Distribution of s at different redshifts. Note that a Gaussian function with mean μ and variance σ has been adopted.

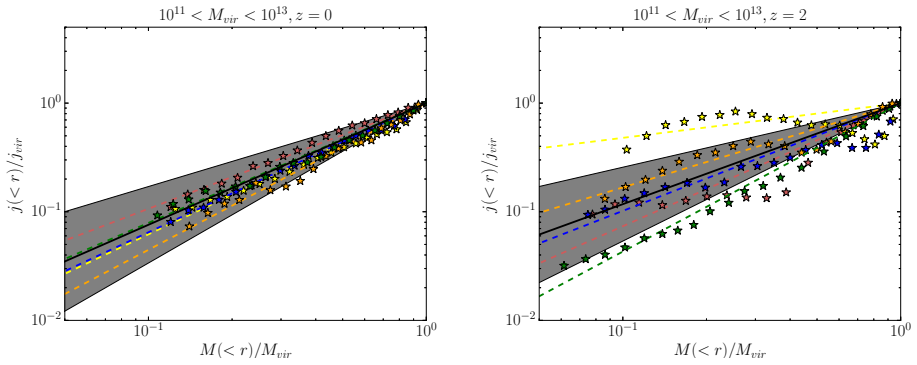

Figure B.1: Specific angular momentum vs. mass profile at redshifts $z = 0$ and 2. The lines with stars are the results for several randomly chosen halos in the sample, while the dashed lines are the fits with equation (B.6). The black solid lines and the grey shaded areas show the mean profiles and their associated 1σ variance.

where s is roughly distributed over the halos like a Gaussian with average $s = 1.3 \pm 0.3$. Note that $j_z(M)$ is the specific angular momentum projected to the direction of total angular momentum J.

Here, we look for a description of the relation between $j(M)$ and $M(< r)$, where $j(M)$ is the specific angular momentum (unprojected) within the shell with mass $M(< r)$. So, we first divide each halo into shells between $0.1\, r_{\rm vir}$ and $r_{\rm vir}$. Then, in each shell, we calculate the specific angular momentum $j(< r)$ and mass $M(< r)$. Even though $j(< r)$ does not always increase monotonically with $M(< r)$, as shown by the data points in FigureB.1, the power-law fitting does provide a useful rendition for the spherical distribution of j on a statistical basis. Thus, we use the formula

$$\frac{j(M)}{j_{vir}} = \left[\frac{M(< r)}{M_{vir}}\right]^{s} \tag{B.6}$$

to fit our measurements in each halo of our samples. In addition, we check the mass and redshift dependence of the power-law parameter s in Figure B.2. We find a very weak dependence on the mass and a decreasing s with increasing z. The fitting parameters for s with varying z are listed in Table B.1.

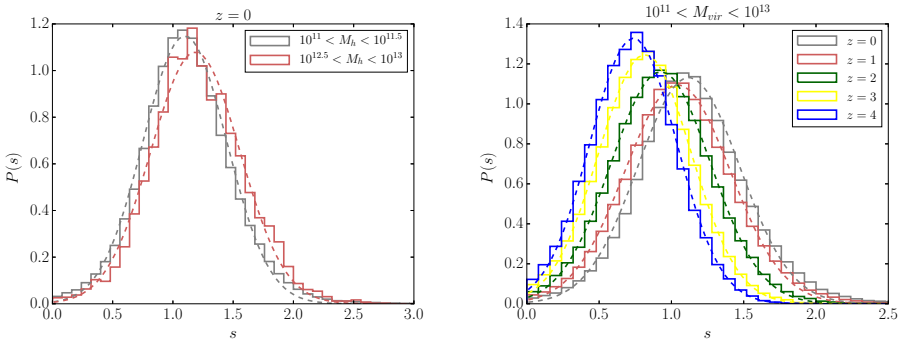

Figure B.2: Left panel: distribution of s (power-law parameter in the specific angular momentum profile) for different halo masses at $z = 0$. Right panel: distribution of s at different redshifts for halo masses $M_{\rm vir} \sim 10^{11} - 10^{13}\, h^{-1}\, M_{\odot}$. The dashed lines illustrate the Gaussian fits with the fitting parameters given in Table B.1.

Bibliography

Abbas U., Sheth R. K., 2007, MNRAS, 378, 641

Abraham R. G., 1998, ArXiv Astrophysics e-prints

Allgood B., Flores R. A., Primack J. R., Kravtsov A. V., Wechsler R. H., Faltenbacher A., Bullock J. S., 2006, MNRAS, 367, 1781

Angulo R. E., Lacey C. G., Baugh C. M., Frenk C. S., 2009, MNRAS, 399, 983

Aversa R., Lapi A., de Zotti G., Shankar F., Danese L., 2015, ApJ, 810, 74

Bahé Y. M., McCarthy I. G., Crain R. A., Theuns T., 2012, MNRAS, 424, 1179

Barnes J., Efstathiou G., 1987, ApJ, 319, 575

Barro G. et al., 2016, ApJ, 827, L32

Baugh C. M., Cole S., Frenk C. S., 1996, MNRAS, 283, 1361

Begeman K. G., 1989, A&A, 223, 47

Behroozi P. S., Conroy C., Wechsler R. H., 2010, ApJ, 717, 379

Behroozi P. S., Wechsler R. H., Conroy C., 2013, ApJ, 770, 57

Belli S., Newman A. B., Ellis R. S., 2014, ApJ, 783, 117

Bellovary J. M., Dalcanton J. J., Babul A., Quinn T. R., Maas R. W., Austin C. G., Williams L. L. R., Barnes E. I., 2008, ApJ, 685, 739

Benson A. J., 2005, MNRAS, 358, 551

Bernardeau F., 1994, A&A, 291, 697

Bernardeau F., Colombi S., Gaztañaga E., Scoccimarro R., 2002, Phys. Rep., 367, 1

Bett P., Eke V., Frenk C. S., Jenkins A., Helly J., Navarro J., 2007, MNRAS, 376, 215

Blumenthal G. R., Faber S. M., Flores R., Primack J. R., 1986, ApJ, 301, 27

Böhringer H., 2014, Mem. Soc. Astron. Italiana, 85, 396

Bond J. R., Cole S., Efstathiou G., Kaiser N., 1991, ApJ, 379, 440

Bosma A., 1981, AJ, 86, 1825

Bournaud F., 2016, Galactic Bulges, 418, 355

Bournaud F., Elmegreen B. G., Elmegreen D. M., 2007, ApJ, 670, 237

Bower R. G., Lucey J. R., Ellis R. S., 1992, MNRAS, 254, 601

Boylan-Kolchin M., Springel V., White S. D. M., Jenkins A., Lemson G., 2009, MNRAS, 398, 1150

Bray A. D. et al., 2016, MNRAS, 455, 185

Bressan A., Granato G. L., Silva L., 1998, A&A, 332, 135

Brook C. B., Stinson G., Gibson B. K., Roškar R., Wadsley J., Quinn T., 2012, MNRAS, 419, 771

Bryan G. L., Norman M. L., 1998, ApJ, 495, 80

Bullock J. S., Dekel A., Kolatt T. S., Kravtsov A. V., Klypin A. A., Porciani C., Primack J. R., 2001, ApJ, 555, 240

Burkert A. et al., 2016, ApJ, 826, 214

Cappellari M., 2016, ARA&A, 54, 597

Cappellari M. et al., 2007, MNRAS, 379, 418

—, 2011, MNRAS, 413, 813

Carpintero D. D., Muzzio J. C., 1995, ApJ, 440, 5

Carroll S. M., Press W. H., Turner E. L., 1992, ARA&A, 30, 499

Catelan P., Theuns T., 1996, MNRAS, 282, 436

Chabrier G., 2003, PASP, 115, 763

Chaves-Montero J., Angulo R. E., Schaye J., Schaller M., Crain R. A., Furlong M., Theuns T., 2016, MNRAS, 460, 3100

Chiappini C., Matteucci F., Gratton R., 1997, ApJ, 477, 765

Chiueh T., Lee J., 2001, ApJ, 555, 83

Choi J., Conroy C., Moustakas J., Graves G. J., Holden B. P., Brodwin M., Brown M. J. I., van Dokkum P. G., 2014, ApJ, 792, 95

Christensen C., Quinn T., Governato F., Stilp A., Shen S., Wadsley J., 2012, MNRAS, 425, 3058

Citro A., Pozzetti L., Moresco M., Cimatti A., 2016, A&A, 592, A19

Cole S., Kaiser N., 1989, MNRAS, 237, 1127

Cole S., Lacey C. G., Baugh C. M., Frenk C. S., 2000, MNRAS, 319, 168

Colín P., Klypin A. A., Kravtsov A. V., 2000, ApJ, 539, 561

Conroy C., Wechsler R. H., Kravtsov A. V., 2006, ApJ, 647, 201

Contini T. et al., 2016, A&A, 591, A49

Cooray A., Sheth R., 2002, Phys. Rep., 372, 1

Cox T. J., Jonsson P., Primack J. R., Somerville R. S., 2006, MNRAS, 373, 1013

Cunow B., 2004, in Astrophysics and Space Science Library, Vol. 319, Penetrating Bars Through Masks of Cosmic Dust, Block D. L., Puerari I., Freeman K. C., Groess R., Block E. K., eds., p. 255

Dalal N., White M., Bond J. R., Shirokov A., 2008, ApJ, 687, 12

Danovich M., Dekel A., Hahn O., Ceverino D., Primack J., 2015, MNRAS, 449, 2087

Davies R. L., Efstathiou G., Fall S. M., Illingworth G., Schechter P. L., 1983, ApJ, 266, 41

Davis M., Efstathiou G., Frenk C. S., White S. D. M., 1985, ApJ, 292, 371

de Blok W. J. G., Walter F., Brinks E., Trachternach C., Oh S.-H., Kennicutt, Jr. R. C., 2008, AJ, 136, 2648

de Jong R. S., 1996, A&A, 313, 377

De Lucia G., Springel V., White S. D. M., Croton D., Kauffmann G., 2006, MNRAS, 366, 499

de Vaucouleurs G., 1948, Annales d'Astrophysique, 11, 247

—, 1974, in IAU Symposium, Vol. 58, The Formation and Dynamics of Galaxies, Shakeshaft J. R., ed., pp. 1–52

DeFelippis D., Genel S., Bryan G., Fall S. M., 2017, ArXiv e-prints

Dekel A., Sari R., Ceverino D., 2009, ApJ, 703, 785

Desjacques V., 2008, MNRAS, 388, 638

Di Matteo T., Springel V., Hernquist L., 2005, Nature, 433, 604

Dodelson S., 2003, Modern cosmology

Doroshkevich A. G., 1970, Astrophysics, 6, 320

Dutton A. A., Conroy C., van den Bosch F. C., Prada F., More S., 2010, MNRAS, 407, 2

Dutton A. A., van den Bosch F. C., 2012, MNRAS, 421, 608

Efstathiou G., Jones B. J. T., 1979, MNRAS, 186, 133

—, 1980, Comments on Astrophysics, 8, 169

Eggen O. J., Lynden-Bell D., Sandage A. R., 1962, ApJ, 136, 748

Eke V., Efstathiou G., Wright L., 2000, MNRAS, 315, L18

Emsellem E. et al., 2011, MNRAS, 414, 888

—, 2007, MNRAS, 379, 401

Fakhouri O., Ma C.-P., 2009, MNRAS, 394, 1825

Fakhouri O., Ma C.-P., Boylan-Kolchin M., 2010, MNRAS, 406, 2267

Fall S. M., 1983, in IAU Symposium, Vol. 100, Internal Kinematics and Dynamics of Galaxies, Athanassoula E., ed., pp. 391–398

—, 2002, in Astronomical Society of the Pacific Conference Series, Vol. 275, Disks of Galaxies: Kinematics, Dynamics and Peturbations, Athanassoula E., Bosma A., Mujica R., eds., pp. 389–396

Fall S. M., Efstathiou G., 1980, MNRAS, 193, 189

Fall S. M., Romanowsky A. J., 2013, ApJ, 769, L26

Faltenbacher A., White S. D. M., 2010, ApJ, 708, 469

Feldmann R., 2015, MNRAS, 449, 3274

Forero-Romero J. E., Contreras S., Padilla N., 2014a, MNRAS, 443, 1090

—, 2014b, MNRAS, 443, 1090

Freeman K. C., 1970, ApJ, 160, 811

Fukugita M., Hogan C. J., Peebles P. J. E., 1998, ApJ, 503, 518

Fukugita M., Peebles P. J. E., 2004, ApJ, 616, 643

Gallazzi A., Bell E. F., Zibetti S., Brinchmann J., Kelson D. D., 2014, ApJ, 788, 72

Gallazzi A., Charlot S., Brinchmann J., White S. D. M., 2006, MNRAS, 370, 1106

Gallazzi A., Charlot S., Brinchmann J., White S. D. M., Tremonti C. A., 2005, MNRAS, 362, 41

Gao L., Navarro J. F., Frenk C. S., Jenkins A., Springel V., White S. D. M., 2012, MNRAS, 425, 2169

Gao L., Springel V., White S. D. M., 2005, MNRAS, 363, L66

Gao L., White S. D. M., 2007, MNRAS, 377, L5

Gao L., White S. D. M., Jenkins A., Stoehr F., Springel V., 2004, MNRAS, 355, 819

Genel S., Fall S. M., Hernquist L., Vogelsberger M., Snyder G. F., Rodriguez-Gomez V., Sijacki D., Springel V., 2015, ApJ, 804, L40

Genel S. et al., 2014, MNRAS, 445, 175

Giocoli C., Tormen G., van den Bosch F. C., 2008, MNRAS, 386, 2135

Glazebrook K., 2013, PASA, 30, e056

Glazebrook K. et al., 2017, ArXiv e-prints

Goddard D. et al., 2017, MNRAS, 466, 4731

Gott, III J. R., Thuan T. X., 1976, ApJ, 204, 649

Governato F., Willman B., Mayer L., Brooks A., Stinson G., Valenzuela O., Wadsley J., Quinn T., 2007, MNRAS, 374, 1479

Granato G. L., De Zotti G., Silva L., Bressan A., Danese L., 2004, ApJ, 600, 580

Granato G. L., Silva L., Monaco P., Panuzzo P., Salucci P., De Zotti G., Danese L., 2001, MNRAS, 324, 757

Guo Q., White S., Li C., Boylan-Kolchin M., 2010, MNRAS, 404, 1111

Haffner L. M. et al., 2009, Reviews of Modern Physics, 81, 969

Hahn O., Porciani C., Carollo C. M., Dekel A., 2007, MNRAS, 375, 489

Hahn O., Porciani C., Dekel A., Carollo C. M., 2009, MNRAS, 398, 1742

Harrison C. M. et al., 2017, ArXiv e-prints

Hearin A. P., Behroozi P. S., van den Bosch F. C., 2016, MNRAS, 461, 2135

Hearin A. P., Watson D. F., 2013, MNRAS, 435, 1313

Hearin A. P., Watson D. F., Becker M. R., Reyes R., Berlind A. A., Zentner A. R., 2014, MNRAS, 444, 729

Hester J. A., Tasitsiomi A., 2010, ApJ, 715, 342

Hinshaw G. et al., 2013, ApJS, 208, 19

Hopkins P. F., Hernquist L., Cox T. J., Keres D., Wuyts S., 2009, ApJ, 691, 1424

Hoyle F., 1949, in Burgers J. M., van de Hulst H. C., eds, Problems of Cosmical Aerodynamics, The origin of the rotations of the galaxies. Central Air Documents Office, Dayton, OH, pp 195–197

Huang K.-H. et al., 2017a, ApJ, 838, 6

Huang S., Ho L. C., Peng C. Y., Li Z.-Y., Barth A. J., 2013, ApJ, 766, 47

Huang S., Leauthaud A., Greene J., Bundy K., Lin Y.-T., Tanaka M., Miyazaki S., Komiyama Y., 2017b, ArXiv e-prints

Hubble E. P., 1926, ApJ, 64

Hudson M. J. et al., 2015, MNRAS, 447, 298

Immeli A., Samland M., Gerhard O., Westera P., 2004a, A&A, 413, 547

Immeli A., Samland M., Westera P., Gerhard O., 2004b, ApJ, 611, 20

Jiang F., van den Bosch F. C., 2014, MNRAS, 440, 193

Jiang L., Cole S., Sawala T., Frenk C. S., 2014, ArXiv e-prints

Jing Y. P., Suto Y., Mo H. J., 2007, ApJ, 657, 664

Kaiser N., 1984, ApJ, 284, L9

Kang X., van den Bosch F. C., Pasquali A., 2007, MNRAS, 381, 389

Kauffmann G., 1996, MNRAS, 281, 487

Kauffmann G., Li C., Zhang W., Weinmann S., 2013, MNRAS, 430, 1447

Kauffmann G., White S. D. M., 1993, MNRAS, 261

Keselman J. A., Nusser A., 2007, MNRAS, 382, 1853

Kormendy J., Bender R., 1996, ApJ, 464, L119

Kriek M. et al., 2016, Nature, 540, 248

Krumholz M. R., Dekel A., 2012, ApJ, 753, 16

Lacerna I., Padilla N., 2011, MNRAS, 412, 1283

—, 2012, MNRAS, 426, L26

Lacey C., Cole S., 1993, MNRAS, 262, 627

Lagos C. d. P., Theuns T., Stevens A. R. H., Cortese L., Padilla N. D., Davis T. A., Contreras S., Croton D., 2017, MNRAS, 464, 3850

Lam T. Y., Sheth R. K., 2008, MNRAS, 386, 407

Lapi A., Raimundo S., Aversa R., Cai Z.-Y., Negrello M., Celotti A., De Zotti G., Danese L., 2014, ApJ, 782, 69

Lapi A., Salucci P., Danese L., 2013, ApJ, 772, 85

Lapi A., Shankar F., Mao J., Granato G. L., Silva L., De Zotti G., Danese L., 2006, ApJ, 650, 42

Leccardi A., Rossetti M., Molendi S., 2010, A&A, 510, A82

Lesgourgues J., 2011, ArXiv e-prints

Lewis A., Bridle S., 2002, Phys. Rev., D66, 103511

Li R., Gao L., Xie L., Guo Q., 2013, MNRAS, 435, 3592

Li Y., Mo H., 2009, ArXiv e-prints

Li Y., Mo H. J., Gao L., 2008, MNRAS, 389, 1419

Libeskind N. I., Hoffman Y., Forero-Romero J., Gottlöber S., Knebe A., Steinmetz M., Klypin A., 2013a, MNRAS, 428, 2489

Libeskind N. I., Hoffman Y., Gottlöber S., 2014, MNRAS, 441, 1974

Libeskind N. I., Hoffman Y., Steinmetz M., Gottlöber S., Knebe A., Hess S., 2013b, ApJ, 766, L15

Libeskind N. I., Knebe A., Hoffman Y., Gottlöber S., 2014, MNRAS, 443, 1274

Lin W. P., Jing Y. P., Lin L., 2003, MNRAS, 344, 1327

Lonoce I. et al., 2015, MNRAS, 454, 3912

Lu Y., Mo H. J., Katz N., Weinberg M. D., 2006, MNRAS, 368, 1931

Ludlow A. D., Navarro J. F., Springel V., Jenkins A., Frenk C. S., Helmi A., 2009, ApJ, 692, 931

Ludlow A. D., Navarro J. F., White S. D. M., Boylan-Kolchin M., Springel V., Jenkins A., Frenk C. S., 2011, MNRAS, 415, 3895

Ma X., Hopkins P. F., Feldmann R., Torrey P., Faucher-Giguère C.-A., Kereš D., 2017, MNRAS, 466, 4780

Macciò A. V., Dutton A. A., van den Bosch F. C., 2008, MNRAS, 391, 1940

Macciò A. V., Dutton A. A., van den Bosch F. C., Moore B., Potter D., Stadel J., 2007, MNRAS, 378, 55

MacMillan J. D., Widrow L. M., Henriksen R. N., 2006, ApJ, 653, 43

Madau P., Dickinson M., 2014, ARA&A, 52, 415

Maller A. H., Dekel A., 2002, MNRAS, 335, 487

Man A. W. S., Zirm A. W., Toft S., 2016, ApJ, 830, 89

Mandelbaum R., Wang W., Zu Y., White S., Henriques B., More S., 2016, MNRAS, 457, 3200

Matteucci F., 1994, A&A, 288, 57

Matteucci F., Greggio L., 1986, A&A, 154, 279

Maulbetsch C., Avila-Reese V., Colín P., Gottlöber S., Khalatyan A., Steinmetz M., 2007, ApJ, 654, 53

McBride J., Fakhouri O., Ma C.-P., 2009, MNRAS, 398, 1858

McDonald P., Seljak U., 2009, J. Cosmology Astropart. Phys., 10, 007

Mo H., van den Bosch F. C., White S., 2010, Galaxy Formation and Evolution

Mo H. J., Mao S., 2004, MNRAS, 353, 829

Mo H. J., Mao S., White S. D. M., 1998, MNRAS, 295, 319

Mo H. J., White S. D. M., 1996, MNRAS, 282, 347

Moffett A. J., Kannappan S. J., Berlind A. A., Eckert K. D., Stark D. V., Hendel D., Norris M. A., Grogin N. A., 2015, ApJ, 812, 89

Mollá M., Díaz Á. I., Gibson B. K., Cavichia O., López-Sánchez Á.-R., 2016, MNRAS, 462, 1329

Monaco P., 2016, Galaxies, 4, 53

Monaco P., Theuns T., Taffoni G., 2002, MNRAS, 331, 587

Monaco P., Theuns T., Taffoni G., Governato F., Quinn T., Stadel J., 2002, ApJ, 564, 8

More S., van den Bosch F. C., Cacciato M., Skibba R., Mo H. J., Yang X., 2011, MNRAS, 410, 210

Moster B. P., Naab T., White S. D. M., 2013, MNRAS, 428, 3121

Musso M., Sheth R. K., 2012, MNRAS, 423, L102

—, 2014, MNRAS, 443, 1601

Naab T., Burkert A., 2003, ApJ, 597, 893

Naab T., Johansson P. H., Ostriker J. P., 2009, ApJ, 699, L178

Navarro J. F., Frenk C. S., White S. D. M., 1995, MNRAS, 275, 56

—, 1996, ApJ, 462, 563

—, 1997, ApJ, 490, 493

Navarro J. F., Steinmetz M., 2000, ApJ, 538, 477

Noguchi M., 1999, ApJ, 514, 77

Obreschkow D., Glazebrook K., 2014, ApJ, 784, 26

Onodera M. et al., 2015, ApJ, 808, 161

Oser L., Naab T., Ostriker J. P., Johansson P. H., 2012, ApJ, 744, 63

Oser L., Ostriker J. P., Naab T., Johansson P. H., Burkert A., 2010, ApJ, 725, 2312

Pahwa I., Paranjape A., 2017, MNRAS, 470, 1298

Paranjape A., Hahn O., Sheth R. K., 2017, ArXiv e-prints

Paranjape A., Kovač K., Hartley W. G., Pahwa I., 2015, MNRAS, 454, 3030

Parkinson H., Cole S., Helly J., 2008, MNRAS, 383, 557

Parry O. H., Eke V. R., Frenk C. S., 2009, MNRAS, 396, 1972

Peebles P. J. E., 1969, ApJ, 155, 393

—, 1971, A&A, 11, 377

Peeples M. S., Werk J. K., Tumlinson J., Oppenheimer B. D., Prochaska J. X., Katz N., Weinberg D. H., 2014, ApJ, 786, 54

Peletier R., Davies R. L., Illingworth G., 1990, Structure and colour gradients in elliptical galaxies., Wielen R., ed., pp. 267–269

Persic M., Salucci P., 1992, MNRAS, 258, 14P

Pezzulli G., Fraternali F., 2016, MNRAS, 455, 2308

Pezzulli G., Fraternali F., Boissier S., Muñoz-Mateos J. C., 2015, MNRAS, 451, 2324

Pipino A., Matteucci F., 2004, MNRAS, 347, 968

Pizzella A., Corsini E. M., Vega Beltrán J. C., Bertola F., 2004, A&A, 424, 447

Planck Collaboration et al., 2016, A&A, 594, A13

Porciani C., Dekel A., Hoffman Y., 2002a, MNRAS, 332, 325

—, 2002b, MNRAS, 332, 339

Porter L. A., Somerville R. S., Primack J. R., Johansson P. H., 2014, MNRAS, 444, 942

Pujol A., Hoffmann K., Jiménez N., Gaztañaga E., 2017, A&A, 598, A103

Rasia E., Tormen G., Moscardini L., 2004, MNRAS, 351, 237

Rawle T. D., Smith R. J., Lucey J. R., Swinbank A. M., 2008, MNRAS, 389, 1891

Reddick R. M., Wechsler R. H., Tinker J. L., Behroozi P. S., 2013, ApJ, 771, 30

Renzini A., 2006, ARA&A, 44, 141

Rodríguez-Puebla A., Avila-Reese V., Yang X., Foucaud S., Drory N., Jing Y. P., 2015, ApJ, 799, 130

Rodríguez-Puebla A., Behroozi P., Primack J., Klypin A., Lee C., Hellinger D., 2016, MNRAS, 462, 893

Romano D., Silva L., Matteucci F., Danese L., 2002, MNRAS, 334, 444

Romanowsky A. J., Fall S. M., 2012, ApJS, 203, 17

Rubin V. C., Burstein D., Ford, Jr. W. K., Thonnard N., 1985, ApJ, 289, 81

Rubin V. C., Ford, Jr. W. K., Thonnard N., 1980, ApJ, 238, 471

Sandage A., 1961, The Hubble Atlas of Galaxies

Sandvik H. B., Möller O., Lee J., White S. D. M., 2007, MNRAS, 377, 234

Schaye J. et al., 2015, MNRAS, 446, 521

Sciama D. W., 1955, MNRAS, 115, 3

Seljak U., Zaldarriaga M., 1996, ApJ, 469, 437

Sembach K. R., Howk J. C., Ryans R. S. I., Keenan F. P., 2000, ApJ, 528, 310

Sérsic J. L., 1963, Boletin de la Asociacion Argentina de Astronomia La Plata Argentina, 6, 41

Shandarin S. F., Zeldovich Y. B., 1989, Reviews of Modern Physics, 61, 185

Shankar F., Lapi A., Salucci P., De Zotti G., Danese L., 2006, ApJ, 643, 14

Sharma S., Steinmetz M., Bland-Hawthorn J., 2012, ApJ, 750, 107

Shen S., Mo H. J., White S. D. M., Blanton M. R., Kauffmann G., Voges W., Brinkmann J., Csabai I., 2003, MNRAS, 343, 978

Sheth R. K., 1998, MNRAS, 300, 1057

—, 2003, MNRAS, 345, 1200

Sheth R. K., Lemson G., 1999, MNRAS, 305, 946

Sheth R. K., Mo H. J., Tormen G., 2001, MNRAS, 323, 1

Sheth R. K., Tormen G., 2002, MNRAS, 329, 61

—, 2004, MNRAS, 350, 1385

Sheth R. K., van de Weygaert R., 2004, MNRAS, 350, 517

Shi J., Wang H., Mo H. J., 2015, ApJ, 807, 37

Shlosman I., Noguchi M., 1993, ApJ, 414, 474

Shostak G. S., 1973, A&A, 24, 411

Silk J., Rees M. J., 1998, A&A, 331, L1

Siudek M. et al., 2017, A&A, 597, A107

Skibba R. A., Sheth R. K., 2009, MNRAS, 392, 1080

Smartt S. J., Rolleston W. R. J., 1997, ApJ, 481, L47

Sokołowska A., Capelo P. R., Fall S. M., Mayer L., Shen S., Bonoli S., 2017, ApJ, 835, 289

Somerville R. S., Kolatt T. S., 1999, MNRAS, 305, 1

Somerville R. S., Primack J. R., 1999, MNRAS, 310, 1087

Sparre M., Hansen S. H., 2012, J. Cosmology Astropart. Phys., 10, 49

Spitoni E., Matteucci F., Marcon-Uchida M. M., 2013, A&A, 551, A123

Springel V., 2005, MNRAS, 364, 1105

Springel V. et al., 2008, MNRAS, 391, 1685

—, 2005, Nature, 435, 629

Springel V., White S. D. M., Tormen G., Kauffmann G., 2001, MNRAS, 328, 726

Steinmetz M., 1999, Ap&SS, 269, 513

Swinbank M. et al., 2017, ArXiv e-prints

Tadaki K.-i. et al., 2017, ApJ, 834, 135

Takase B., Kinoshita H., 1967, PASJ, 19, 409

Tassev S., Zaldarriaga M., Eisenstein D. J., 2013, J. Cosmology Astropart. Phys., 6, 036

Thielemann F.-K., Nomoto K., Hashimoto M.-A., 1996, ApJ, 460, 408

Thomas D., Greggio L., Bender R., 1998, MNRAS, 296, 119

Thomas D., Maraston C., 2003, A&A, 401, 429

Thomas D., Maraston C., Bender R., Mendes de Oliveira C., 2005, ApJ, 621, 673

Thomas D., Maraston C., Schawinski K., Sarzi M., Silk J., 2010, MNRAS, 404, 1775

Thomas J. et al., 2009, MNRAS, 393, 641

Toomre A., 1963, ApJ, 138, 385

—, 1964, ApJ, 139, 1217

Toomre A., Toomre J., 1972, ApJ, 178, 623

Tormen G., 1997, MNRAS, 290, 411

Trager S. C., Worthey G., Faber S. M., Burstein D., González J. J., 1998, ApJS, 116, 1

Trujillo I., Ferreras I., de La Rosa I. G., 2011, MNRAS, 415, 3903

Tumlinson J. et al., 2011, Science, 334, 948

Uhlemann C., Codis S., Kim J., Pichon C., Bernardeau F., Pogosyan D., Park C., L'Huillier B., 2017, MNRAS, 466, 2067

van Albada T. S., Bahcall J. N., Begeman K., Sancisi R., 1985, ApJ, 295, 305

van den Bosch F. C., 2002, MNRAS, 331, 98

van den Bosch F. C., Abel T., Croft R. A. C., Hernquist L., White S. D. M., 2002, ApJ, 576, 21

van den Bosch F. C., Aquino D., Yang X., Mo H. J., Pasquali A., McIntosh D. H., Weinmann S. M., Kang X., 2008, MNRAS, 387, 79

van den Bosch F. C., Burkert A., Swaters R. A., 2001, MNRAS, 326, 1205

van den Bosch F. C., Jaffe W., van der Marel R. P., 1998, MNRAS, 293, 343

van den Bosch F. C., Tormen G., Giocoli C., 2005, MNRAS, 359, 1029

van der Wel A. et al., 2014, ApJ, 788, 28

van Dokkum P. G. et al., 2014, ApJ, 791, 45

—, 2015, ApJ, 813, 23

Velander M. et al., 2014, MNRAS, 437, 2111

Vincenzo F., Matteucci F., Belfiore F., Maiolino R., 2016, MNRAS, 455, 4183

Vitvitska M., Klypin A. A., Kravtsov A. V., Wechsler R. H., Primack J. R., Bullock J. S., 2002, ApJ, 581, 799

Vogelsberger M. et al., 2014a, Nature, 509, 177

—, 2014b, MNRAS, 444, 1518

—, 2014c, MNRAS, 444, 1518

Wang H., Mo H. J., Jing Y. P., 2009, MNRAS, 396, 2249

Wang H., Mo H. J., Jing Y. P., Yang X., Wang Y., 2011, MNRAS, 413, 1973

Wang H., Mo H. J., Yang X., van den Bosch F. C., 2012, MNRAS, 420, 1809

Wang H. Y., Jing Y. P., Mao S., Kang X., 2005, MNRAS, 364, 424

Wang H. Y., Mo H. J., Jing Y. P., 2007, MNRAS, 375, 633

Wang Y., Yang X., Mo H. J., van den Bosch F. C., Katz N., Pasquali A., McIntosh D. H., Weinmann S. M., 2009, ApJ, 697, 247

Watson D. F., Conroy C., 2013, ApJ, 772, 139

Watson D. F. et al., 2015, MNRAS, 446, 651

Wechsler R. H., Bullock J. S., Primack J. R., Kravtsov A. V., Dekel A., 2002, ApJ, 568, 52

Wechsler R. H., Zentner A. R., Bullock J. S., Kravtsov A. V., Allgood B., 2006, ApJ, 652, 71

Wetzel A. R., 2011, MNRAS, 412, 49

Wetzel A. R., Tinker J. L., Conroy C., 2012, MNRAS, 424, 232

Wetzel A. R., Tinker J. L., Conroy C., Bosch F. C. v. d., 2014, MNRAS, 439, 2687

Wetzel A. R., Tinker J. L., Conroy C., van den Bosch F. C., 2013, MNRAS, 432, 336

White S. D. M., 1984, ApJ, 286, 38

White S. D. M., Efstathiou G., Frenk C. S., 1993, MNRAS, 262, 1023

White S. D. M., Frenk C. S., 1991, ApJ, 379, 52

White S. D. M., Rees M. J., 1978, MNRAS, 183, 341

Wojtak R., Mamon G. A., 2013, MNRAS, 428, 2407

Xie L., Gao L., 2015, MNRAS, 454, 1697

Yang X., Mo H. J., van den Bosch F. C., Pasquali A., Li C., Barden M., 2007, ApJ, 671, 153

Yang X., Mo H. J., Zhang Y., van den Bosch F. C., 2011, ApJ, 741, 13

Zavala J. et al., 2016, MNRAS, 460, 4466

Zehavi I. et al., 2011, ApJ, 736, 59

Zel'dovich Y. B., 1970, A&A, 5, 84

Zentner A. R., Bullock J. S., 2003, ApJ, 598, 49

Zhang Y., Yang X., Faltenbacher A., Springel V., Lin W., Wang H., 2009, ApJ, 706, 747

Zhao D. H., Jing Y. P., Mo H. J., Börner G., 2003a, ApJ, 597, L9

—, 2009, ApJ, 707, 354

Zhao D. H., Mo H. J., Jing Y. P., Börner G., 2003b, MNRAS, 339, 12

Zhu H., Alam S., Croft R. A. C., Ho S., Giusarma E., 2017, MNRAS, 471, 2345

Zu Y., Mandelbaum R., 2015, MNRAS, 454, 1161